

**Experimental investigation of inclined cantilever beams in vertically falling soap
films**

by

Veera Brahmendra Chary Sajjanapu
(Veera B C Sajjanapu)

A thesis submitted to the graduate faculty
in partial fulfillment of the requirements for the degree of
MASTER OF SCIENCE

Major: Aerospace Engineering

Program of Study Committee:
Thomas Ward III, Major Professor
Partha P. Sarkar
Alric P. Rothmayer

Iowa State University
Ames, Iowa
2017

Copyright © Veera Brahmendra Chary Sajjanapu
(Veera B C Sajjanapu), 2017. All rights reserved.

DEDICATION

I dedicate this thesis to my mother, Smt. Vijaya Lakshmi without whose support, motivation and eternal love, since the beginning of my journey to the United States until now, has enabled me to accomplish this goal. I would like to thank my major professor for his support and patience in successfully achieving the research objective. Lastly, I thank my family for their loving guidance and financial assistance through out the time I spent for my masters degree.

TABLE OF CONTENTS

LIST OF TABLES	v
LIST OF FIGURES	vi
ACKNOWLEDGEMENTS	xiii
ABSTRACT	xv
CHAPTER 1. INTRODUCTION	1
1.1 Background and Motivation	2
1.1.1 Deflection of a cantilever beam	4
1.2 Literature Review	5
1.2.1 Piezoelectric beams in low-speed wind tunnel	5
1.3 Nomenclature	8
1.4 Wind tunnel experiments and governing equations	9
1.5 Summary	20
CHAPTER 2. FLOW VISUALIZATION AND MEASUREMENT TECH-	
NIQUES	22
2.1 Introduction	22
2.2 Experimental Setup	26
2.2.1 Fluid injection	28
2.2.2 Channel expansion	29
2.2.3 Channel test section	31
2.2.4 Channel contraction	31
2.2.5 Flow illumination and thickness of the film	33
2.2.6 Materials considerations	36

2.3	Operation	37
2.3.1	Flow control and channel geometry	37
2.3.2	Optimal soap solutions	42
2.3.3	Surrounding conditions	42
2.3.4	Variety of test pieces in the soap film tunnel	43
2.4	Measurement Techniques	46
2.4.1	Velocity measurement	46
CHAPTER 3. CANTILEVER BEAMS IN SOAP FILM: METHODS AND PROCEDURES		49
3.1	Introduction	49
3.1.1	Single cantilever beam at an inclination	51
3.1.2	Beam characteristics in soap film	56
3.1.3	Vortex shedding behind the cantilever beam	56
CHAPTER 4. IMAGE PROCESSING		60
4.1	Velocity measurement	62
4.2	Tracking beam vibrations	64
4.3	Tracking vortices in the wake	67
CHAPTER 5. RESULTS AND DISCUSSION		69
5.1	Introduction	69
5.1.1	Steady displacement loading vs dynamic loading	70
5.1.2	Strouhal number vs Reynolds number	71
5.1.3	Strouhal vs angle of attack	74
5.1.4	Beam vibrations vs vortex shedding	74
CHAPTER 6. CONCLUSIONS AND FUTURE WORK		81
APPENDIX A. ADDITIONAL EXPERIMENTS		83
APPENDIX B. SUPPLEMENTARY MATERIAL		85
BIBLIOGRAPHY		88

LIST OF TABLES

Table 1.1	Aerodynamic forcing coefficients $F_i = C_i \rho_\infty U_\infty^2 A_L / 2$ where $i = s$ or ω corresponding to steady and unsteady forcing, respectively.	18
Table 2.1	Data for test pieces	36
Table 3.1	Properties of the soap film test models	49
Table 3.2	Comparison of test models used in the wind tunnel and the soap film experiments	50
Table 3.3	Angles of attack for $L = 7.5$ mm	53
Table 3.4	Angles of attack for $L = 10$ mm	53
Table 3.5	Angles of attack for $L = 20$ mm	53
Table 5.1	For flexible beam: Aerodynamic coefficients with respect to increase in angle of attack	70
Table 5.2	For semi-flexible beam: Aerodynamic coefficients with respect to increase in angle of attack	70
Table 5.3	For rigid beam: Aerodynamic coefficients with respect to increase in angle of attack	71
Table B.1	Aerodynamic forcing coefficients $F_i = C_i \rho_\infty U_\infty^2 A_L / 2$ where $i = s$ or ω corresponding to steady and unsteady forcing, respectively.	86

LIST OF FIGURES

Figure 1	Vortex structure visualization in soap film	xiv
Figure 1.2	Various piezoelectric applications	3
Figure 1.3	A point load acting on a cantilever beam	4
Figure 1.5	Piezoelectric thin films in the wind tunnel	6
Figure 1.6	Schematic of two piezoelectric beams in wind tunnel	10
Figure 1.7	Schematic depiction of piezoelectric cantilever beam displacement in a wind tunnel (not shown). In a) we show the streamwise xy-plane and in b) the spanwise yz-plane.	10
Figure 1.8	Displacement versus elapsed time waveforms for a) 3.6 and b) 1.6 aspect ratio piezoelectric cantilever beams. Note the difference in the horizontal and vertical axis scales.	13
Figure 1.9	Cantilever tip displacement and measured voltage frequencies versus aerodynamic loading. Open symbols correspond to measurements made using tip displacement data for aspect ratios a) 1.6 \bigcirc , \triangle and b) 3.6 \times , \square . Note: the same relationship between the open symbols and corresponding experiment are used in the figures that follow. The closed symbols \blacklozenge correspond to frequencies measured using oscilloscope data.	14
Figure 1.10	Force measured from steady tip displacement of a vibrating cantilever $F_s = 8EIu_s(L)/L^3$, versus dynamic force. The dotted lines — are best fits with slopes of C_s	16

Figure 1.11	Amplitude of the vibrating cantilever tip $u_\omega(L)$ versus aerodynamic force. The dotted lines $--$ are results of numerical simulations of Eq. 1.1 for values of C_ω shown in Table 1.	17
Figure 1.12	Voltage versus vibration force $m\omega^2 u_\omega$ where $m = \rho AL$ for the low and larger aspect ratio piezoelectric cantilevers. Dotted line ' $--$ ' is the best fit for all of the experimental data points.	19
Figure 2.2	Soap bubble structure: Depending on the thickness of the film, different colours interfere constructively and destructively	23
Figure 2.3	Soap film when interfered with an illumination source. a) Soap film between two thin wires. Image captured from our setup. b) Soap film in a circular hoop. Observe how the interference patterns converge downwards due to gravity (Source: //hyperphysics.phy-astr.gsu.edu)	24
Figure 2.4	Why soap films? A better technique pertained to our application . . .	25
Figure 2.5	Cross-sectional view of a soap film between two vertical wires. The film gets attached to the wire at a contact angle called the Plateau border. The diagram is not drawn to scale. Approximate sizes are wire diameter 0.5 mm, wire spacing 8 cm, film thickness of order $4\mu\text{m}$, Rutgers et al. (2001)	27
Figure 2.6	Actual setup of vertically falling soap films	27
Figure 2.7	Schematic of the experimental setup	28
Figure 2.8	Schematic of the conical nozzle	29
Figure 2.9	Conical nozzle with elliptical type opening	30
Figure 2.10	All 3 sections of the soap film (top to bottom) for 0.3, 0.5, 0.8 GPH (left to right) for a 7.5 cm channel width is shown. Note how the interference patterns depict the magnitude and direction of the flow. d) and e) are schematic and actual setup images respectively. We can see the pull wires in e) ready to expand the soap film.	32
Figure 2.11	Top view of the soap film experiment setup	34

Figure 2.12	Circuit diagram of low pressure sodium lamps with a ballast	35
Figure 2.13	The tri-connection with the bypass pipe to lower the pressure of water driven by the motor	38
Figure 2.14	The flowmeter from KING instrument company, of 7520/7530 series with a bl-float that can sustain up to 125 psig water at a max temperature of 130° F	39
Figure 2.15	Soap film formation process	40
Figure 2.16	Freestream velocity for various channel widths	41
Figure 2.17	Temperature of the soap film with respect to the experiments runtime	43
Figure 2.18	Visualization of the downstream vortex shedding for different objects in the soap film. a) Flexible filament, b) Cambered airfoil cross-section, c) Flexible airfoil cross-section, d) Symmetric airfoil cross-section, e) Thin cylinder, f) Thick rectangular plate	44
Figure 2.19	Visualization of vortices behind a cylinder of diameter 2 mm for Reynolds numbers ranging from, Re: 5500-8500	45
Figure 2.20	Velocity profile for a 2 cm window in a 7.5 cm channel width test section from 0.3 - 0.8 GPH. As a result we achieve an approximate uniform flow in this window.	47
Figure 3.1	Schematic of the inclined cantilever beam	50
Figure 3.2	Schematic of the inclined cantilever beam	52
Figure 3.3	First natural (eigen) frequencies calculated in air for beams of lengths $L = 7.5$ mm, $L = 10$ mm, $L = 20$ mm and $L = 25$ mm. Note the good agreement with our assumptions of natural frequencies.	54
Figure 3.4	Cantilever beam with the change in inclination. a), b), c) are the current models analyzed and interpreted for results. Results for d), e), f) can be found in the Appedix. 1 as a part of additional materials	55

Figure 3.5	Vibrating flexible beam of length $L = 10$ mm at an $\alpha_2 = 31^\circ$ at 0.3 GPH in soap film. Although the vibrations are very small, we could see the vortex shedding locked in with the trailing edge of the beam. . . .	57
Figure 3.6	Vortex shedding for flexible beam of length $L = 7.5$ mm at an $\alpha_2 = 30^\circ$ at 0.3 GPH. We could clearly see the vortex shedding lock-in behavior as discussed by other authors in the literature.	59
Figure 4.1	RGB image type. a) Depicts the computer vision for an RGB image type (Source: Mathworks). b) The 3-D matrix format of an RGB image. c) An experiment image viewed though the high-speed camera interface with the window sizes	61
Figure 4.2	Tracking the defects in the soap film. The algorithm automatically tracks all the defects or pollutants in the soap film and the average flow-rate of the freestream is estimated. b) is the filtered and processed image of a). Time is incrementing from top to bottom.	63
Figure 4.3	Flowchart for Image digitalization	64
Figure 4.4	Tracking the tip of the beam. The image processing is displayed in a step-by-step manner. e) is the final processed image ready to be analyzed.	65
Figure 4.5	c) Waveform of the tracked tip of the beam. These waveforms are then processed through an FFT filter to extract the frequencies as shown in d)	66
Figure 4.6	Tracking the vortices shed behind a rigid beam having an angle of attack $\alpha = 27^\circ$	68
Figure 5.1	Plotting nomenclature for a better understanding of the plots.	70
Figure 5.3	Steady tip displacement force of a flexible vibrating cantilever beam of Length ($L_1 = 7.5$ mm) versus dynamic force with varying angle of attacks.	71
Figure 5.4	Steady tip displacement force of a flexible vibrating cantilever beam of Length ($L_2 = 10$ mm) versus dynamic force with varying angle of attacks.	71

Figure 5.5	The dotted lines are linear fits having slopes dependent on the angle of attack. This slope is identified as an aerodynamic loading coefficient C_{SAL} . Note that C_{SAL} increases with the increase in angle of attack .	71
Figure 5.7	Steady tip displacement force of a semi-flexible vibrating cantilever beam of Length ($L_1 = 7.5 \text{ mm}$) versus dynamic force with varying angle of attacks.	72
Figure 5.8	Steady tip displacement force of a semi-flexible vibrating cantilever beam of Length ($L_2 = 10 \text{ mm}$) versus dynamic force with varying angle of attacks.	72
Figure 5.9	The dotted lines are linear fits having slopes dependent on the angle of attack. These slopes are identified as an aerodynamic loading coefficient C_{SAL} . Note that C_{SAL} increases with the increase in angle of attack .	72
Figure 5.10	Steady tip displacement force of a relatively rigid vibrating cantilever beam of Length ($L_2 = 10 \text{ mm}$) versus dynamic force with varying angle of attacks. The dotted lines are linear fits having slopes dependent on the angle of attack. This slope is identified as an aerodynamic loading coefficient C_{SAL} . Note that C_{SAL} increases with the increase in angle of attack	73
Figure 5.11	Steady tip displacement force of a flexible vibrating cantilever beam of both lengths ($L_1 = 7.5 \text{ mm}$ and $L_2 = 10 \text{ mm}$) versus dynamic force with varying angle of attacks are compared with that of the results obtained from the wind tunnel experiments. The dotted lines are linear fits having slopes dependent on the angle of attack. This slope is identified as an aerodynamic loading coefficient C_{SAL} . Note that C_{SAL} increases with the increase in angle of attack	75
Figure 5.13	Steady tip displacement force of a relatively rigid vibrating cantilever beam of Length ($L_1 = 7.5 \text{ mm}$) versus dynamic force with varying angle of attacks.	76

Figure 5.14	Steady tip displacement force of a relatively rigid vibrating cantilever beam of Length ($L_2 = 10 \text{ mm}$) versus dynamic force with varying angle of attacks.	76
Figure 5.15	The dotted lines are linear fits having slopes dependent on the angle of attack. These slopes are identified as an aerodynamic loading coefficient C_{SAL} . Note that C_{SAL} increases with the increase in angle of attack .	76
Figure 5.16	Steady tip displacement force of a relatively rigid vibrating cantilever beam of Lengths ($L_1 = 7.5 \text{ mm}$ and $L_2 = 10 \text{ mm}$) versus dynamic force with varying angle of attacks. The dotted lines are linear fits having slopes dependent on the angle of attack. This slope is identified as an aerodynamic loading coefficient C_{SAL} . Note that C_{SAL} increases with the increase in angle of attack	77
Figure 5.18	Strouhal numbers versus Reynolds numbers for Lengths ($L_1 = 7.5 \text{ mm}$) and ($L_2 = 10 \text{ mm}$)	78
Figure 5.19	Strouhal numbers versus Reynolds numbers for rigid beam of Length ($L_2 = 10 \text{ mm}$)	78
Figure 5.20	Strouhal number vs angle of attack for all data sets	79
Figure 5.21	Vortex shedding frequency (f_{vs}) with corresponding beam vibrational frequencies (f_{bv}) for all data sets. Note how the data aligns with the $x=y$ line showing the dependency of f_{bv} with the corresponding f_{vs} . .	79
Figure 5.22	Beam vibrational frequencies (f_{bv}) with corresponding vibrational amplitude strengths (V_{as}) for all data sets. Same notation applies for the data. It can be observed that the flexible beam has a higher amplitude strengths i.e high amplitude of vibrations compared to the semi-flexible beam (red) and the rigid beam (black)	80
Figure A.1	Cantilever beam with the change in inclination. Analysis for St. Vs α can be found in Fig. A.2	83

Figure A.2	Strouhal number Vs α updated with higher inclination experiments. A curve approximating the data is represented by the green dotted line. .	84
Figure S1	Free vibrations for a piezoelectric cantilever with aspect ratio a) 1.6 (short) and b) 3.6 (long).	85
Figure S2	Displacement versus elapsed time waveforms for a) 3.6 and b) 1.6 aspect ratio piezoelectric cantilever beams found by solving the Euler-Bernoulli beam equation.	87

ACKNOWLEDGEMENTS

I would like to take this opportunity to express my thanks to those who helped me with various aspects of conducting research and the writing of this thesis. First and foremost, Dr. Thomas Ward for his guidance, patience, support and valuable suggestions for conducting this research. His insights and words of encouragement have often inspired me and renewed my hopes for completing my graduate education. I would also like to thank Dr. Partha Sarkar for serving as a committee member for my graduate education. I would additionally like to thank Dr. Alric Rothmayer for serving as a minor representative for my applied math minor and also serving as a committee member for my graduate education. Sincere thanks to the undergraduate research assistants Stanley Barbel and Layne Droppers for conducting the wind tunnel experiments.



Figure 1: Vortex structure visualization in soap film

ABSTRACT

Here we investigate the dynamic response of cantilever beam at various angles of attack using theory and experiments. The problem is motivated by separate wind tunnel experiments using energy producing piezoelectric cantilevers. Assuming small vibrational amplitudes, we utilize the Euler-Bernoulli beam theory to test semi-empirical correlations that are compared with measured quantities. To utilize the beam theory, we estimate the aerodynamic loading on the cantilever as the sum of a steady and harmonic component, each proportional to the aerodynamic pressure. Dynamically similar cantilever beams ($5000 < \text{Re} < 25000$) with varying flexural rigidity are studied in a vertically falling soap film experiment to visualize the wake and vortex shedding flow characteristics. High speed video and image analysis were used to estimate quantities such as the average displacement, vibration amplitude and frequency for the cantilevers. From the analysis we find the steady displacement force is linear with respect to the aerodynamic pressure. We define a coefficient which is the ratio of steady displacement force and aerodynamic pressure. We call this steady aerodynamic loading coefficient. We further show that there is a significant effect of inclination on this coefficient. Furthermore, this coefficient was found to be dependent on the flexible nature of the cantilever beam. The wake structure and the vortex shedding are visualized and analyzed for the vortex shedding frequency which is plotted against the frequency of beam vibrations. We also explore the relationship between the Strouhal, Reynolds numbers and angle of attack.

CHAPTER 1. INTRODUCTION

The thesis is constructed on the basis of the nature of piezoelectric materials and their applications. These materials when subjected to vibrations or mechanical strain, are capable of converting the mechanical energy to electrical energy and vice-versa. These materials come in two major forms, a ceramic disc type and a flexible beam type. The present study focuses on the latter type. The flexible piezoelectric beams are used in energy harvesting, self-powering devices, MAV's, NAV's, etc.

Few naturally occurring materials have the capability to generate an electric charge when sustained to any mechanical vibration and vice-versa. These materials are known as piezoelectric materials and the phenomena is called piezoelectric phenomena. The phenomenon was first discovered by Pierre and Jacques Curie in 1880. They demonstrated that when specially prepared crystals (such as quartz, topaz and Rochelle salt) were subjected to a mechanical stress, a surface charge could be measured. A year later, Gabriel Lippmann deduced from thermodynamics that when in an applied electric field they would also exhibit a strain. The Curies later experimentally confirmed this effect and provided proof of the linear and reversible nature of piezoelectricity.

Among the first few applications of the piezoelectric effect, one was an ultrasonic submarine detector developed during the First World War. A mosaic of thin quartz crystals glued between two steel plates acted as a transducer that resonated at 50 MHz. By submerging the device and applying a voltage they succeeded in emitting a high frequency 'chirp' underwater, which enabled them to measure the depth by timing the return echo. This was the basis for sonar and the development encouraged other applications using piezoelectric devices both resonating and non-resonating such as microphones, signal filters and ultrasonic transducers. The applications range from automotive to military but are not limited to medical. Some typical applications

are:

Automotive: Air bag sensor, air flow sensor, audible alarms, fuel atomiser, keyless door entry, seat belt buzzers, knock sensors.

Computer: Disc drives, inkjet printers.

Consumer: Cigarette lighters, depth finders, fish finders, humidifiers, jewellery cleaners, musical instruments, speakers, telephones.

Medical: Disposable patient monitors, foetal heart monitors, ultrasonic imaging.

Military: Depth sounders, guidance systems, hydrophones, sonar.

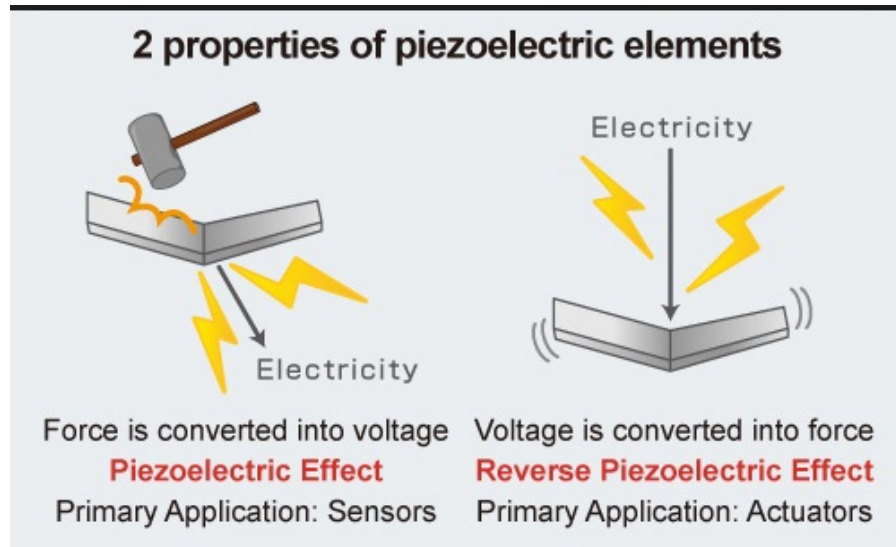
These advances in modern technology have led to flexible synthetic devices, piezoelectric transducers, that can be incorporated into the structure of a device, allowing it to compress/bend and withstand these forces converting this mechanical energy into electricity.

Piezoelectric transducers have been used in various designs for fluid flow energy harvesting to generate power, on the scale of microwatts and milliwatts, for small electronic devices such as remote sensors. One such device was provided by Allen and Smits (2001), is called a piezoelectric eel which is a sheet of piezoelectric polymer oscillating underwater in the wake of a bluff body. Another device that operates in air, designed by Priya et al. (2004) was based on more conventional rotating turbine designs that implement piezoelectric discs driven by cam systems. Schmidt (1992) developed, an oscillating blade generator, which uses a piezoelectric transducer to connect a steel leaf spring to leaf-like ears.

We implemented a similar objective system, where the piezoelectric thin film is fixed to the floor of a low-speed wind tunnel. Hence the piezoelectric beam now acts as a cantilever beam. The beam is connected to an oscilloscope to record the voltage output when the experiment is ran for various Reynolds numbers.

1.1 Background and Motivation

Utilizing piezoelectric energy to power small, low-power electronic devices has emerged recently as an area of high interest. Many approaches to harness piezoelectric energy have been studied, using various vibrational systems. Researchers have found out that the response



- (a) Piezoelectric phenomena illustrated in beams.
 Various applications based on their properties
 (Source: www.rohm.com)



- (b) Latest in-shoe device is designed to harvest the energy that is created by walking, and store it for use in mobile electronic devices (Source: New atlas newsletter)

Figure 1.2: Various piezoelectric applications

to the vibrations is drastically affected by the angle of attack of the beam. This parameter is one of primary focuses of this research.

1.1.1 Deflection of a cantilever beam

When the free end of a cantilever beam is subjected to any type of load, P , the beam will deflect into a curve. Increase in load leads to increase in deflection, $v(x)$. See Fig. 1.3 below. Assuming the beam undergoes small deflections, is in the linearly elastic region, and has a uniform cross-section (Gere, p. 602), the curvature of the beam is equal to the second derivative of the deflection (δ) and can also be related to the bending moment (M) and flexural rigidity (EI).

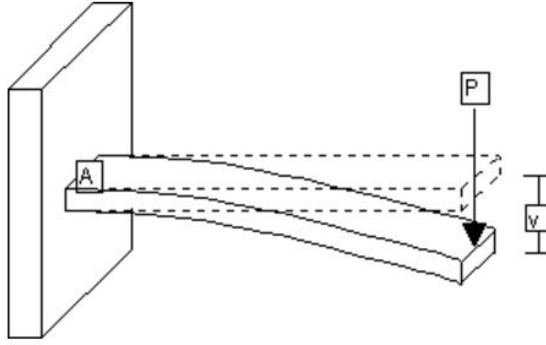


Figure 1.3: A point load acting on a cantilever beam

When the force, P , is removed from a displaced beam, the beam will return to its original shape. However, inertia of the beam will cause the beam to vibrate around that initial location. This is a phenomena associated with flexible cantilever beams, which elaborates the studies in the current thesis.

Application with soap film experiments The interactions between flexible beams and fluids, which exist in nature, everyday life, and industry applications, are a research focus in recent years. This topic involves complex flow phenomena and fluid structure interactions. It has important scientific significance and engineering values. Background on soap film experiments will be discussed in detail in Chapter 2.

We carry out a series of experiments on this topic using soap film tunnels by employing shim

plastic sheets as flexible beams. Based on the experiments, several problems on this topic were systematically investigated. The problems involve the interactions between a flexible beam and uniform and periodic flow.

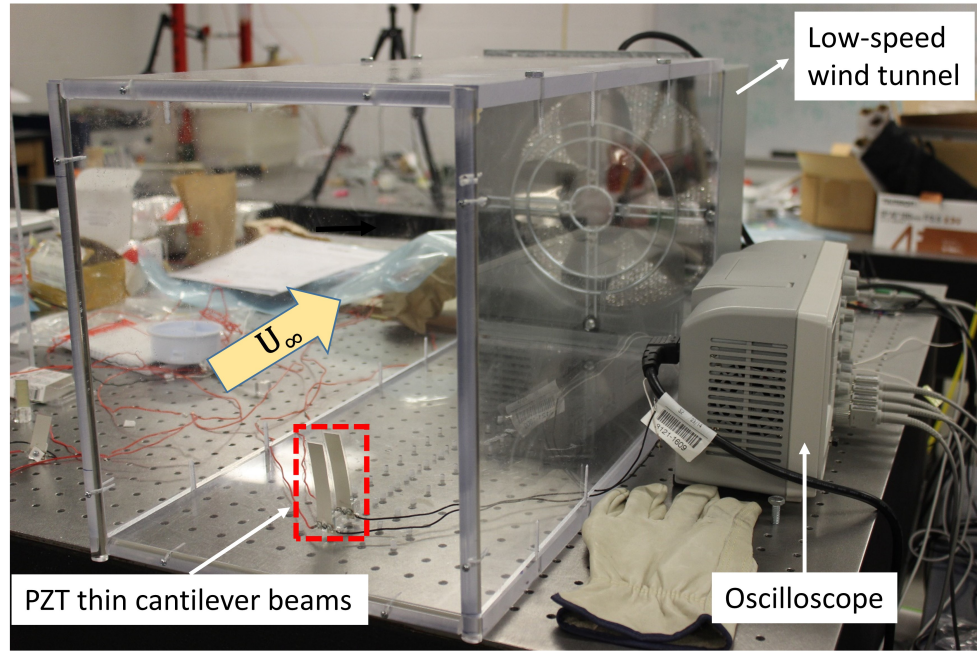
1.2 Literature Review

Flexible structure generally refers to an object that can have large elastic deformation. In this thesis, we focus on the interaction between flexible beams and their ambient fluid. In two-dimensional space, a beam is simplified to an elongated structure having thicknesses in the order hundredth of a millimeter. In our study, flexible beams are employed in soap films to provide a mimic of two-dimensional flow around a beam.

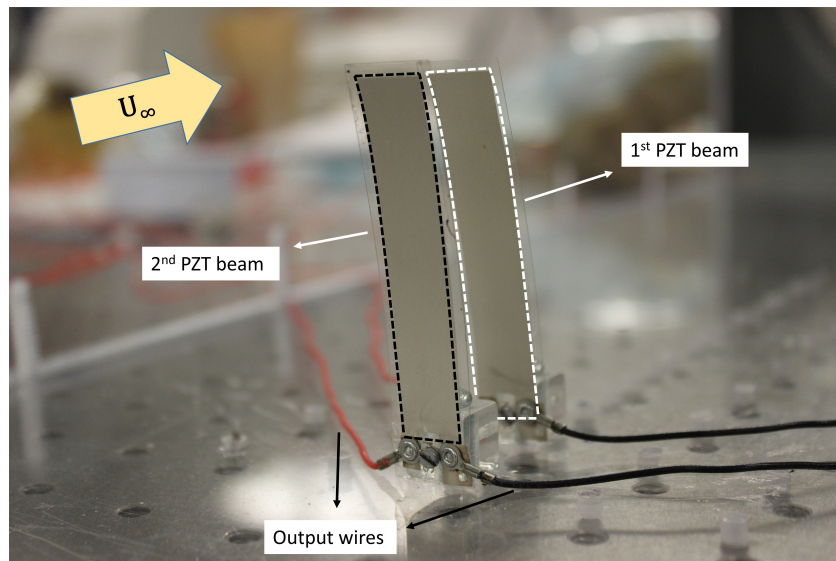
1.2.1 Piezoelectric beams in low-speed wind tunnel

The piezoelectric phenomenon is a reversible processes that occurs in ceramic materials that are capable of generating power (voltage and current) in response to a strain (Cook-Chennault et al., 2008; Erturk et al., 2010). Piezoelectric devices have gained much attention in recent years due to their potential use for power generation (Kim et al., 2015; Adendorff et al., 2015) with a minimal footprint. For example, researchers have been developing non-invasive ways to imbed piezoelectric devices into consumer products and other equipment to harvest energy; from shoes that undergo many compressive loading events during walking (Mateu and Moll, 2005; Cook-Chennault et al., 2008) to imbedding piezo-ceramics into the trailing edge of an airfoil (Zakaria et al., 2015). Here we focus attention on wind harvesting via laminated piezo-ceramic cantilevers that are used commercially as micro strain sensors.

It has already been demonstrated that piezoelectric cantilevers harvest wind by self-sustaining small-amplitude vibrations, the mechanics of which are not completely understood. Recently, though, researchers have begun to study the vibration process (flutter) by which energy is generated (Koyama and Nakamura, 2010; Kim et al., 2015; Hobeck and Inman, 2012). These studies are necessary since optimizing their energy harvesting potential will require additional scientific understanding of the underlying physics governing these vibrations. Here, we perform image analysis and voltage-difference measurements of laminated piezo-ceramic cantilevers of



(a) Piezoelectric thin films placed in low-speed wind tunnel at tandem to the flow direction



(b) A closer view of the two cantilever piezoelectric beams in the wind tunnel

Figure 1.5: Piezoelectric thin films in the wind tunnel

different aspect ratio (Dayou et al., 2015) that generate electricity by these same self sustained small-amplitude vibrations in a low speed (< 4 m/s) wind tunnel. The purpose is to test empirical correlations between measurable quantities, such as aerodynamic loading or vibrational amplitude, and the subsequent voltage that is generated. In particular, we propose a model for the small-amplitude vibrations using a 2D Euler-Bernoulli beam equation, and demonstrate through experiments that the vibration magnitude is directly proportional to the aerodynamic loading for the range of velocities used in the study. These are the first studies to use high speed imaging to directly visualize the transient small-amplitude displacements of the vibrating cantilever's tip.

Pobering et al. (2009) gave a detailed report on the design, fabrication, and testing of piezoelectric cantilever generators as electrical power sources for sensors. They use a similar cantilever beam setup, having three to nine cantilevers arranged in tandem to each other. All of them are operating in a streaming flow. A bluff body placed in front of the cantilevers lead to vortices in the stream. These vortices are connected with a low pressure surrounding area. Hence, cantilevers will be forced to deflect into the low pressure region. Due to noticeable resetting spring forces cantilevers starts to oscillate. Some of his experiments have been carried out in air, others were done in water. He found out the cantilevers were oscillating in air with their first eigen frequency. A synchronized oscillation was found for cantilevers in a water media. Electric power generated in the cantilevers was processed in an electric circuitry. This circuitry was supplied with energy by the cantilevers and was used to feed an external electric load. He concluded that Piezoelectric harvesters can convert the energy of streaming media due to self induced oscillation. Also, the smaller the converters were, the better was the efficiency of power conversion. This has been observed in our experiments. He also stated the internal structure of the cantilevers and their geometrical dimensions in relation to the bluff are a major factor accounting for the amount of power to be converted. Cantilevers arranged in a row oscillate synchronous in water and under defined conditions in gases, too.

Another researcher, Akaydin et al. (2012) worked on a self-excited energy harvester similar to Pobering et al. (2009). Their work includes an experimental investigation of a self-excited piezoelectric energy harvester subjected to a uniform and steady flow. The harvester consists

of a cylinder attached to the free end of a cantilevered beam, that is partially covered by piezoelectric patches. Due to fluidstructure interaction phenomena, the cylinder experiences oscillatory forces, and the beam is deflected accordingly, causing the piezoelectric elements to strain and thus develop electric charge. They found the attachment of a vibration-inducing body to the tip of the harvester beam resulted in a tremendous increase in the aeroelastic efficiency of the harvester.

One of the researcher studied the effect of angle of attack on these piezoelectric cantilever beams, without any external exciter. To harvest energy from aeroelastic vibrations, previous attempts have been based on attaching a beam to a moving wing or structure. Zakaria et al. (2015) exploited self-excited oscillations of a fluttering composite beam to harvest energy using piezoelectric transduction. He studied the effects of a preset angle of attack, wind speed, and load resistance on the levels of harvested power are determined. The results pointed to a complex relation between the aerodynamic loading and its impact on the static deflection and amplitudes of the limit cycle oscillations and the load resistance and level of power harvested. The results also showed a strong dependence of the frequency of oscillations on the flow speed and angle of attack. This shows that small variations in the aerodynamic loads cause variations in the beam stiffness when subjected to large deformations. The nonlinear effects of the system were detected by the observed harmonics in the spectra of the signal of the harvested voltage.

All of these works ultimately use an external bluff body or an exciter to initiate the fluctuations. Our research helps in understanding the behavior of the oncoming flow over these piezoelectric cantilevers without having any external exciter to initiate the vibration. We will be extensively focusing on vortex shedding effects on a single cantilever with different geometries, flexibilities, and inclination with the flow.

1.3 Nomenclature

L = Length of the beam

t = thickness of the beam

b = width or breadth of the beam

α = Angle of attack

E = Elastic modulus

I = Moment of Inertia

$E.I$ = Flexural rigidity

U_∞ = Velocity of freestream (m/s)

GPH = Gallons per hour

ρ_∞ = Density of freestream (m/s)

Re = Reynolds number

St = Strouhal number

(Definitions of Re and St vary depending on the experiment type)

u_s = Steady displacement (mm)

u_ω = Unsteady vibrations

F_s = Steady loading (N)

F_ω = Unsteady loading (N)

F_d = Dynamic loading

C_s = Coefficient of steady aerodynamic loading for wind tunnel experiments

C_{SAL} = Coefficient of steady aerodynamic loading for soap film experiments

C_ω = Coefficient of unsteady loading

f_{bv} = Frequencies of beam vibrations

f_{vs} = Frequencies of vortex shedding

1.4 Wind tunnel experiments and governing equations

The schematic of our low-speed box wind tunnel is shown in 1.6. This setup is capable of having up to 20-30 cantilevers placed in several orientations. An oscilloscope is attached to these piezoelectric cantilevers in order to have a measure of the voltage generated.

Consider a cantilever of length L with area $A_L = bL$ facing a low speed wind of uniform velocity U_∞ and density ρ_∞ such that the cantilever self oscillates (see Fig. 1.7 for schematic).

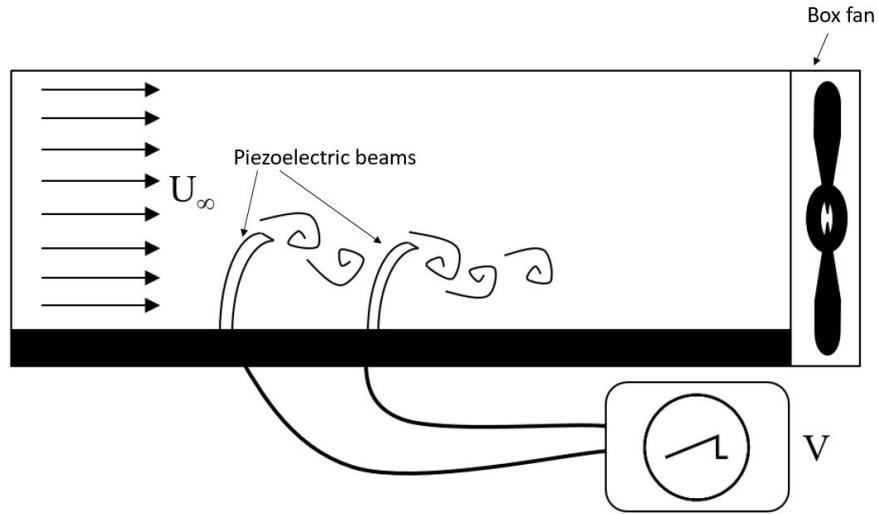


Figure 1.6: Schematic of two piezoelectric beams in wind tunnel

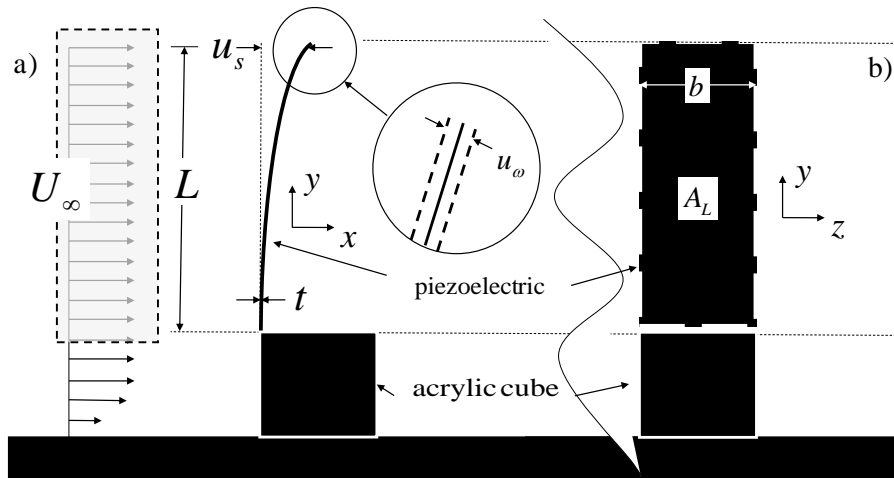


Figure 1.7: Schematic depiction of piezoelectric cantilever beam displacement in a wind tunnel (not shown). In a) we show the streamwise xy -plane and in b) the spanwise yz -plane.

The oscillations are small-amplitude and, we propose, can be described in 2D using the Euler-Bernoulli beam equation.

$$\rho A \frac{\partial^2 u}{\partial t^2} + \mu_1 \frac{\partial u}{\partial t} + \mu_2 I \frac{\partial^5 u}{\partial x^4 \partial t} + EI \frac{\partial^4 u}{\partial x^4} = F'_s + F'_\omega e^{i\omega t}. \quad (1.1)$$

Here, $u(x, t) = u_s(x) + u_\omega(x)e^{i\omega t}$ (Zhao and Yang, 2015) is the cantilever displacement, written as the sum of a steady u_s and an unsteady-vibration u_ω component, ρ the piezoelectric cantilever density, $A = tL$ the cross sectional area, E the elastic modulus and I the area moment of inertia. The left hand side is the standard Euler-Bernoulli beam equation where we include net external (linear viscous), $\mu_1 \partial u / \partial t$, and internal $\mu_2 I (\partial^5 u / \partial x^4 \partial t)$ (Kelvin-Voigt) damping (Banks and Inman, 1989) for a homogeneous cantilever. The constants F'_s and F'_ω are used to represent the steady and unsteady components of the aerodynamic loading, respectively, and both have dimensions of force per unit length (' denotes per unit length quantities). The unsteady-vibration component to the loading consist of a single harmonic function with frequency ω (Zhao and Yang, 2015). We relate the aerodynamic loading terms to the aerodynamic force $\rho_\infty U_\infty^2 A_L / 2$ (Song et al., 2015) according to

$$F_s = C_s \rho_\infty U_\infty^2 A_L / 2 \quad \text{and} \quad F_\omega = C_\omega \rho_\infty U_\infty^2 A_L / 2. \quad (1.2)$$

Analytical solutions for the linear PDE (Han et al., 1999) can be found by using the boundary conditions for a cantilever: $u(0, t) = 0$, $\partial u(0, t) / \partial x = 0$, $EI \partial^2 u(L, t) / \partial x^2 + \mu_2 I \partial^3 u(L, t) / \partial x^2 \partial t = 0$ and $EI \partial^3 u(L, t) / \partial x^3 + \mu_2 I \partial^4 u(L, t) / \partial x^3 \partial t = 0$, and with proper estimates for the damping coefficients (See Supplementary Material). The cantilever displacement may be initially set equal to the analytical solution for the steady forcing component i.e. $u(x, 0) = u_s(x) = [F_s / (24EIL)][x^4 - 4x^3L + 6(xL)^2]$.

To test the validity of the assumptions in (2) we performed experiments using piezoelectric strips (Images SI Inc.) of dimensions ($L_T \times b \times t$) $73 \times 17 \times 0.2 \text{ mm}^3$ and $41 \times 17 \times 0.2 \text{ mm}^3$ i.e. both had equal width and thickness but different length. Either piezoelectric strip was mounted to an acrylic cube ($13 \times 13 \times 13 \text{ mm}^3$) which reduced the vibrating portion of the cantilever's length by the length of one side of the cube $L = L_T - 13 \text{ mm}$. The corresponding

aspect ratios for the rectangular area facing the free stream (L/b) were either 1.6 or 3.6 for the *short* and *long* piezoelectric cantilevers, respectively. The piezoelectric cantilever density was $\rho = 1800 \text{ kg/m}^3$ with an average elastic modulus of $3 \times 10^9 \text{ GPa}$ based on information provided by the manufacturer. Data for the damping coefficients μ_1 and μ_2 , and results of the pattern search method (White and Ward, 2015) used to find their values, appears as Supplementary Material. To summarize that information; the internal damping coefficient is nearly identical for each strip ($\approx 1.4 \times 10^5 \text{ Pa s}$) and the external-viscous damping is slightly smaller (0.2 versus 0.06 Pa s) for a 3.6 aspect ratio cantilever.

The acrylic cube and piezoelectric strip assembly was bolted to the bottom wall of an open circuit wind tunnel at a distance approximately 75 mm from the inlet. The wind tunnel was an acrylic box that was assembled by bolting together four $0.3 \times 0.6 \times 0.013 \text{ m}^3$ acrylic plates. Semi-circular acrylic strips were attached to the wind tunnel inlet to help laminarize the flow (Madanu et al., 2016). A small box fan (Pentair) placed downstream from the test section drew air into the wind tunnel at a speed determined by a voltage regulator (Staco Energy) giving rise to small-amplitude vibrations of the piezoelectric cantilever. The free stream wind speed was measured prior to performing an experiment with a probe using hot wire anemometry (Extech). Vibrations of the cantilever tip were captured by fast camera (Hotshot) at 5000 frames per second, fit with a macro lens (Computar) and in a 200×500 pixels window. The macro lens and camera combination gave a pixel resolution of approximately $8 \mu\text{m}$ per pixel. A fluorescent lamp in-line with the camera was placed behind the setup for clearer visibility of the vibrating cantilever tip. Voltage was measured using an oscilloscope (Agilent Technologies). Wires of from the piezoelectric cantilevers were wrapped around the front to the rear of the acrylic cube and outside of the wind tunnel.

The experimental procedure consisted of, first, performing cantilever visualization experiments followed by experiments to measure voltage. Measurements were taken for both increasing (0-3.6 m/s) and decreasing (3.6-0 m/s) free stream velocity in approximately 0.4 m/s increments. The Reynolds numbers based on hydraulic diameter ($Re_H = U_\infty s / \nu$) were $Re_H < 1 \times 10^5$ where s is a side of the square face of the wind tunnel inlet; the Reynolds numbers based on a cantilevers' total length, L_T , were $Re_{L_T} < 3.2 \times 10^4$ and $Re_{L_T} < 1.9 \times 10^4$

for the long and short cantilevers, respectively; and Reynolds numbers for the anchoring cube were $< 6.2 \times 10^3$. Estimates for the boundary layer thickness were made using Blasius' flat plate solution and were determined to be less than the height of the anchoring cube based on their downstream distance from the wind tunnel inlet.

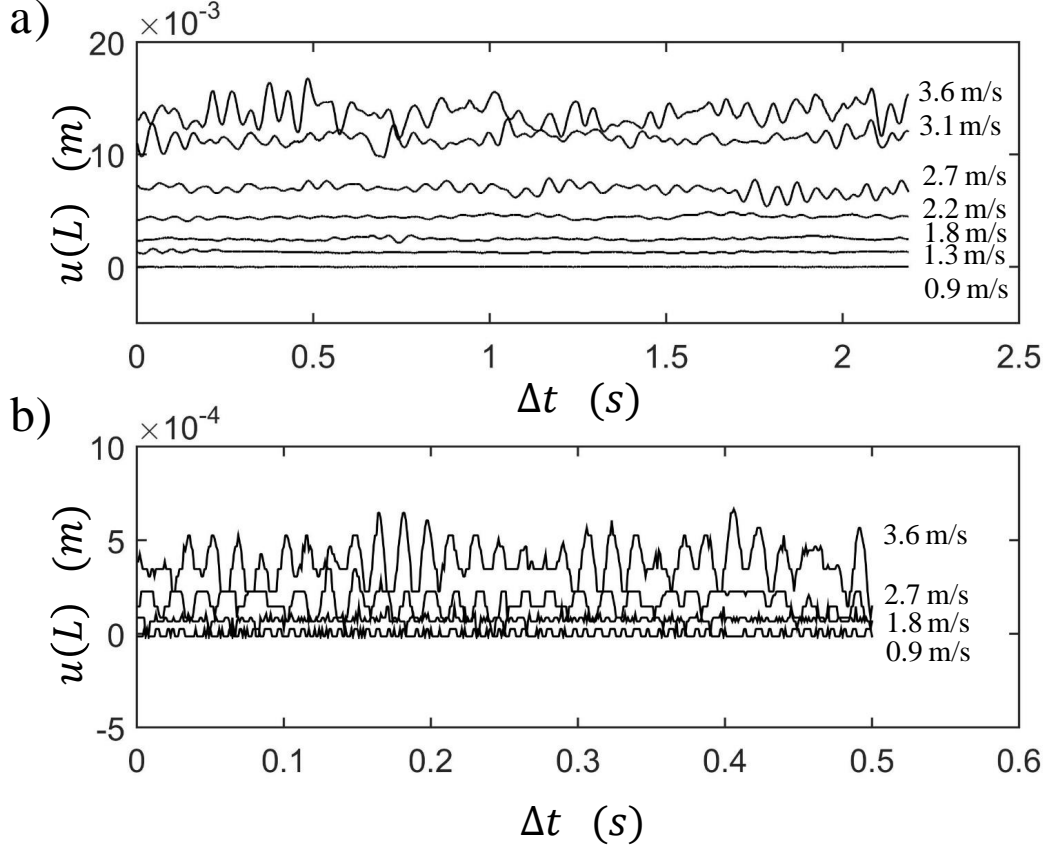


Figure 1.8: Displacement versus elapsed time waveforms for a) 3.6 and b) 1.6 aspect ratio piezoelectric cantilever beams. Note the difference in the horizontal and vertical axis scales.

For the small aspect ratio cantilever, measurements were made using two identical cantilevers. For the large aspect ratio cantilever we used a fresh piezoelectric cantilever, and one that had been used multiple times, so it was pre-strained i.e. it was not initially flat for $U_\infty = 0$. We did not observe the same behavior after multiple use of the small aspect ratio cantilevers. With the video data we were able to perform image analysis using in-house MATLAB codes to

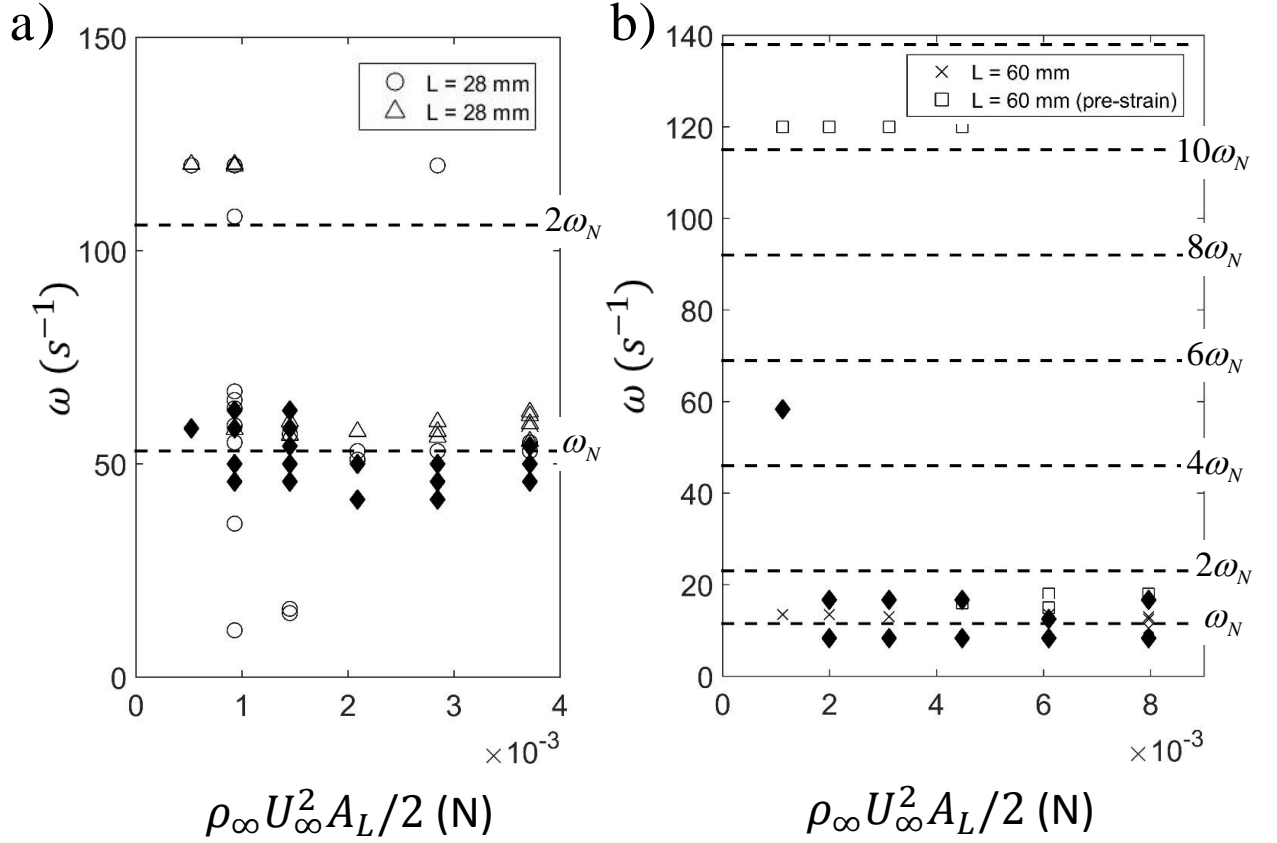


Figure 1.9: Cantilever tip displacement and measured voltage frequencies versus aerodynamic loading. Open symbols correspond to measurements made using tip displacement data for aspect ratios a) 1.6 \circ , \triangle and b) 3.6 \times , \square . Note: the same relationship between the open symbols and corresponding experiment are used in the figures that follow. The closed symbols \blacklozenge correspond to frequencies measured using oscilloscope data.

estimate values for $u_s(L)$ and $u_\omega(L)$. The steady component to the cantilever tip displacement is reported as the time averaged displacement $u_s(L) = \bar{u}(L, t)$, and the amplitude of the unsteady component, $u_\omega(L) = [\max|u(L, t)| - \min|u(L, t)|]/2$, was measured as half the difference between the maximum and minimum tip displacement.

In Fig. 1.8 we plot the piezoelectric cantilever tip displacement $u(L, t)$ versus elapsed time. Data sets for multiple free stream velocities are shown on a single graph for an aspect ratio of 3.6, Fig. 1.8(a), and 1.6, Fig. 1.8(b). For the larger aspect ratio cantilever, Fig. 1.8(a), there are small displacements with small-amplitude vibrations at lower speeds with an increase in the magnitude of both the displacement and vibration amplitude at higher ones. The same trend is true for the lower aspect ratio cantilever shown in Fig. 1.8(b). The vibration amplitudes, relative to the steady displacements, suggest the lower aspect ratio cantilevers produce amplitudes that are closer in magnitude to the time averaged displacement i.e. $u_\omega/u_s \approx 1$.

Estimates of the vibration frequency versus aerodynamic force, taken from analysis of image data (open symbols) and also from voltage measurements (filled symbols, oscilloscope data not shown) are plotted in Fig. 1.9. The maximum dynamic force on the cantilevers varied from approximately 8 mN for the higher aspect ratio cantilever to 4 mN for the lower ones. The first horizontal dotted line represents the natural frequency to first normal mode oscillations, $\omega_N \approx 0.6\sqrt{EI/\rho AL^3}$ (Zhao and Yang, 2015), and the additional dotted lines are integer multiples that represent higher harmonics. High frequency vibrations appear at lower loading with frequencies reaching as high as 6 times the natural one for high aspect ratio cantilevers. This is most likely due to noise in the FFT transformation of the waveforms, which is greater at smaller vibrational amplitudes. In general, though, most of the data points at higher aerodynamic loading are located in the vicinity of the natural frequency of approximately 10 and 50 Hz, for the short and long cantilevers, respectively.

Next, we plot the average cantilever force, based on the steady displacement $u_s(L)$, versus aerodynamic force for the two sets of cantilevers, in Fig. 1.10. The expression for the force measured from the steady tip displacement, $F_s = 8EIu_s(L)/L^3$, was derived from the solution to the steady Euler-Bernoulli beam equation. The resulting force was much larger for the

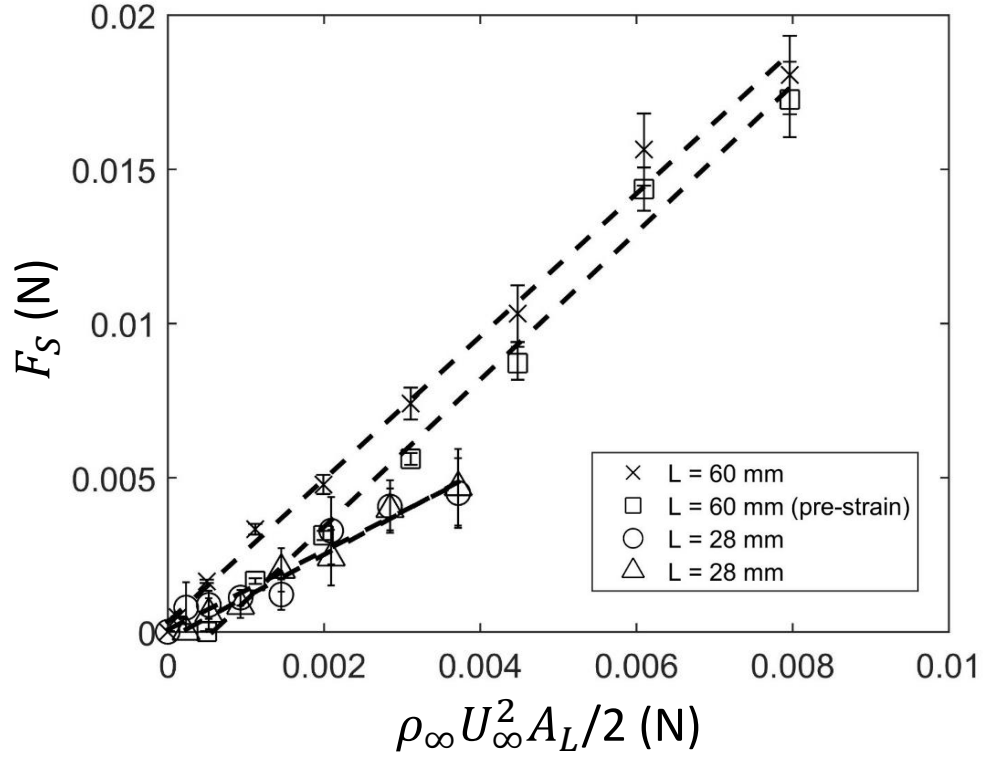


Figure 1.10: Force measured from steady tip displacement of a vibrating cantilever $F_s = 8EIu_s(L)/L^3$, versus dynamic force. The dotted lines $--$ are best fits with slopes of C_s .

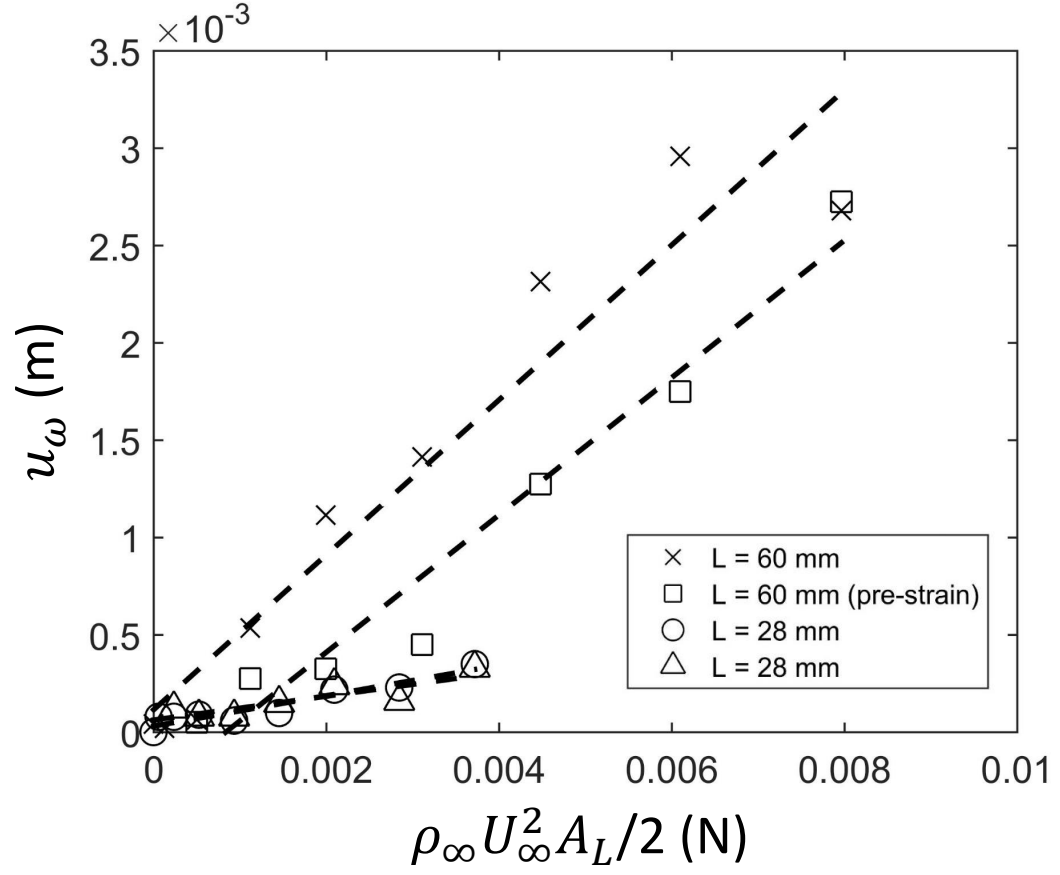


Figure 1.11: Amplitude of the vibrating cantilever tip $u_\omega(L)$ versus aerodynamic force. The dotted lines — are results of numerical simulations of Eq. 1.1 for values of C_ω shown in Table 1.

higher aspect ratio cantilevers at about 20 mN versus a maximum of 5 mN for the lower ones. Also shown in the plots are best fit lines through the data points, the slopes of which were used to determine C_s . The slopes are similar for each aspect ratio cantilever including a comparison of the pre-strained and flat cantilevers. The next comparison between the two aspect ratio cantilevers is in the corresponding vibration amplitude versus aerodynamic force, shown in Fig. 1.11. The maximum vibrational amplitude of the higher aspect ratio cantilevers are approximately 10 times greater than the ones generated by the lower aspect ratio ones. The dotted lines appearing in this graph are results of solutions to Eq. (1) using C_s estimates from the data shown in the previous graph, and varying C_ω to find the best fit. A summary of the coefficients for the displacement and vibrational forces are shown in Table 1.

Table 1.1: Aerodynamic forcing coefficients $F_i = C_i \rho_\infty U_\infty^2 A_L / 2$ where $i = s$ or ω corresponding to steady and unsteady forcing, respectively.

Aspect Ratio	C_s	C_ω
1.6	1.37	0.07
1.6	1.28	0.07
3.6 (pre-strain)	2.38	0.03
3.6	2.31	0.04

The effect of the measured differences in vibrational amplitude, relative to the displacements, in terms of the generated voltage are shown in Fig. 1.12 where we plot the measured voltage difference, ΔV , averaged over many samples taken for a single beam at a given speed, versus the vibrational force, $m\omega^2 u_\omega$ where $m = \rho AL$. The scaling for vibrational force was determined by inserting $u(x, t) = u_s(x) + u_\omega(x)e^{i\omega t}$ into the Euler-Bernoulli beam equation then separating the steady and unsteady components. The voltage difference is reported as the maximum minus the minimum measured values. The maximum measured ΔV was approximately 0.4 and 0.6 V, at 3.6 m/s, for the high and lower aspect ratio piezoelectric cantilevers, respectively. The dotted line is a best fit for all of the experimental data with a slope of approximately 3.8 V mN^{-1} . This value is larger than the one reported by the manufacturer, although their testing method was not the same.

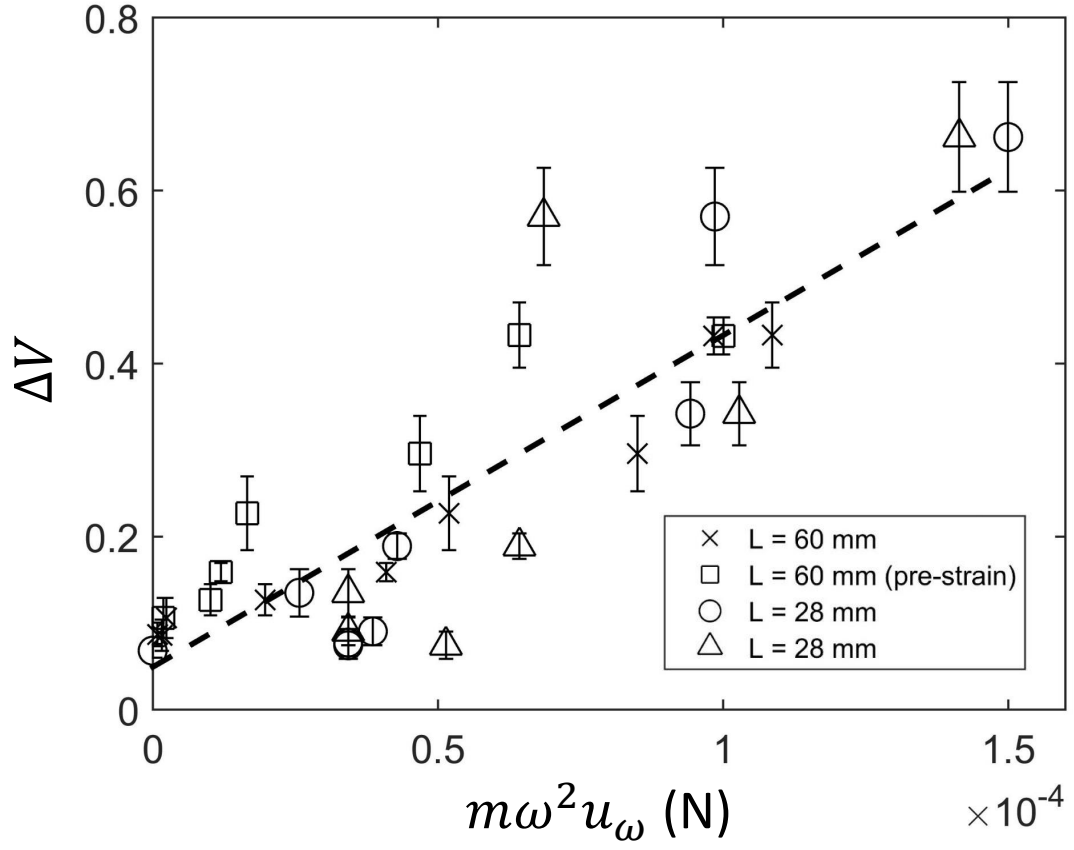


Figure 1.12: Voltage versus vibration force $m\omega^2 u_\omega$ where $m = \rho AL$ for the low and larger aspect ratio piezoelectric cantilevers. Dotted line '—' is the best fit for all of the experimental data points.

It appears that the lower aspect ratio piezoelectric cantilevers are more efficient i.e. for lower aerodynamic force, lower due to the smaller area, these cantilevers are able to produce a larger voltage difference. This does not come without some sort of a cost, though, because the higher aspect ratio cantilevers appear to be more reliable in terms of voltage production according to Fig. 1.12; where a greater number of the lower voltage data points, which correspond to the higher aspect ratio cantilevers, follow the best fit line. In regards to a cantilever's vibrational amplitude it appears to be directly proportional to the displacement. Therefore, larger displacements and vibration amplitudes possibly both contribute to the pre-strain that develops in the higher aspect ratio piezoelectric devices when used multiple times. But the effects of pre-strain do not appear to significantly affect the measured voltage. Clearly more work needs to be done in the area of aging for these devices before any firm conclusions can be made. With respect to the vibrational frequency, the lower aspect ratio cantilevers vibrate at relatively higher frequency (50 versus 10 Hz) which correlates with their higher voltage output. Since they vibrate near the natural frequency then even smaller length cantilever may be more efficient than the lower aspect ratio ones used here. But the increase in frequency may lead to issues concerning noise pollution given that the frequencies we observed are in the audible range.

1.5 Summary

The results shown in Fig. 1.10, Fig. 1.11 and Fig. 1.12 summarise that higher aspect ratio beams tend to have higher loading when compared to the low aspect ratio beams. This can be seen when the magnitudes of the loading terms are compared. These results will be compared with the soap film experiment results later in Chapter.5. Also, we see a good agreement with the literature since low aspect ratio beams were found to be more efficient in terms of harvesting electricity that have lower aerodynamic loading as seen in Fig. 1.12. To explore the flow behavior on these cantilevers we built a visualization technique to visualize the flow and a set of image processing tools to analyze the images. For our research we implement a vertically falling soap film tunnel to visualize the flow. Similar experiments, comparable with that of the wind tunnel experiments, will be performed. The results acquired with a dynamically

similar test models in the soap film experiments are then used to validate the wind tunnel experiments. The frequencies of beam vibrations and the vortex shedding frequency are some more parameters of focus.

CHAPTER 2. FLOW VISUALIZATION AND MEASUREMENT TECHNIQUES

In this chapter we will discuss a brief history of soap films and why it is important to visualize the flow. We rigorously describe the experimental setup of our flow visualization technique, and also explore the measurement techniques for various quantitative parameters such as freestream velocity, film thickness, flow visualization, etc. that are necessary for a quantitative measurement. Furthermore the operation of the soap film experiment and the maintenance conditions are elaborated upon. The structure of soap film tunnel is introduced. The significance of various controlling parameters for the soap film experiment and properties of the soap film and beams are also discussed in this chapter.

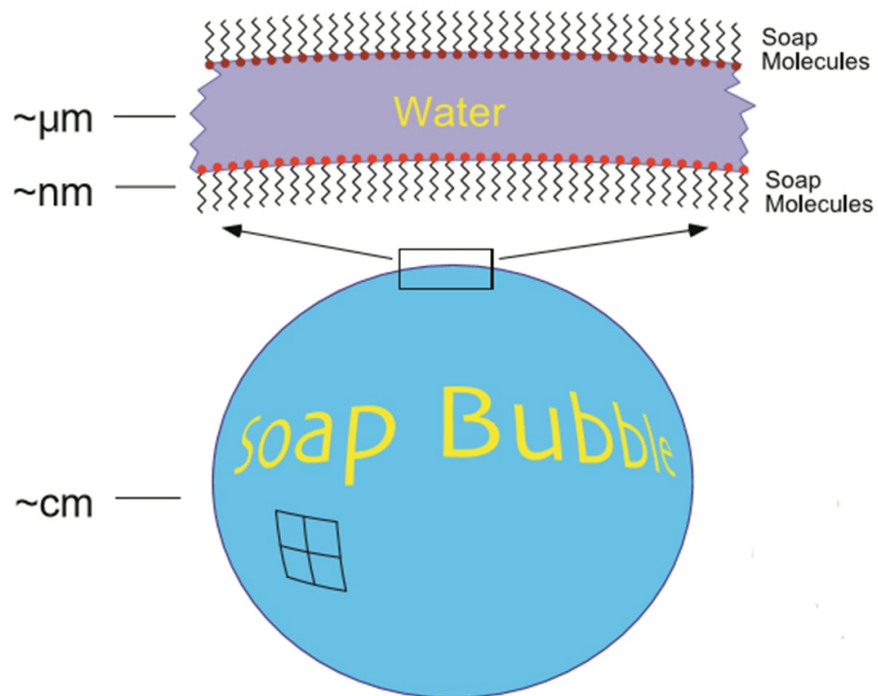
2.1 Introduction

Soap films have always been an object of curiosity until the work by Couder et al. (1989), where he investigated soap films as fluid dynamical systems. He utilized soap film as an experimental tool to visualize the flow structure of a two-dimensional towing tank. Since then, many experiments were carried out using soap film to simulate 2-D flow. Colour fringes on the surface of a soap film is the key to visualize the flow structure.

Soap films represent the closest physical approximation to a true two dimensional (2D) fluid. They are a good alternative for performing real experiments that are otherwise confined to the realm of theory or simulation. Surfactants like every day dish soap are generally constituted by molecules with two distinct parts: a hydrophilic polar head which is attracted to the polar water molecule, and some group of hydrocarbons, usually strung out in a tail, that is hydrophobic. This hydrophobic/hydrophilic duality also allows soap solutions to create films. The soap film constitutes a thick sheet of water covered by surfactant molecules on either sides as shown in Fig. [2.1b](#). Although soap films are an appealing candidate system for studying 2D flow phenomena,



(a) Soap Bubbles: The colours visible arise from interference of light reflecting off the front and back surfaces of the thin soap film



(b) Constituents of a Soap bubble
Source: Rutgers et al. (2001)

Figure 2.2: Soap bubble structure: Depending on the thickness of the film, different colours interfere constructively and destructively

there are still questions as to whether it is appropriately described as a 2D incompressible flow. In Chomaz (2002), he explains the 2D phenomena of the soap films and at what conditions they are valid. The condition was that the flow velocity should be comparatively equal to the Marangoni elastic wave velocity of the film. Based on the observations our soap film tunnel is assured to be a good assumption for a 2D approximation. Thickness variations in the film and air drag on the film surface can also affect the governing equations.

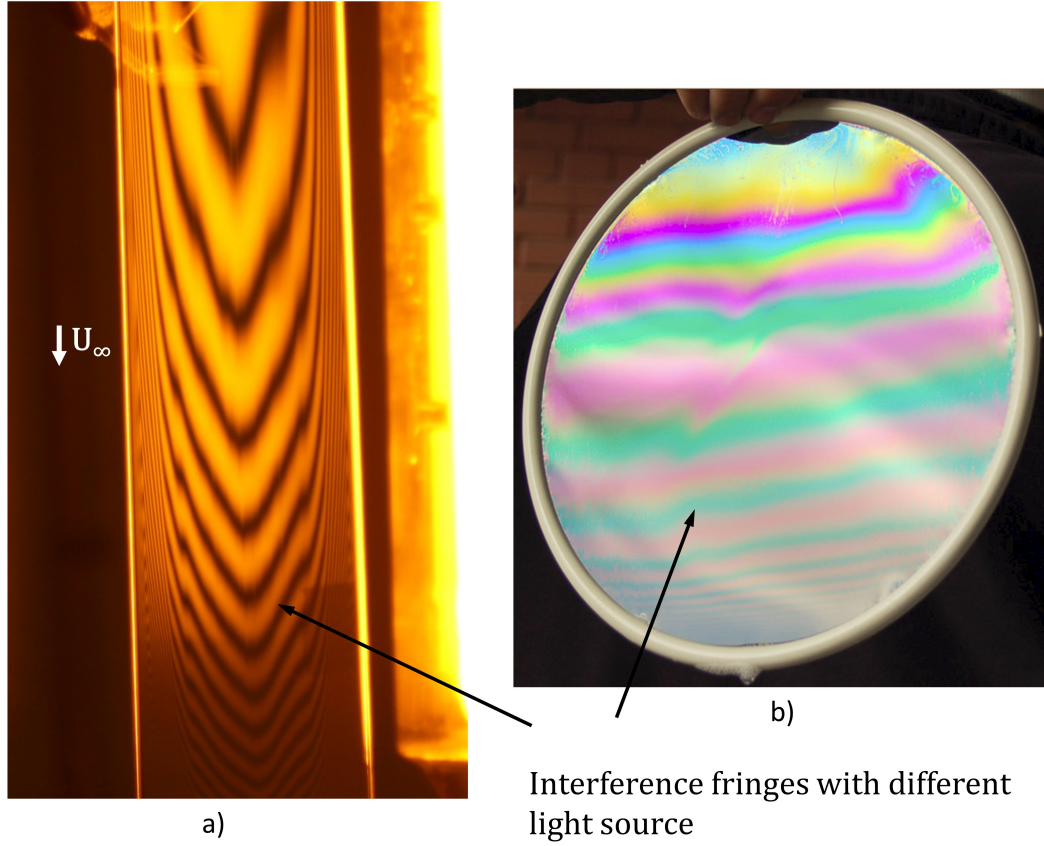
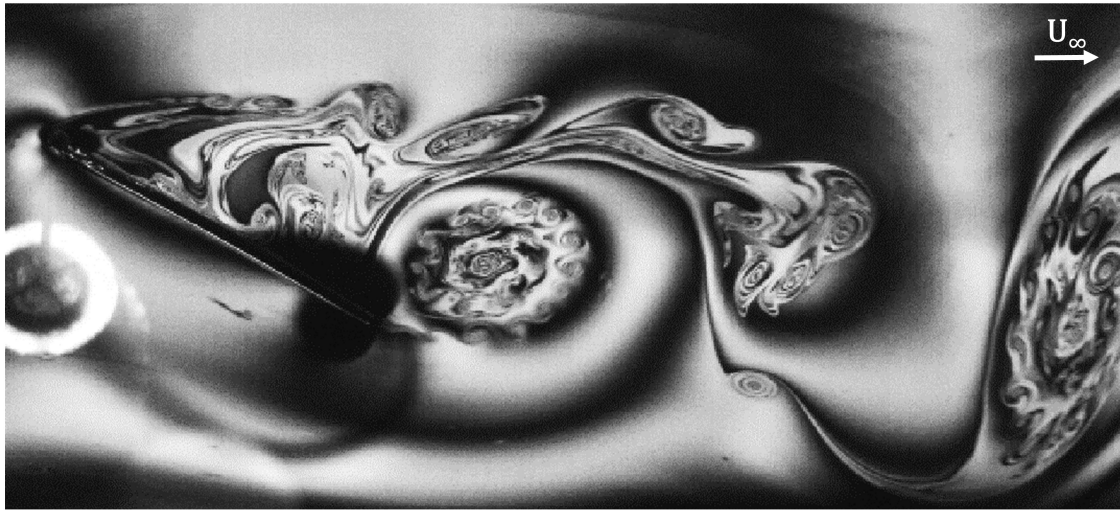


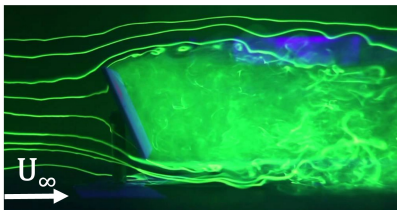
Figure 2.3: Soap film when interfered with an illumination source. a) Soap film between two thin wires. Image captured from our setup. b) Soap film in a circular hoop. Observe how the interference patterns converge downwards due to gravity (Source: <http://hyperphysics.phy-astr.gsu.edu>)

Soap films are excellent to visualise overall features as well as minute details of two-dimensional flows. The first documented work that makes use of soap films to visualise flows is that of Sir James Dewar in 1923, who visualised the flow due to a jet of air impinging on a hor-

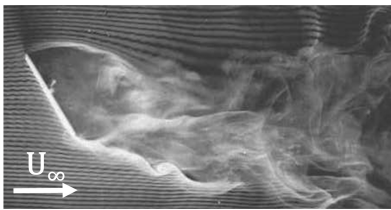


Soap film visualization

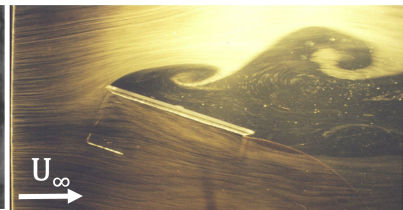
Some of the famous visualization techniques used for an inclined plate



Dye visualization



Smoke tunnel visualization



Hydrogen bubble visualization

Figure 2.4: Why soap films? A better technique pertained to our application

horizontal soap film suspended on a wire frame (Dewar, 1923). Later on, in the early 1980s, soap films gained widespread popularity as a flow visualisation tool. Of particular importance is the inspirational work of Yves Couder and co-workers, who studied wakes of cylinders that penetrated an otherwise quiescent soap film (Couder and Basdevant, 1986). Gharib and Derango (1989) invented a liquid film tunnel where a planar water jet pulls a soap film and thereby produces a horizontally moving soap film in which a number of experiments studying shear flows were conducted. Kellay et al. (1995) made a simpler version where gravity drives the flow vertically downwards between two guide wires. In the last two decades, several groups have adopted gravity-driven soap film tunnels to study a great variety of phenomena such as the shedding of vortices behind a cylinder in an otherwise uniform flow (Vorobieff et al. (1999)), structure in two-dimensional turbulence (Rivera et al., 1998; Rutgers, 1998), flapping of flags (Zhang et al. (2000)), passive swimming of a filament behind a cylinder that sheds a von Karman wake (Jia and Yin (2009)) and the inverted drafting of two flags that flap in a tandem configuration (Ristroph and Zhang, 2008). This chapter first gives a general introduction to soap films. Part of the content is based on the books by Isenberg (1992) and Boys (1890), that both thoroughly explains many aspects of soap films in an easy-to-digest language. Secondly, an experimental set-up that makes use of a flowing soap film to visualise two-dimensional flows is presented. The relevant properties of the flow tunnel are given, and the link between measured thickness variations and the underlying flow in the soap film itself is discussed, as is soap film tunnels as a testing ground for experiments on two-dimensional incompressible Newtonian flows.

2.2 Experimental Setup

The current design is inspired from that of Rutgers et al. (2001), who have specified every little intricate detail in their paper. Although inspired, we still have a variety of modifications worked to our setup to achieve a stable flowing soap film. We will be discussing those changes as we go through the process step by step. Typically a vertical soap film tunnel consists of three sections. a) Fluid injection section b) Expansion section, c) Test section and d) Convergent section. Few of the main components include a reservoir, metal frame, a flow frame, flow-meter, a pump(motor), tubes and pipes, valves, thin nylon strings, and a weight. The actual setup

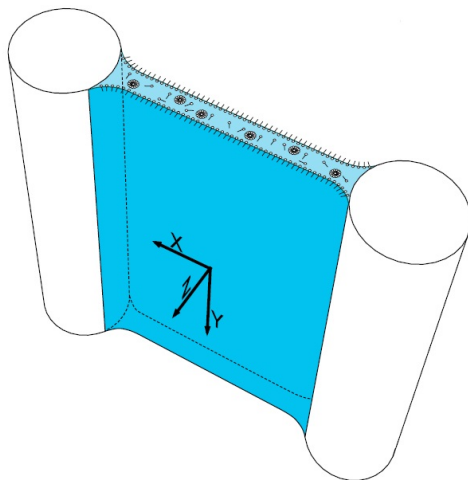


Figure 2.5: Cross-sectional view of a soap film between two vertical wires. The film gets attached to the wire at a contact angle called the Plateau border. The diagram is not drawn to scale. Approximate sizes are wire diameter 0.5 mm, wire spacing 8 cm, film thickness of order $4\mu\text{m}$, Rutgers et al. (2001)

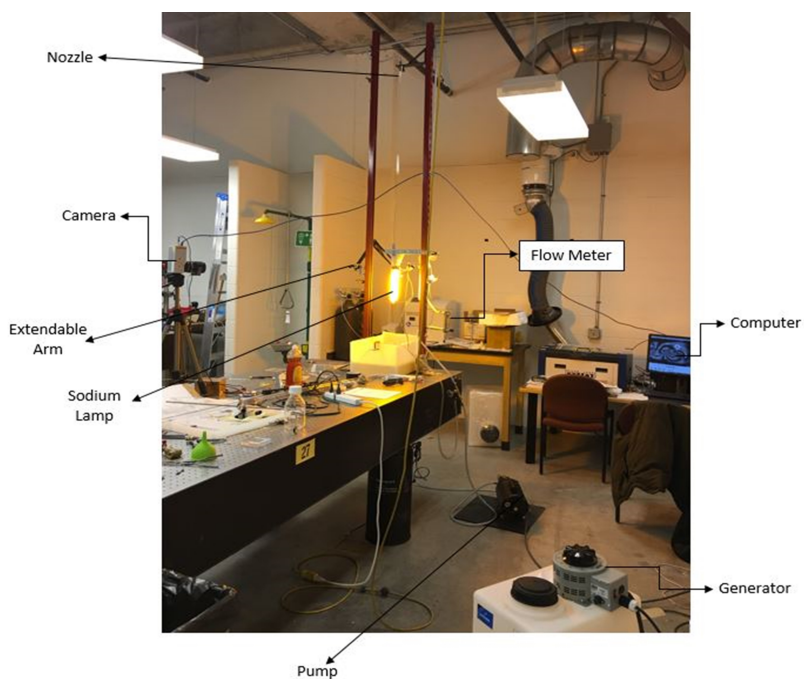


Figure 2.6: Actual setup of vertically falling soap films

is shown in Fig. 2.6. As we go along explaining different sections of the setup, Fig. 2.7, a schematic of the setup has been used as a reference.

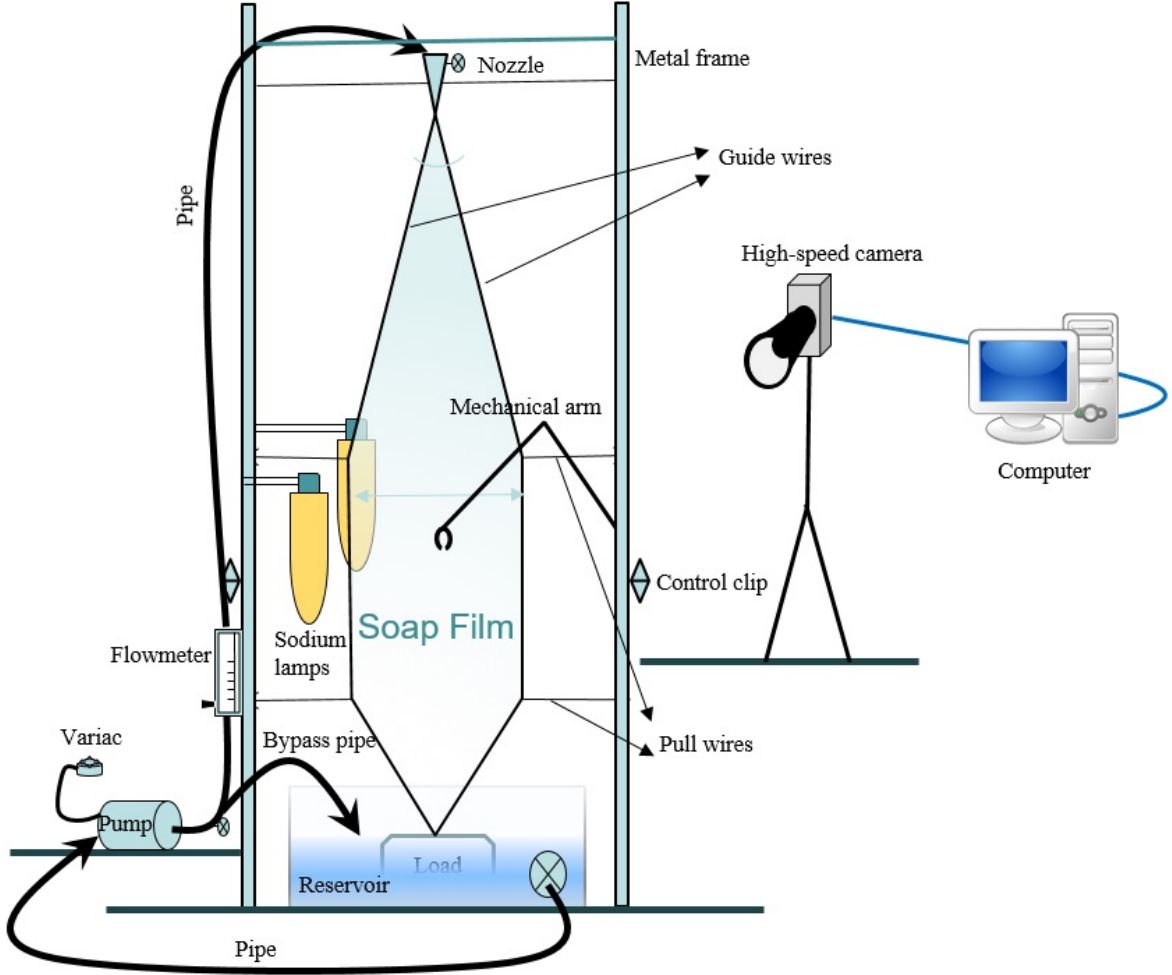


Figure 2.7: Schematic of the experimental setup

2.2.1 Fluid injection

A 4" long round conical nozzle with 1/16" opening from McMaster-CARR was used as our soap solution injecting tube. The round nozzle has been shaped to an elliptical shape so that the guide wires stay put at the vertex as shown in Fig. 2.8. To direct the flow into the reservoir to minimize spilling, we have guide wires that go through this nozzle and into the reservoir attached to a dumbbell. The guide wires are tied to the dumbbell tight enough to maintain a tension in these guide wires. These wires have a high strength to sustain the huge loads(13-15

lbs).

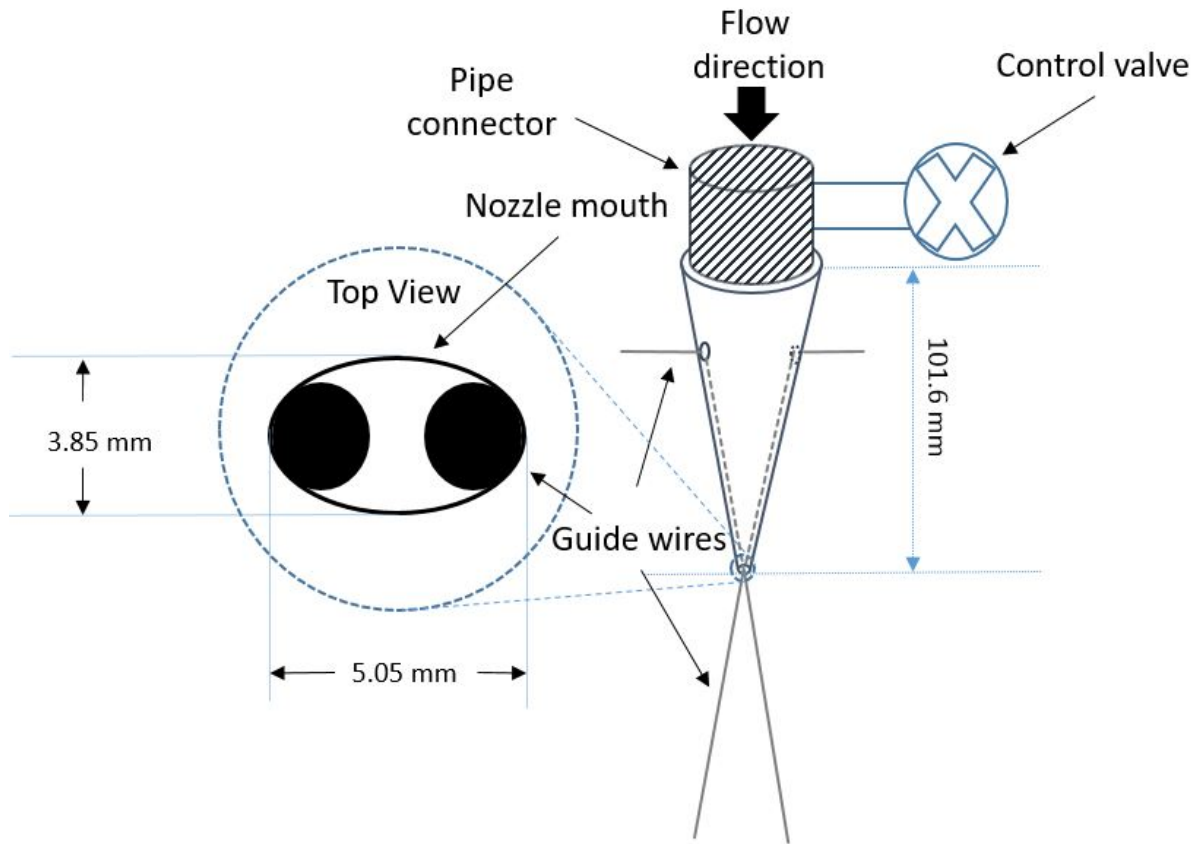


Figure 2.8: Schematic of the conical nozzle

2.2.2 Channel expansion

The expansion section is 53" long starting from the nozzle's mouth to the first set of pull wires. We have pull lines that are much thinner than the guide wires but of the same material and equivalent strength. We have 2 sets of these pull lines attached to the guide wires at some distance to help expanding the film to get a good rectangular test section. These pull wires are used for expanding the guide wires to produce a steady film and test section.



Figure 2.9: Conical nozzle with elliptical type opening

2.2.3 Channel test section

The test section is the region containing the parallel guide wires. The test section is 28 cm long where the flow visualization is performed. We have chosen to hold the guide wires apart by attaching thinner nylon pull lines directly to the guide wires. Surgical hooks can also be used to pull these guide wires but is more prone to puncture the film. Tying thinner nylon pull lines to the guide wires minimizes the time required to regenerate the film and causes the least intrusion to the flow. The pull lines must, however, be guided fairly accurately to ensure a reproducible channel width. Tying the pull lines to the guide wires is best done with a type of knot outlined by Rutgers et al. (2001).

We have control clips that are used to control the test section width for the experiment as shown in Fig. 2.15.

No matter how high the tension in the guide wires, the surface tension of the film will pull them slightly inward. For channels of different widths the guide wire bowing becomes a large fraction of the total channel width. Further increasing guide wire tension is impractical since it causes difficulty in operating the pull wires. This setup is very useful for studying laminar channel flows where it is important to have a well defined distance from the inlet of the channel.

It is also the region where we can carefully place different test pieces inside the film for the study of beam vibrations, displacement and vortex shedding. For all our experiments we try to maintain a constant test section width of 7.5 cm.

2.2.4 Channel contraction

The fluid is collected at the bottom of the channel in the reservoir as seen in Fig. 2.10. In the design a dumbbell was immersed in the soap solution. The wires must be pinched together manually beneath the fluid surface to regenerate the film. Also, for high flow rates a significant amount of foam can be generated where the film impacts the reservoir fluid surface. The contraction section is made by tying both guide wires to the dumbbell. This method allows the guide wires to be moved entirely by the pull lines and cuts the film regeneration time down to seconds. The contraction is best kept gradual, though it can be more abrupt than in the expansion section. In a typical case the channel contracts from a 5 cm wide test section over

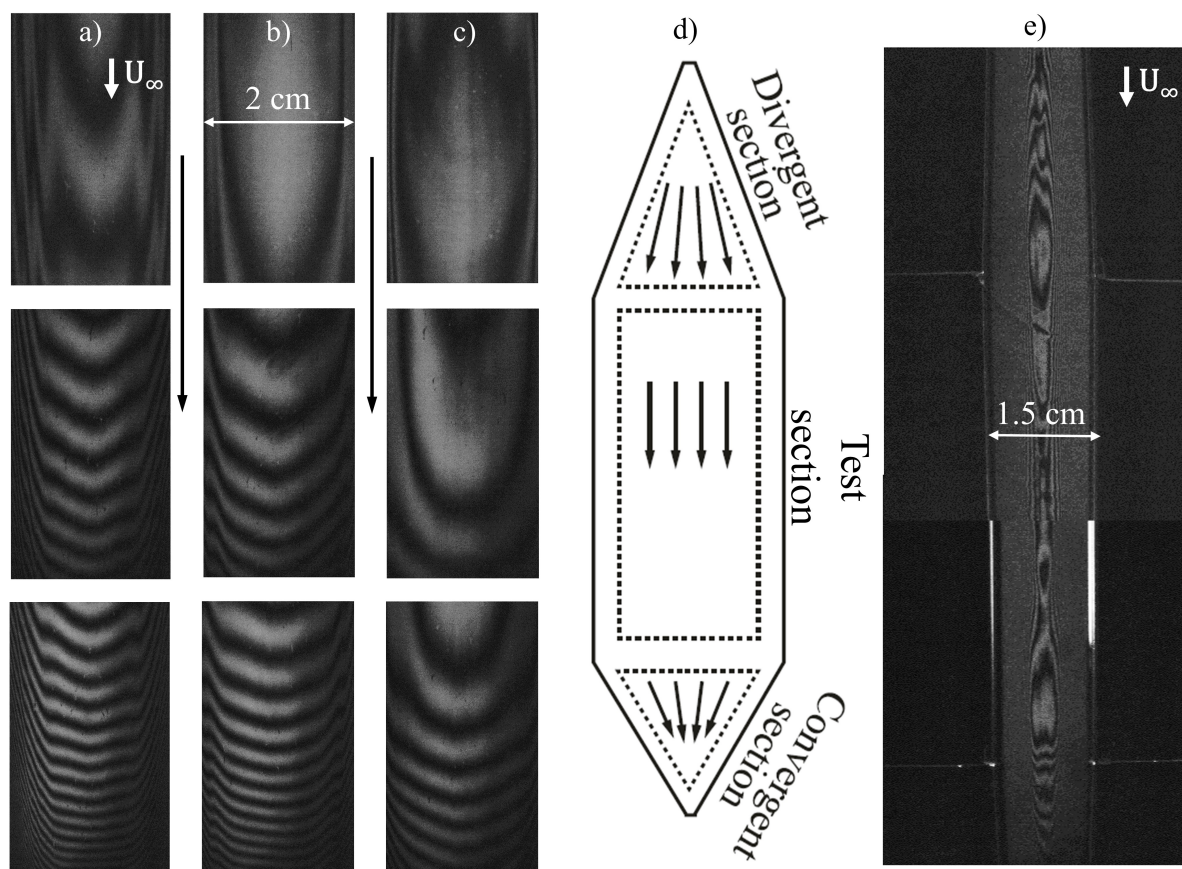


Figure 2.10: All 3 sections of the soap film (top to bottom) for 0.3, 0.5, 0.8 GPH (left to right) for a 7.5 cm channel width is shown. Note how the interference patterns depict the magnitude and direction of the flow. d) and e) are schematic and actual setup images respectively. We can see the pull wires in e) ready to expand the soap film.

20 or 30 cm making 18° with the vertical. More abrupt contractions apply unnecessary tension to the pull lines and can cause violent flows which may rupture the film. After the contraction section the fluid is collected in a lower reservoir. It can be recirculated to the nozzle with a pump. We have used a motor pump to drive the flow to the nozzle at the top. Prolonged recirculation will lead to a thickening of the mixture as some evaporation occurs from the surface of the film, and can cause a buildup of dust and other contaminants.

The flow is directed inside the reservoir and then the cycle continues. The main purpose of the contraction channel is to not spill the soap solution when it is driven at high speeds by the motor.

2.2.5 Flow illumination and thickness of the film

Visualizing flow is an extremely important aspect of any program of fluid dynamics experimentation and there are various methods of doing so with flowing soap films. The simplest visualization method does not require addition of contrast agents to the flow. It is purely based on the optical interference between the front and back surfaces of the film, which is the source of the various colors of soap films. A quarter wavelength change in thickness of the film 0.1 mm, in water will change the interference condition from constructive to destructive. When viewed under a monochromatic light, the thickness variations in the film are visible as dark and bright fringes. Looking at a typical photograph of a soap film flowing past a cylinder, it is pretty clear that the contrast variations act as a tracer in the flow.

The change in soap film thickness can be revealed by Interferometry (Greco and Molesini, 1996). This is the most common method employed. The incident light is reected from two liquid-air interfaces of the soap film. The thickness of the film is comparable with the incident light wavelength. As a result, the reected light from two interfaces interferes and thus fringes form. These interference fringes reect the changes of the film thickness. Chomaz (2001) theoretically proved that the thickness of soap film is related to the pressure and vorticity fields under the condition that the flow velocity is much lower than the Marangoni elastic wave velocity of the soap film.

In order to visualize the flow structure clearly, monochromatic light source is preferred.

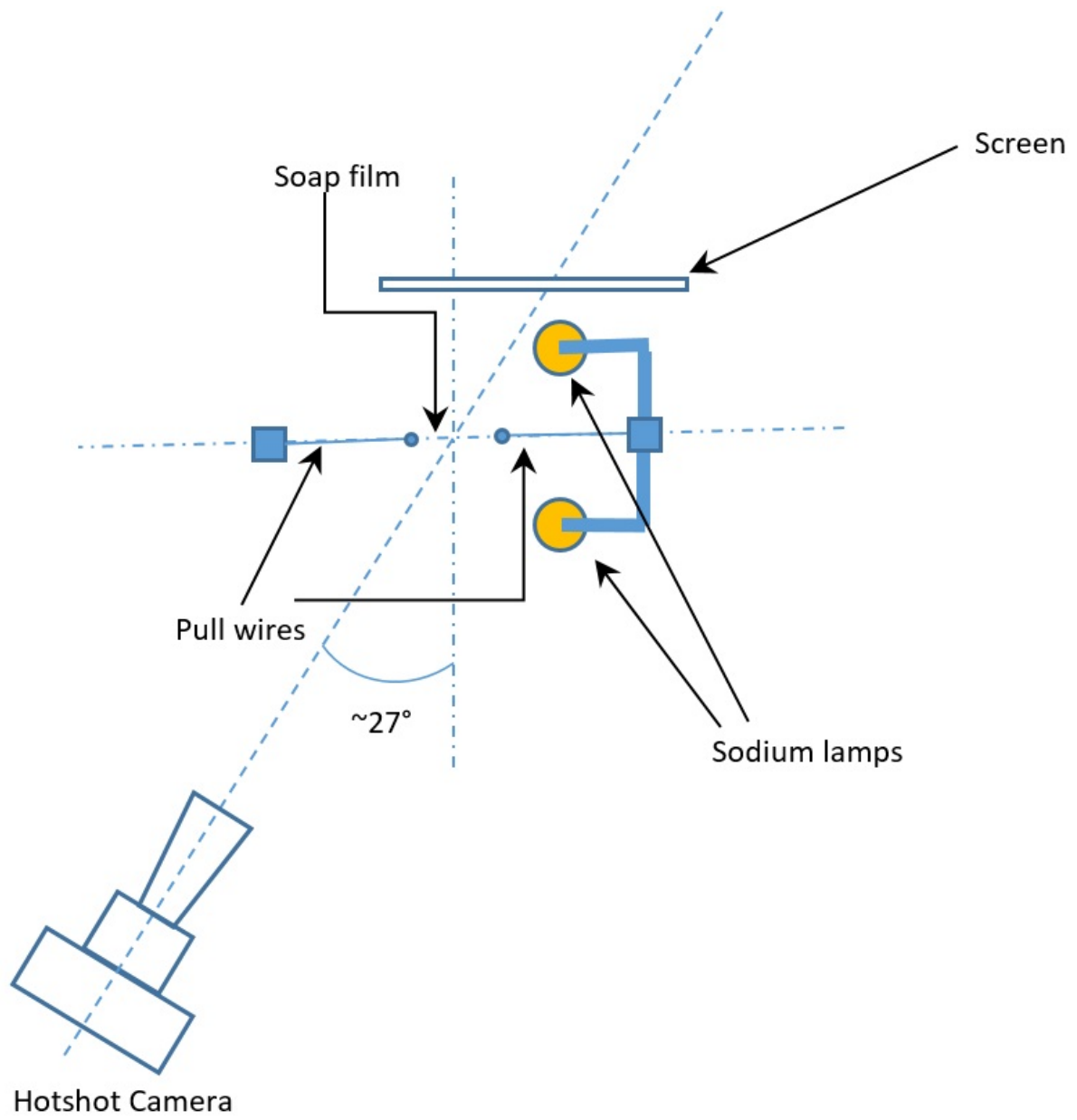


Figure 2.11: Top view of the soap film experiment setup

Monochromatic light can reveal the thickness change of the soap film with clear interference fringes. A sodium-vapour lamp features well monochromaticity, high brightness and good luminous efficiency. Low pressure sodium lamp(LPS) has higher efficiency and better monochromaticity than high pressure sodium lamp(HPS) but its power is much lower than HPS lamp. In our studies, LPS lamps are used as the light source. Fig. 2.12 shows the circuit of the LPS lamp. With the increase of time, the brightness of the lamp is gradually increased, and the spectrum is gradually enriched. The interference fringes of wide spectrum are not as clear as monochromatic light. But at the time the lamp has just started, the brightness of the lamp is not enough to meet the requirement of a high speed camera to record the interference fringes. Thus in the experiments, the LPS lamp needs to be turned on for a while until the brightness is sufficient. The interference fringes recorded by cameras are mixed sodium yellow light with other spectrum. The LPS lamp is a gas-discharge lamp. Its brightness changes periodically with the AC voltage. Fig. 2.12 shows the circuit design. For visualizing the vortex structures and the vibrations of the beam in the soap film, two sodium lamps are used forth and back of the film.

We used a high speed Hot-Shot camera to capture these visuals. The camera is capable of capturing images at more than 10,000 fps. Since the capturing window limit is sensitive to the fps (frames per second) value that we select, we are limited to 5000 fps to achieve a good resolution of both, the beam's vibration and vortex shedding.

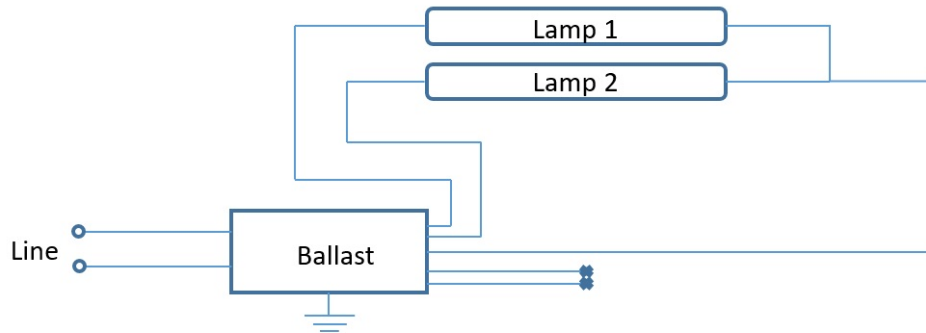


Figure 2.12: Circuit diagram of low pressure sodium lamps with a ballast

2.2.6 Materials considerations

We use practi-shim plastic sheets as our flexible beams. We use four different lengths i.e. 7.5 mm, 10 mm, 20 mm, 25 mm to get an understanding of the length dependency. Have a table that gives the description of the test pieces in detail.

Table 2.1: Data for test pieces

Cantilever Type	Thickness	Width
Rigid	0.0762 mm	1 mm
Semi-flexible	0.0508 mm	1 mm
Flexible	0.0381 mm	1 mm

Soap solution is corrosive and prolonged exposure will corrode most metals including many stainless steels. The fluid metering valve should therefore be very corrosion resistant. If the soap solution is to be recycled, the tensioning weight must be protected since it can contaminate the soap solution. Our dumbbell was coated with a very thick rubber material which delayed corrosion.

The guide wires and pull lines are made of monolament fishing line. Berkley trilene super strong wires are used for both guide and pull wires. Guide wires should be of a heavy gauge, in our case, 0.7112 mm thick, and capable of supporting about 20 kg. Thinner guide wires caused problems with film stability, probably because they cannot properly guide the very thick film near the injection nozzle. Pull lines should be thinner 0.3 mm thick, capable of supporting about 23 kg to minimize the intrusion on the flow. Thinner pull lines are also less rigid and more easily guided away from the pull points.

Even though our flowing soap films can last for more than 5 hours, breakage occurs more frequently during experimentation. Each rupture will send down a mist of soap solution which will cover an appreciable area depending on the channel height at the base of the apparatus. In the middle of the test section the fallout is less severe but one should take care to protect any delicate instruments, such as the electrical circuit used for the lamps by keeping them some distance from the film, or by wrapping them in plastic.

2.3 Operation

The goals are to create a long lived film having nearly constant thickness and flowing with a uniform velocity. Once an apparatus, such as in Fig. 2.6, has been built, an optimum soap solution must be prepared, then injected from a nozzle of the right shape into the channel under the right ambient conditions. This section will commence by describing some typical situations and how they relate to the operational parameters.

2.3.1 Flow control and channel geometry

Initially we only used two valves to control the flow i.e. a gate valve and a ball valve. But the motor was running the soap water with very high pressure and thus at high speeds, the soapy water led to spilling everywhere from the nozzle. To control this we used a bypass pipe that goes into the reservoir, which we set up with another ball valve. This bypass is a part of the tri-connection, with the gate valve and the pipe coming from the motor as shown in Fig. 2.13.

The setup now has three valves that can be used to control the flow. The gate valve and the ball valve that is located right above the fluid injection are always kept open during the operation of the experiment. The ball valve located near the reservoir at the pipe connecting the bypass pipe and the gate valve is used to control the flow. This valve proved to better flow-rate control, but due to very minute differences in the control handle, we were still unable to form the soap film. To further increase control over the flow and measure the flow rate, we added a flow-meter with range from 0-2 GPH (gallons per hour). We found the optimum range to form a stable soap film was from 0.3-1 GPH, after which the flow starts to become unstable and film formation becomes difficult.

Videos were captured at flow-rates with 0.05 GPH increments, starting from 0.3-0.8 GPH.

As shown in Fig. 2.15, the two guide wires were pulled to obtain a film flow channel. This is performed with the help of channel control clips that pull the guide wires upon rotation. This helps to reduce any boundary effects that may rise from the guide wires.

If the film breaks, one simply releases the tension on pull lines, allowing the weight to pull the guide wires together until they touch. Once sufficient soap solution has dripped from the

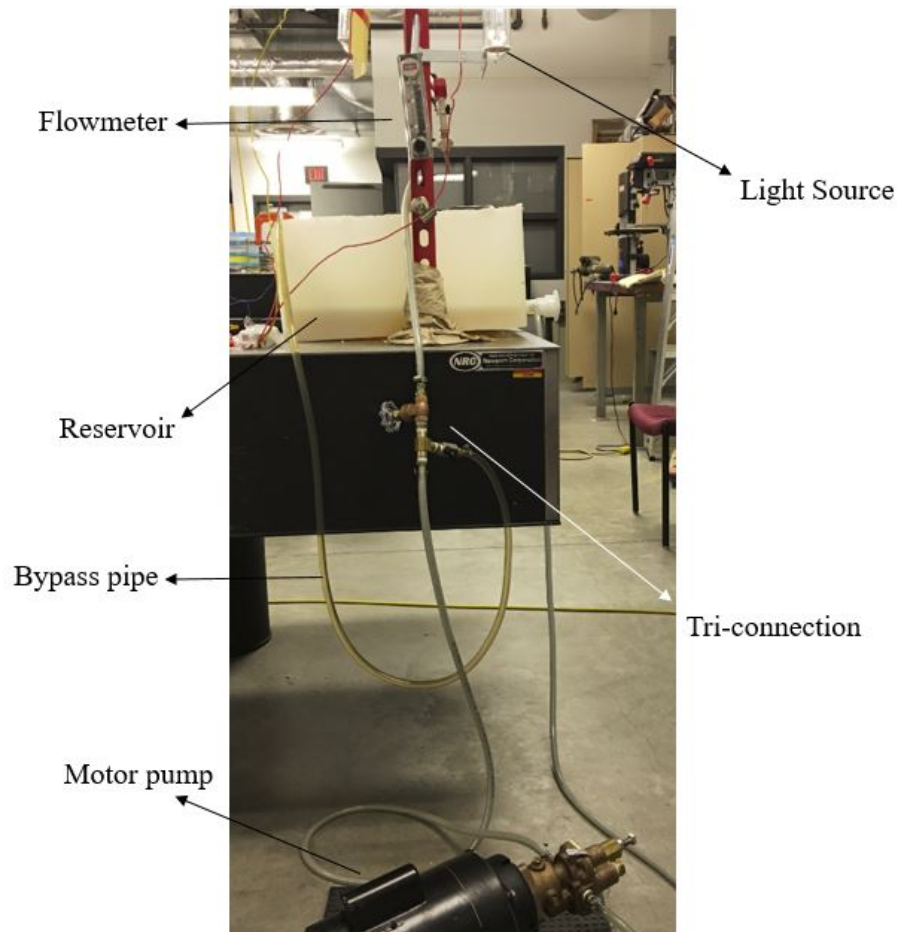


Figure 2.13: The tri-connection with the bypass pipe to lower the pressure of water driven by the motor



Figure 2.14: The flowmeter from KING instrument company, of 7520/7530 series with a bl-float that can sustain up to 125 psig water at a max temperature of 130° F

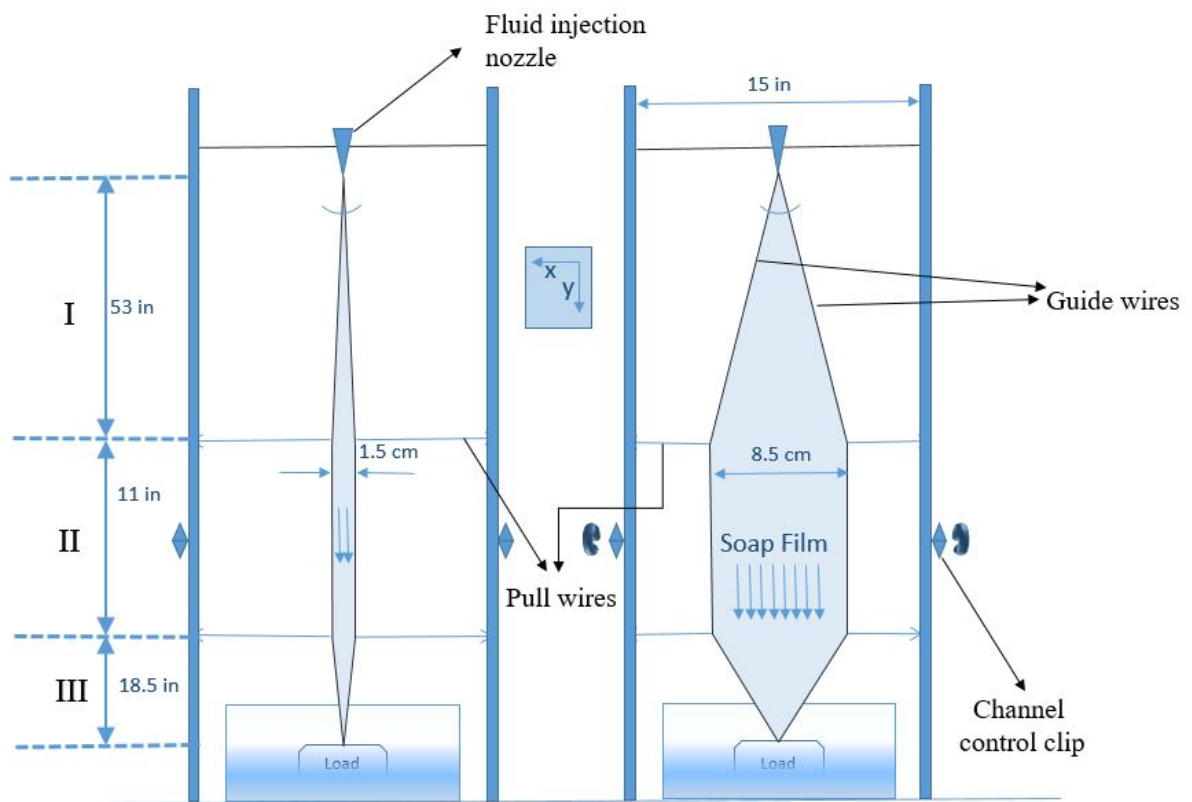


Figure 2.15: Soap film formation process

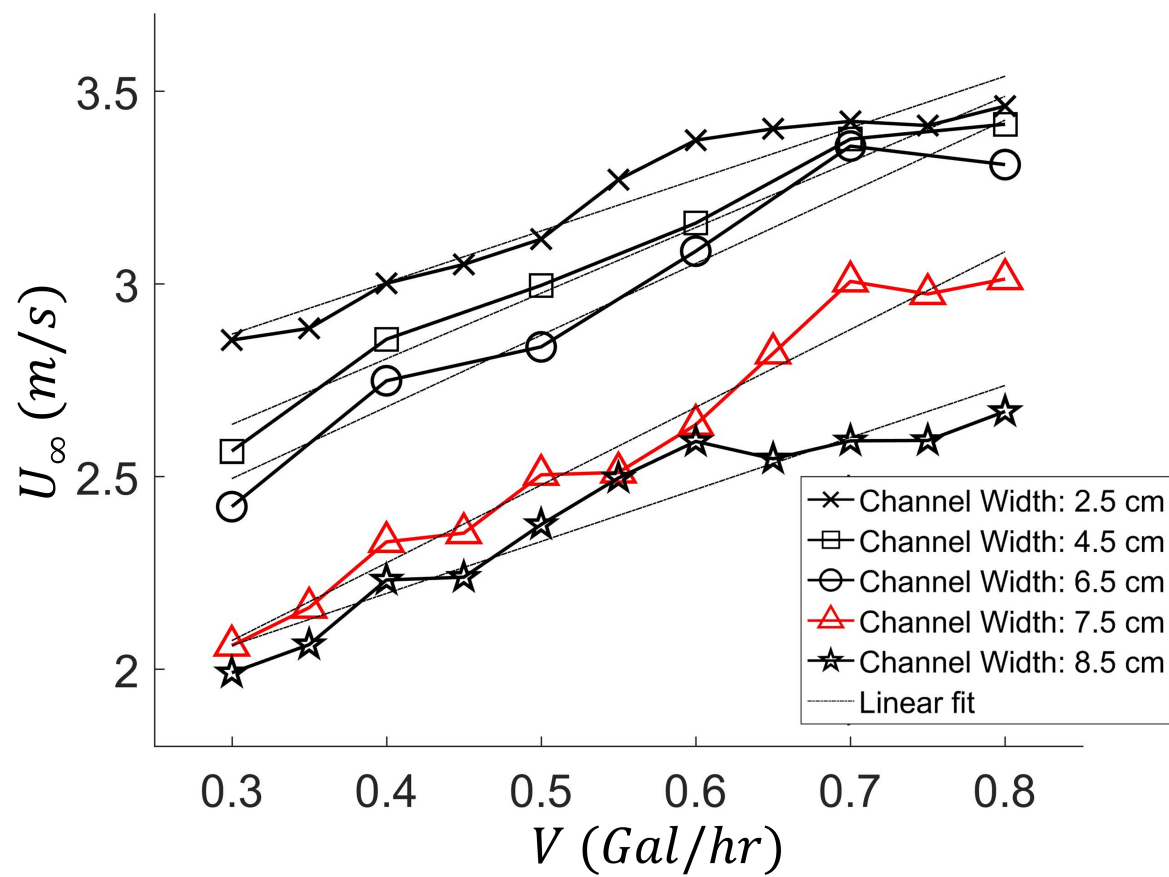


Figure 2.16: Freestream velocity for various channel widths

nozzle to wet the entire length of the guide wires, tension is reapplied to the pull lines, and a new film is formed.

2.3.2 Optimal soap solutions

We have obtained the best results with a mixture of 3%—5% percent liquid dishwashing detergent SMILE from Walgreens and 97%—95% percent tap water. The flowing films in the laboratory have lasted up to 5 hrs, and we have made lms 10 cm wide which last for minutes. Significantly lower soap concentrations(>3%) lead to more frequent breakage. The soap solution is above the critical micelle concentration but we have not performed a systematic study of the effects of solution constituents and concentration on film longevity. Much higher soap concentrations, or the addition of glycerol, make it much more difficult to generate uniform films. Such viscous fluids typically do not spread uniformly in the expansion section of the channel. Most of the fluid immediately separates from the guide wires and travels down the center in a thick jet no matter how gradual the channel expansion. (Put an image of soap concentration) The thin film on the sides then dries out and causes the film to rupture. This was observed to happen with a solution of >8% Dawn, and 80% water. The bulk viscosity of such a mixture is scarcely twice that of water and one would not expect such a large effect on the film flow. It should be noted that the soap solution will deteriorate with age and prolonged recycling is not recommended. For most experiments we did not recycle the solution, since it changes its characteristics due to evaporation, possible oxidation, and contamination with dust.

2.3.3 Surrounding conditions

We try to maintain no obstructions around the soap film that would lead to the film breakage. The temperature of the soap solution at the start of the experiments was 22.5° C, going to a peak of 45°C at the end of the experiments. The maximum time consumed the motor ran for some sets of experiments was 5 hours. This heated up the soap solution to almost 45°C.

Vertically flowing films are very robust under almost any conditions. Evaporation is likely to occur only within the air boundary layer surrounding the film. Frequent film breakage can be prevented in a number of ways: using a fresh solution, cleaning the guide wires and nozzle

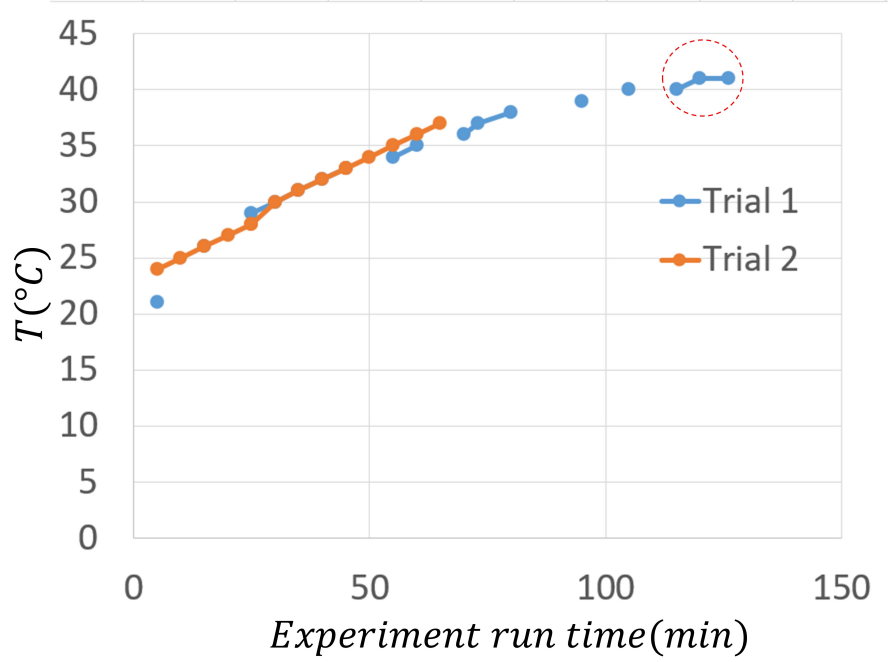


Figure 2.17: Temperature of the soap film with respect to the experiments runtime

with alcohol from time to time to remove soap buildup, avoiding large channel geometries which lead to separation of the main fluid stream from the guide wires and can lead to stagnation areas where the film is not replenished, and staying away from abrupt termination of the channel, which can cause the film to buckle and rupture. The film should also be protected from excessive air currents. Air currents can blow the film out of the plane defined by the guide wires and can cause waves to travel up and down the channel.

While a deflection of 1 mm will probably not severely affect the in-plane motion of the film, it does change the distance between the measurement instruments and the film.

2.3.4 Variety of test pieces in the soap film tunnel

In order to study 2D flow around an arbitrary body, they must be inserted into the film. These bodies, or as we call test pieces, should be pre-wet before carefully placing them in the test-section region. Breakage of film while trying to insert a test piece causes unnecessary soap spray. The technique to insert the test pieces is already explained in the operation section.

We tested a variety of test-pieces to verify the usability of the experiment. From the simplest shape such as a cylinder of diameter 2 mm to intricate shapes such as an airfoil of chord length

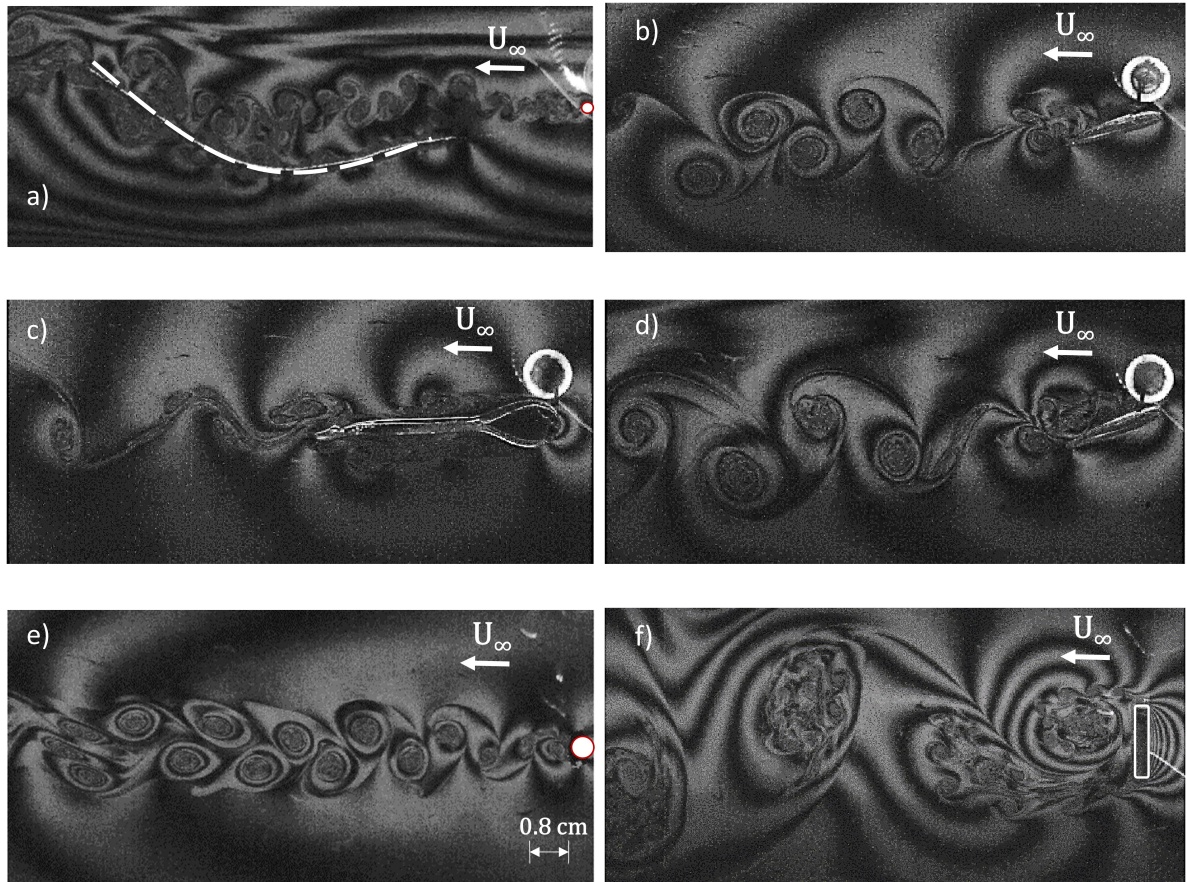


Figure 2.18: Visualization of the downstream vortex shedding for different objects in the soap film. a) Flexible filament, b) Cambered airfoil cross-section, c) Flexible airfoil cross-section, d) Symmetric airfoil cross-section, e) Thin cylinder, f) Thick rectangular plate

15 mm. We tested two different airfoil cross-sections, one with zero camber (symmetric) and a positive camber (asymmetric) as shown in Fig. 2.18. These test pieces are made of acrylic and was cut by a laser cutting machine at our lab. A flexible fibre is also tried to visualize the vortical structures and compare them with the works of Jia (2014). Our soap film was stable enough to test these different types of test pieces of varying lengths and sizes. Fig. 2.19 shows the vortex shedding and wake visualization downstream of a cylindrical cross section with increasing Reynolds number.

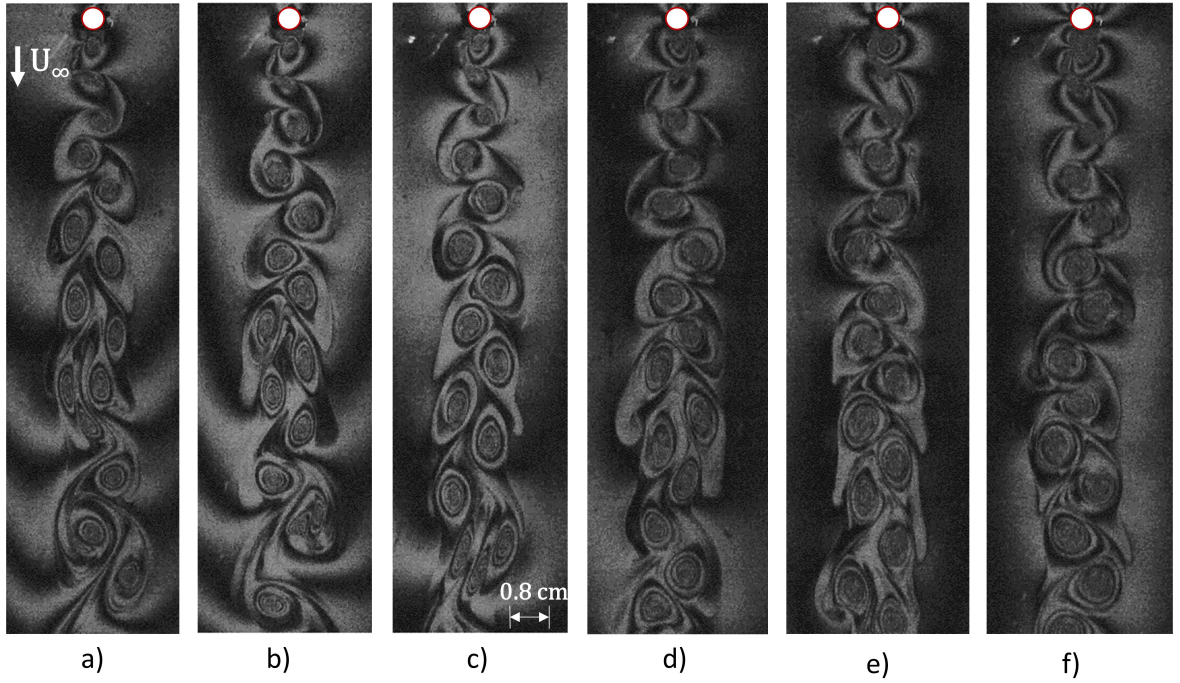


Figure 2.19: Visualization of vortices behind a cylinder of diameter 2 mm for Reynolds numbers ranging from, Re: 5500-8500

2.4 Measurement Techniques

Once the soap film experiment has been established, one would want to measure the properties and conditions of the soap film. Few of the crucial parameters for a quantitative analysis are the film velocity and film thickness. We discuss some of the methods used in general for these types of visualizations in the following sections.

2.4.1 Velocity measurement

Soap film flow speed is an important experimental parameter for soap film tunnels. Only accurate flow speed can determine the dimensionless flow parameters, such as Reynolds number and Strouhal number. We explore a few techniques from the literature and highlight the one we implement for our experiments. Flow-rate of the film is controlled by two parameters, the film's channel width and flow-meter reading.

From the literature, we found two ways the velocity of the soap film can be achieved.

a) Using the PIV technique

According to Rutgers et al. (2001), Particle Image Velocimetry (PIV) is a common technique for measuring flow velocity. By seeding tiny particles into the flow, PIV can track the movement of the particles. Assumption being the particles are moving together with flow at the same speed. Thus, PIV can be suitable to measure the flow speed. Due to the soap film being very thin, commonly used tracking particle with diameter above 5 μ m does not fulfil the requirement for the particle density per unit area. If too many particles are added into the soap solution, they can block the flux control valve and stop the flow. The author proposed to use titanium dioxide ultra-fine powder as tracking particles. However, the use of ultra-fine powder causes difficulty in illumination.

b) Tracking the defects in the soap film

This technique, is discussed by Jia (2014) in his Doctorate thesis. This alternative technique suggests to track the defects or dust particles or pollutants that are visible in the soap film. According to the author, after a long-time exposure to air, the soap solution is inevitably mixed with some dust. The dusts running in the soap film are visualized as defects in the interference fringes. By recording and tracking the motion of the defects, the flow speed can be determined.

And since the images are captured at 5000 fps, the tracking of defects becomes much easier and cost effective. From the results shown in Fig. 2.16 the technique proves to be a very reliable method. Since the velocity of these defects depend on the region of interest captured with respect to the channel area, we only stick to the core region for tracking them. The Fig. 2.20, depicts the velocity profile in the free-stream. We found a uniform velocity for all the flow-rates we list. Note: In the case of the zoomed version of data, the defects are affected by the wake region and the boundary layer over the cantilever beam and thus cannot be used to estimate the flow velocity.

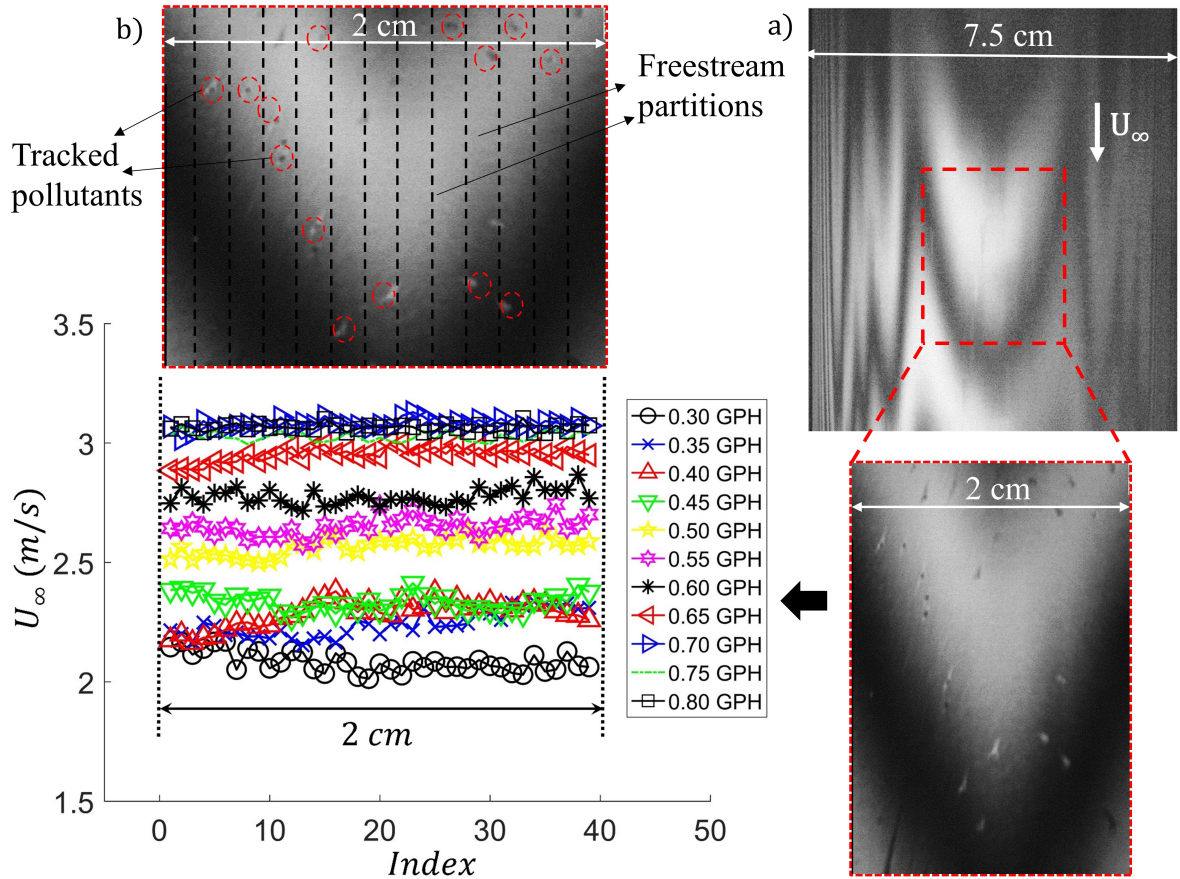


Figure 2.20: Velocity profile for a 2 cm window in a 7.5 cm channel width test section from 0.3 - 0.8 GPH. As a result we achieve an approximate uniform flow in this window.

The algorithm for the image processing is discussed in Chapter. 4 along with all other image processing techniques implemented in the research.

For the velocity profile of the film, we have a series of slices cut in the images vertically and then the defects are detected(if any are found) and are tracked in all those individual slices. The successfully tracked defects from upstream to downstream in all the 5000 recorded frames are averaged to get an estimation of the velocity. Thus, aiding us the velocity profile of the soap film.

We assume of the fluid flow to be constant at a particular channel width and the flow velocity is directly controlled by the flow-meter. For all of our experiments we used a fixed channel test section width of 7.5 cm that yields a good range of velocities to carry on with the experiments. At this test section width the free-stream is studied without any test pieces inserted. We collect the video data and use the same technique of tracking defects to get an estimate of the velocity at a particular GPH value. Similarly the velocity profile is also found across the test section and is found to be nearly uniform as shown.

The main advantage of soap film tunnels is the quality of flow visualisation they provide. Some of the drawbacks can be related with the lack of consistency of flowrate, measure the fluid forces acting on the beam at an instant, and the soap film flow is generally complicated.

CHAPTER 3. CANTILEVER BEAMS IN SOAP FILM: METHODS AND PROCEDURES

This chapter introduces a series of experiments conducted in order to understand the fluid interaction with the cantilever beams. To implement this using the soap film tunnel, we initially tried a variety of orientations, but ended up with one particular orientation that enabled us to quantitatively analyze the physics of the flexible beam interacting with fluid flow. We will be discussing this particular setup in this section.

3.1 Introduction

Based on trial and error methods, we came to the conclusion that only the dynamic similarity can be achieved using the soap film experiment for our particular application. We try to maintain the dynamic similarity of the piezo-cantilevers in the wind tunnel with the soap film experiments to prove our hypothesis. The theory that abides the frequencies of vibrations and the frequency of vortex shedding is discussed. The schematic of the cantilever beam setup is shown in Fig. 3.1.

We consider the inclined cantilever beams with respect to the flow direction and vary the inclination as needed. Primarily, three angles of attacks plus a 90° case have been experimented and studied. The colors in the Table. 3.1, are allocated for the different flexural rigidities and follows the same code through out the thesis. The properties of these cantilevers are given in the table. M.I is Moment of Inertia.

Table 3.1: Properties of the soap film test models

Beam Type	Thickness	Width	Elastic Modulus	M.I (mm^4)	Color
Rigid	0.0762 mm	1 mm	1.38×10^9 Pa	0.46×10^{-5}	●
Semi-flexible	0.0508 mm	1 mm	1.38×10^9 Pa	1.092×10^{-5}	●
Flexible	0.0381 mm	1 mm	1.38×10^9 Pa	3.69×10^{-5}	●

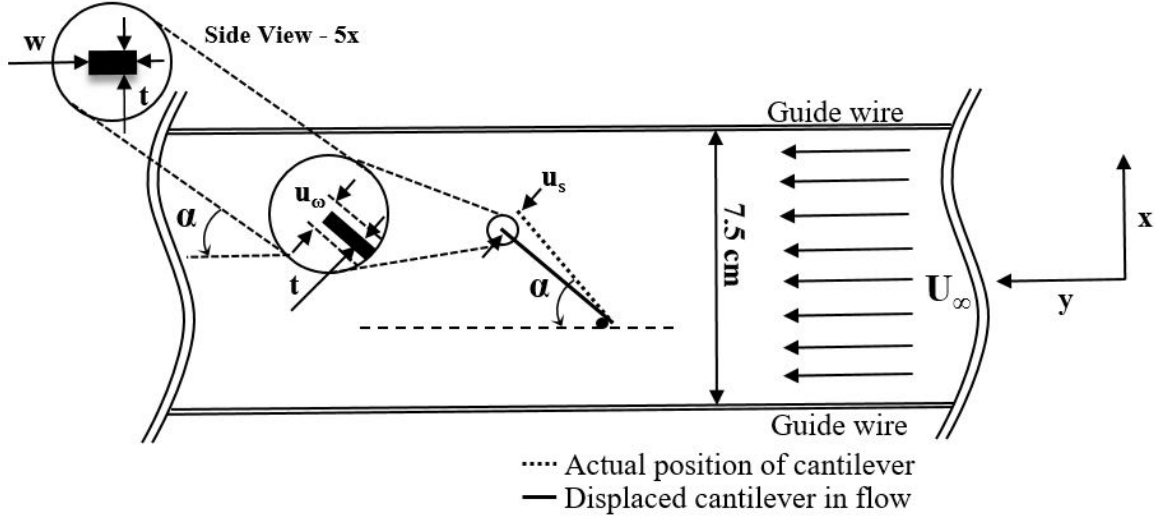


Figure 3.1: Schematic of the inclined cantilever beam

We have three cantilevers of different flexural rigidity used for the experiments. Each type that has been assigned a unique color code, is also used for plotting the results.

In the schematic setup shown in Fig. 3.1, we have the cantilever beam inclined at an angle " α " inside the soap film. The soap film test section width is maintained at a constant channel width of 7.5 cm for all the experiments. The beam displaces depending on the flexible characteristic of the beam and Reynolds number. This displacement is denoted by u_s . We also observe the beam to vibrate within the soap film and we denote this parameter by u_ω which is a measure of the amplitude of the oscillations. The width for all the test models is kept $< 1mm$ to avoid any out of plane flow interactions with the beams. The thickness of the beam varies and is tabulated in Table. 3.1.

Table 3.2: Comparison of test models used in the wind tunnel and the soap film experiments

System	Elastic Modulus (Pa)	Re	Aspect ratio (L/w)
Wind tunnel	3×10^9 Pa	0 – 30000	1.6, 3.6
Soap film tunnel	1.38×10^9 Pa	5000 – 35000	7.5, 10, 20

3.1.1 Single cantilever beam at an inclination

We consider the inclination of cantilever beams at several random angles of attacks with the flow direction since we did not prioritize the control of angle of attack as it was a tedious process to position the beam in space. From the smallest angle of attack = 12° to 90° , the experiments were conducted. The schematic orientation of the test piece is shown in Fig. 3.1. This orientation is apt for our study since we are also interested in analyzing the affect the angle of attack on the dynamics of these cantilever beams. This setup can be easily compared to that of the wind tunnel setup and predict the behavior of flow for different parameters. Four different lengths for cantilever beams of same material and elastic modulus but with varying thickness as shown in Fig. 3.2, e) are used as our test models for the soap film system. These models are do not have any geometrical similarity with that of the wind tunnel test models but we can observe the dynamic similarity being achieved. The thickness of the test models play a major role in terms of the flexible nature of the beam.

The cantilevers are pre-wetted before carefully placing in the test-section. We could not find an effective method to accurately place the cantilevers at the same angle of attack. Hence, we try to have the cantilevers placed at random angles of attacks but rather maintaining an order either increasing or decreasing with respect to the experimentation order, to have a sense of what sets of experiments were performed and recorded. This proved to be an effective yet reliable method to perform the experiments and collection of data.

The natural frequencies of the beams are illustrated in Fig. 3.3. The natural first harmonics can be extracted theoretically using the classical cantilever beam deflection problem. We use the proper boundary conditions to simulate our problem and end up getting the natural frequency to be eqn. 3.1. The plot is based on the simplified eqn. 3.2.

$$f_n = \frac{1.875^2}{2\pi l^2} \sqrt{\frac{EI}{m}} \quad (3.1)$$

Since, E , ρ are constants, we get the following

$$f_n \propto \frac{t}{l^2} \quad (3.2)$$

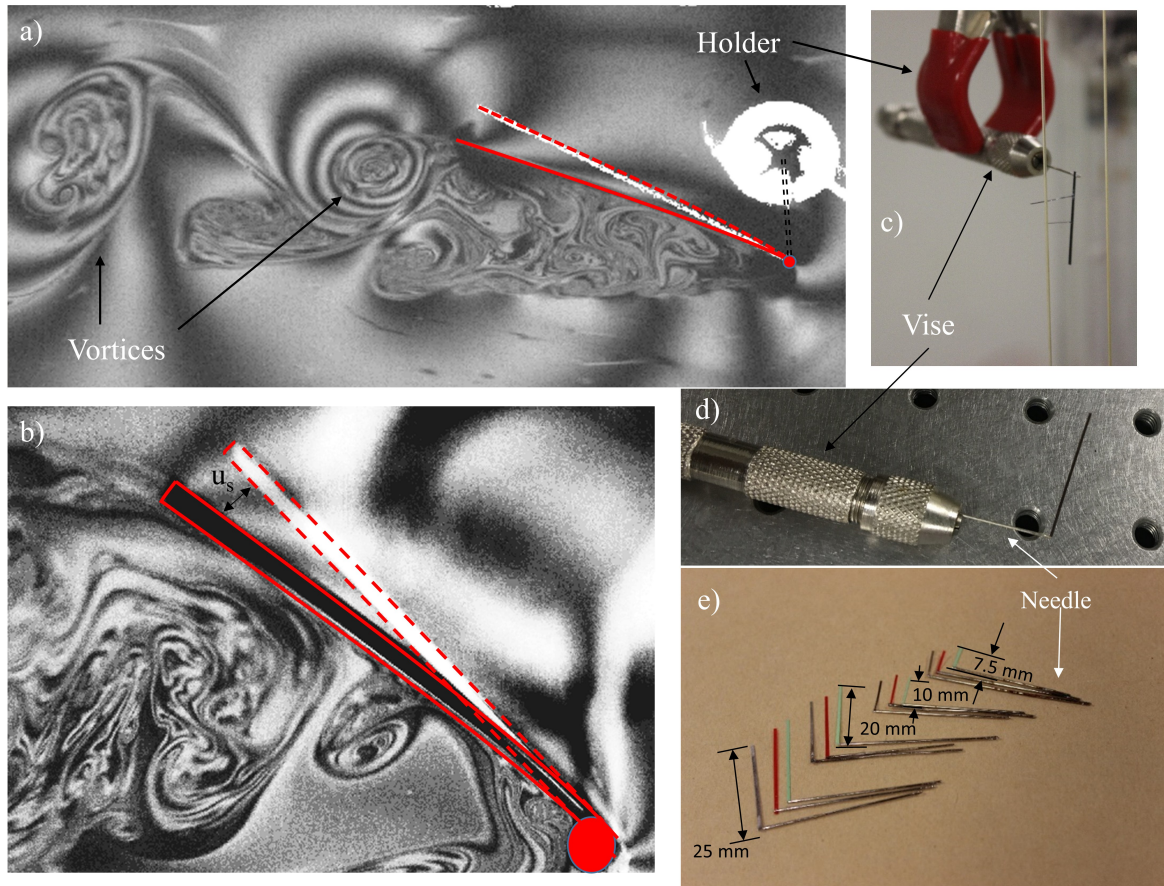


Figure 3.2: Schematic of the inclined cantilever beam

The beams are attached to a needle that is hold by a double-pin vise, which is held by another holder as shown in Fig. 3.2 c). In Fig. 3.2, a) is an actual image of an inclined cantilever beam embedded in soap film captured by the high-speed camera. The flow is directed from right to left. We could clearly visualize the 2D wake structure behind the beam. We can also see the vortices being shed from the trailing edge as well as the leading edge. Note the vorticity level of the vortex couple. The trailing edge vortex posses much higher vorticity than the leading edge vortex. Lam and Leung (2005) in a similar work as current, observed a similar behavior. He worked on experimental and computations on vortex shedding past an inclined flat plate. In b), a zoomed version of the beam is captured for a better resolution of the beam tip. These images are used for the beam tip tracking and proved to be promising from the results. In c) we can see the actual mounting of test piece and the holder, alongside the guide wires.

The below table shows all different angle of attacks used for the three types of beams and lengths.

Table 3.3: Angles of attack for $L = 7.5$ mm

Cantilever Type	α_1	α_2	α_3	α_4
Rigid	27°	34°	48°	90°
Semi-flexible	21°	27°	36°	90°
Flexible	18°	30°	42°	90°

Table 3.4: Angles of attack for $L = 10$ mm

Cantilever Type	α_1	α_2	α_3
Rigid	16°	26°	40°
Semi-flexible	19°	28°	40°
Flexible	20°	31°	47°

Table 3.5: Angles of attack for $L = 20$ mm

Cantilever Type	α_1	α_2	α_3	α_4	α_5
Rigid	17°	20°	23°	41°	90°
Semi-flexible	14°	20°	30°	38°	90°
Flexible	12°	18°	28°	49°	90°

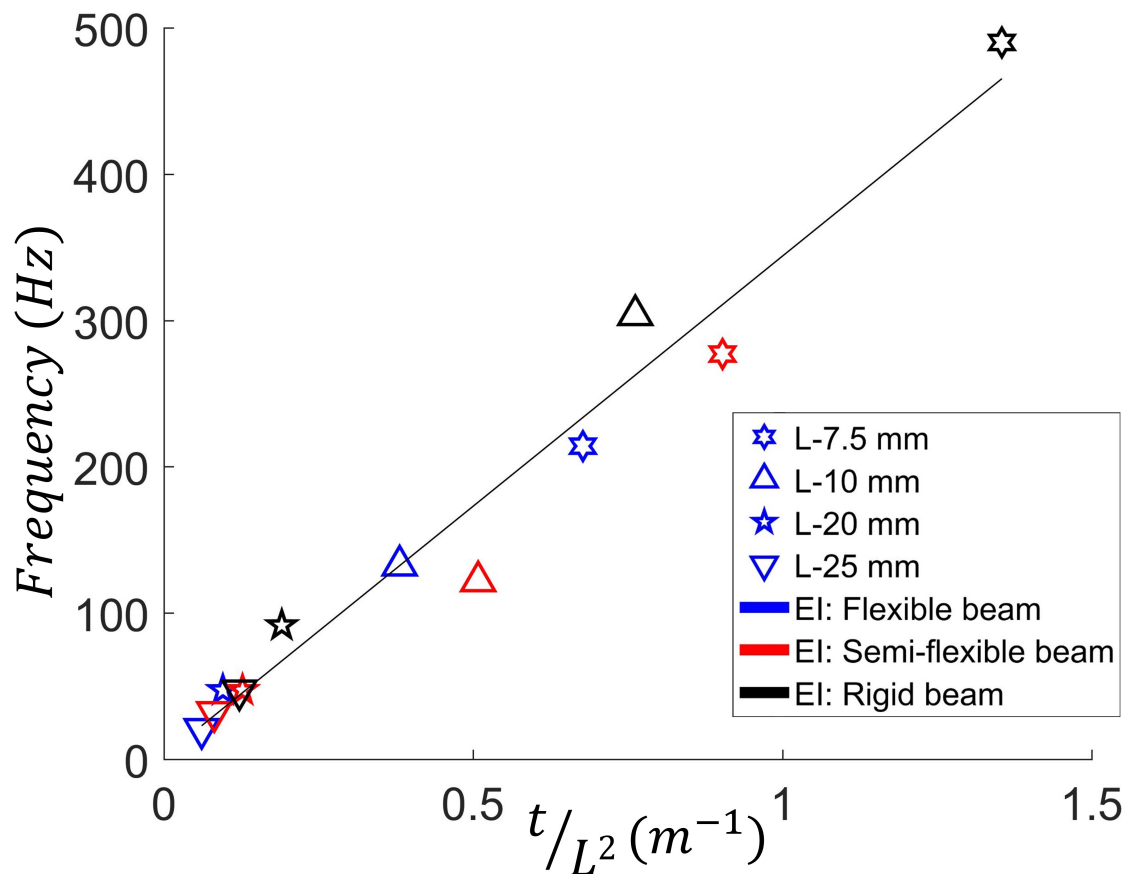


Figure 3.3: First natural (eigen) frequencies calculated in air for beams of lengths $L = 7.5$ mm, $L = 10$ mm, $L = 20$ mm and $L = 25$ mm. Note the good agreement with our assumptions of natural frequencies.

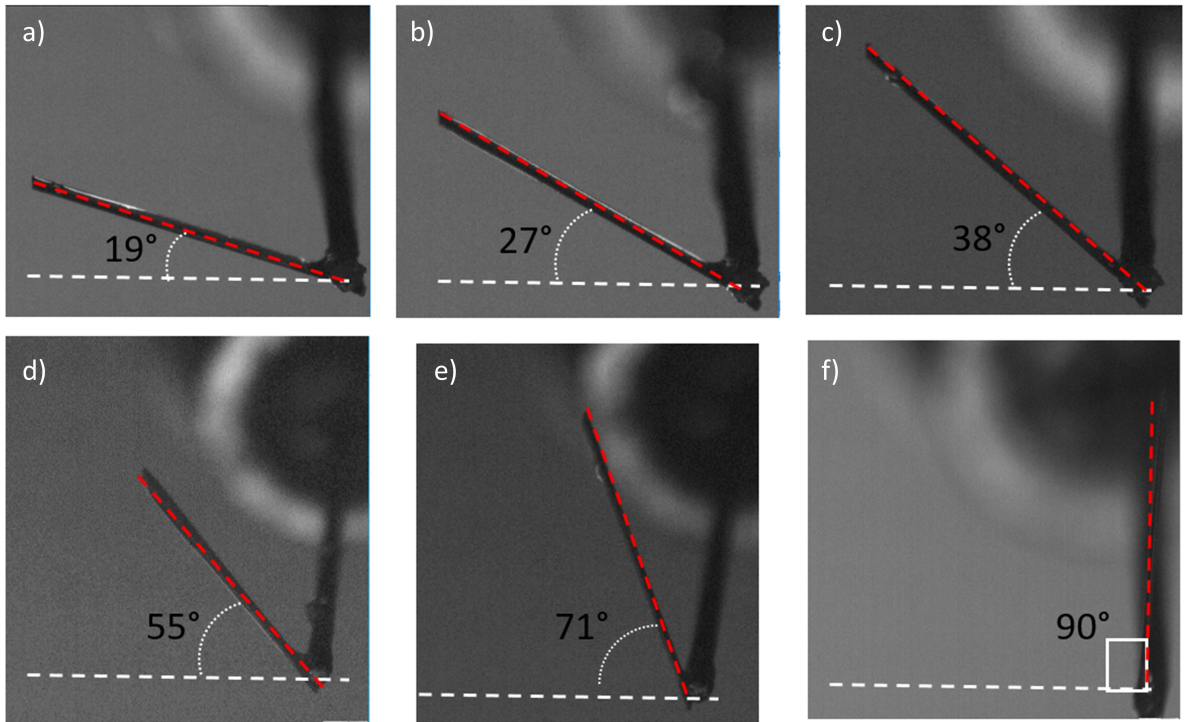


Figure 3.4: Cantilever beam with the change in inclination. a), b), c) are the current models analyzed and interpreted for results. Results for d), e), f) can be found in the Appedix. 1 as a part of additional materials

3.1.2 Beam characteristics in soap film

Jia et al. (2015) investigated a flag in flow with an externally forced vibration by using flexible filaments and soap film. His experiments have shown that for a filament in either oscillatory state or stationary state, the external force vibration lead to its oscillations. A small perturbation lead to a large response in amplitude of flapping. We observe a similar scenario when an external force was applied to the flexible beams. Fig. 3.5, depicts the motion of the flexible inclined cantilever beam whilst in the soap film, indicating the displacement and vibration of the beam. Images a), b), c) are actual images from an experiment. The blue shaded contour over in the images is the contour of the beam in motion. The background image is just a stable not moving image at its equilibrium position. The red line indicates the moving beam tip, whereas the black line indicates the mean beam tip displacement. This figure helps us clearly visualize the motion of the beam with respect to its equilibrium position.

3.1.2.1 Displacement and vibrations of the beam in soap film

The displacement of the cantilever beam as shown in Fig. 3.1, is denoted by u_s . This is calculated by taking the average of the vibrational displacements when we plot it as a waveform. The mean beam tip displacement is nothing but u_s . This will be discussed in more detail in Chapter. 5.

The vibrations of the beam are denoted by u_ω . This is nothing but the amplitude strength of the cantilevers vibrating in the soap film. This will be discussed in more detail in Chapter. 5.

3.1.3 Vortex shedding behind the cantilever beam

A vortex street pattern comprises a train of leading edge vortices alternating with a train of trailing edge vortices. The trailing edge vortex is directly shed from the sharp trailing edge while the formation and shedding of the leading edge vortex involves a much more complex mechanism. The leading edge vortex seems to be shed into the wake from an axial location near the trailing edge. After shedding, the vortices are continually convected downstream in the wake with a shedding speed that was found to be dependent on the free-stream velocity.

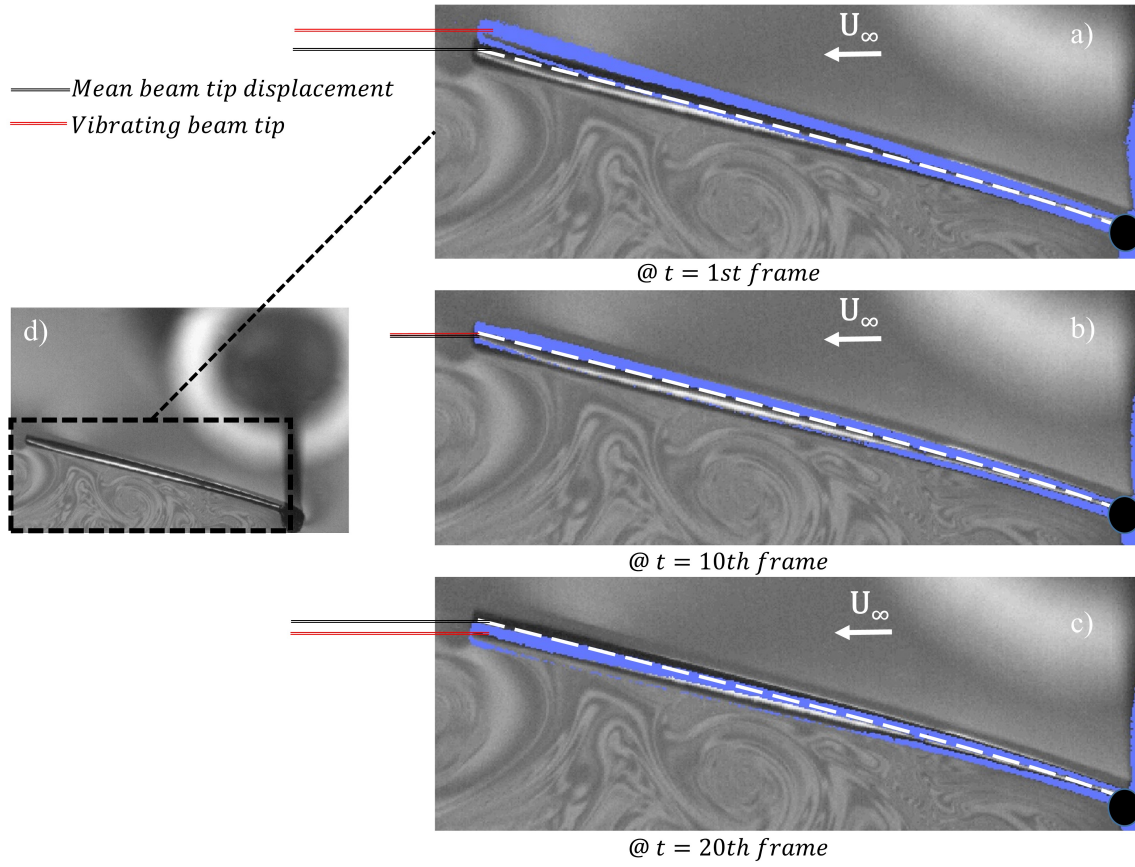


Figure 3.5: Vibrating flexible beam of length $L = 10$ mm at an $\alpha_2 = 31^\circ$ at 0.3 GPH in soap film. Although the vibrations are very small, we could see the vortex shedding locked in with the trailing edge of the beam.

The trailing edge vortex, as compared to the leading edge vortex, is found to possess a higher peak vorticity level at its centre on reaching the same axial location. It induce more intense fluid circulation. It is found that the results at the three angles of attack can be collapsed into similar trends by using the projected plate width as the characteristic length of the flow. Fig. 3.5 shows an image of beam vibrating in a flowing soap film. The length of the beam is 7.5 mm, and the flow rate is 0.3 GPH. The flow direction is from right to left and time iterates from right to left following a sequence going down. Fig. 3.5.a) is a photo taken from an experiment. The figure shows the beam and wake structure after processing the photo. The beam vibrates and vortices are shed from its trailing edge and form a vortex street in its wake. We could see similarities between the structure of vortices behind a cylinder and the inclined cantilever beam. The Karman vortex street of a cylinder is formed by two rows of vortices with counter rotation shedding alternatively from two sides of a cylinder as seen in Fig. 2.19.

For the vortex structure in the wake, Zhang et al. (2000) elaborated it could be a result of Kelvin-Helmholtz instability. Because the flow velocity by two sides of the beam is different, the flow loses its stability due to shear. He used a filament as their test model. Argentina and Mahadevan (2005) proposed a different explanation about the wake structure. They suggested the structure is caused by the coupling behavior of fluid with the beam vibrations.

Jia et al. (2015) found that a lock-in regime in the middle of two non-lock-in regimes. In the non-lock-in state, the dominant frequency component in the wake of the cylinder is found to be equal to the wake shedding frequency without any sort of forcing. Similar results have been observed with the flexible filament experiments, where the lock-in regime was found between two non-lock-in regimes. Hirata et al. (2008) had performed a similar study using a circular cylinder and observed this phenomena both numerically and experimentally. We had observed this phenomena in our experiments for the flexible beam case. We also find that the free vibration frequency dominating when the external forced vibration frequency nothing comparable to filaments free flapping frequency which was also observed by him. Their study also shows their setup's effectiveness in an active vibration control to enhance the flapping of a filament. Although we do not use any external forcing, this helped us in understanding the behaviour of the fluid interaction with the beams.

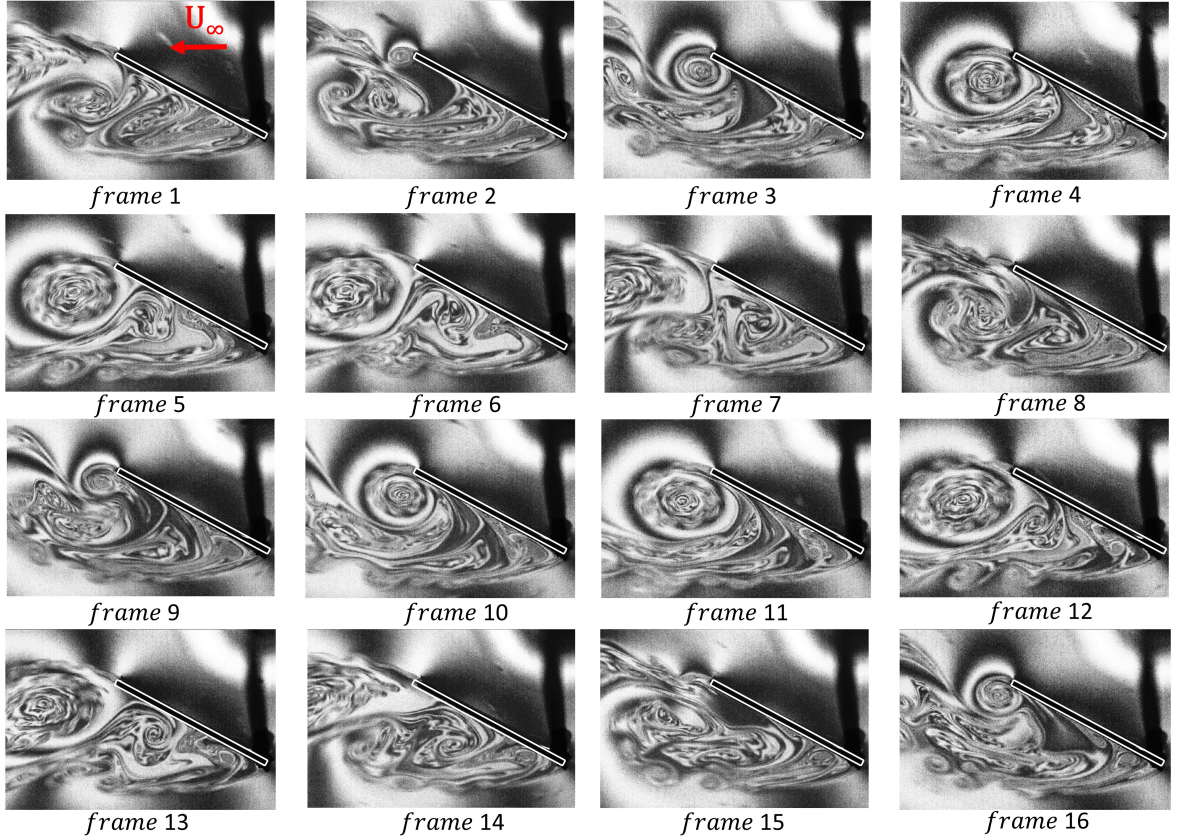


Figure 3.6: Vortex shedding for flexible beam of length $L = 7.5$ mm at an $\alpha_2 = 30^\circ$ at 0.3 GPH. We could clearly see the vortex shedding lock-in behavior as discussed by other authors in the literature.

CHAPTER 4. IMAGE PROCESSING

We will begin discussing the processing and post-processing techniques and features applied for the visual data we acquire from the soap film experiments. These images are captured with a high-speed camera at 5000 *fps* allowing us to visualize the flow in high-resolution. We utilize two lenses depending on the image size, resolution and user application. One lens is utilized in order to capture images for the downstream vortex shedding as well as the tip of the cantilever beam. The size of the capturing window for the first lens is approximately $40 \times 60 \text{ mm}^2$ whereas for the second lens it is $8 \times 12 \text{ mm}^2$. This lens is used for a higher resolution of the beam tip for minimizing the unnecessary noise acquired through the tracking algorithm. The two lenses used are Nikkor 105 *mm* micro-lens and Nikon Tamron SPAF 180 *mm* *f*/3.5 Di respectively. The techniques described below are developed for the calculation of the velocity of the soap film flow, beam tip tracking and tracking of vortices in the wake, for further analysis of the quantitative data. The in-house algorithms are developed using MATLAB as the base platform.

The fast camera captures the images as an RGB type image. These images have three color maps namely red, green, and blue images clubbed to form a final real image as shown in Fig. 4.1. These images are then saved as a movie for easy access to the data. The video data read by Matlab will be in a 4-D Matrix format. An image maybe considered as a two-dimensional matrix where the rows and columns correspond to the spatial position of the pixels in the image. The respective matrix values are the intensity values of the pixels. The first two dimensions in the 4-D Matrix also represent the height and width of the capturing window in pixels respectively i.e. 436px608p. This window size is dependent on the number of frames the camera is able to capture, which is again user-selected. But this does not affect the data since we consider only one frame rate i.e. 5000 *fps*, that eliminates the hassle of repetition of experiments. Also, there is a scaling ratio we consider to analyze the data, that depends with

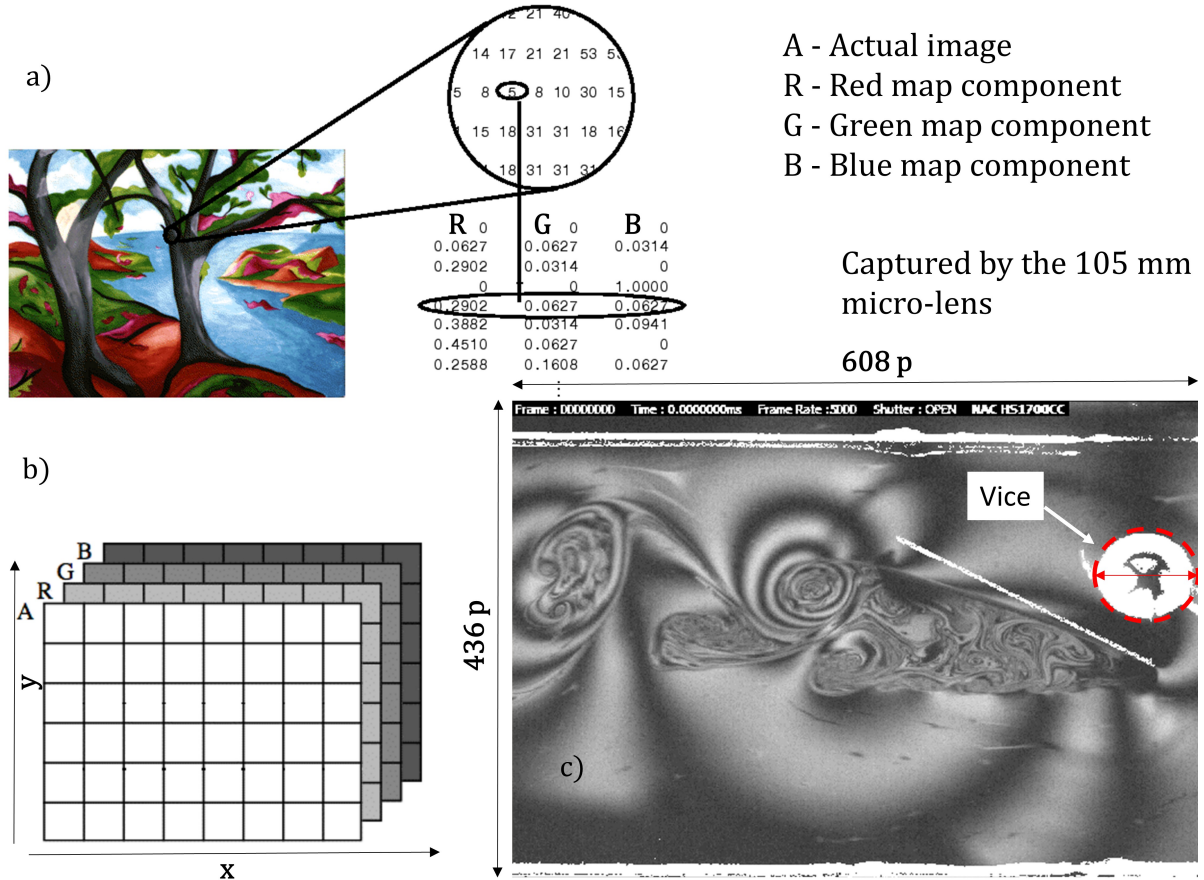


Figure 4.1: RGB image type. a) Depicts the computer vision for an RGB image type (Source: Mathworks). b) The 3-D matrix format of an RGB image. c) An experiment image viewed through the high-speed camera interface with the window sizes

the type of lens used. Usually we calculate the scaling ratio making use of a known length value of a object from the visuals. Although the length of beam itself can be utilized in doing so, we find radii of the front face of the vice that holds the cantilever beams as shown in Fig. 4.1. After comparing the pixel length of the vice face obtained from the visuals and the actual diameter of the vice face one can easily determine the scaling ratio. The third dimension is for the number of color maps the image contains. There are typically three color maps red, green, blue in any color image. And lastly, the number of frames is given by the fourth dimension of the 4-D matrix.

4.1 Velocity measurement

As discussed in Chapter. 2, the velocity of the soap film is an important parameter that allows for a quantitative comparison of the results with that of the wind tunnel experimental results. Considering the assumption that the defects we observe inside the soap film travel with the same rate as the free-stream flow rate, we will detect these defects/pollutants using an in-house algorithm.

Fig. 4.2 shows the trajectory of a defect over time. In the plot, the horizontal direction is the flow direction, and the vertical direction is time advancing direction. Figure a) and b) are actual and processed images of freestream flow. And the corresponding time advancing images are shown. The algorithm processes the flow image (Fig. 4.2(i)) in order to segment the defects that we see in the actual image (check Fig. 4.2(ii)). Once the defect is detected the code automatically creates a colored-dashed line perpendicular to the flow direction as seen in (ii). And with the time advancing, these defects are tracked for their path. The length of the path is determined by the capturing window size. Using the scaling ratio (conversion of pixel length to mm), the actual velocity of the defect can be obtained. This process continues until all the 5000 frames are processed. These velocities are saved in an array and averaged at the end to obtain a mean velocity of the freestream. By combining a series of slices from a time-sequenced high speed camera recorded images, the defects are tracked over time. The tracked path of one of the defects is plotted against time as shown in Fig. 4.2, c). We achieve a reasonable value for the velocity of the soap film when compared with the flowrate values.

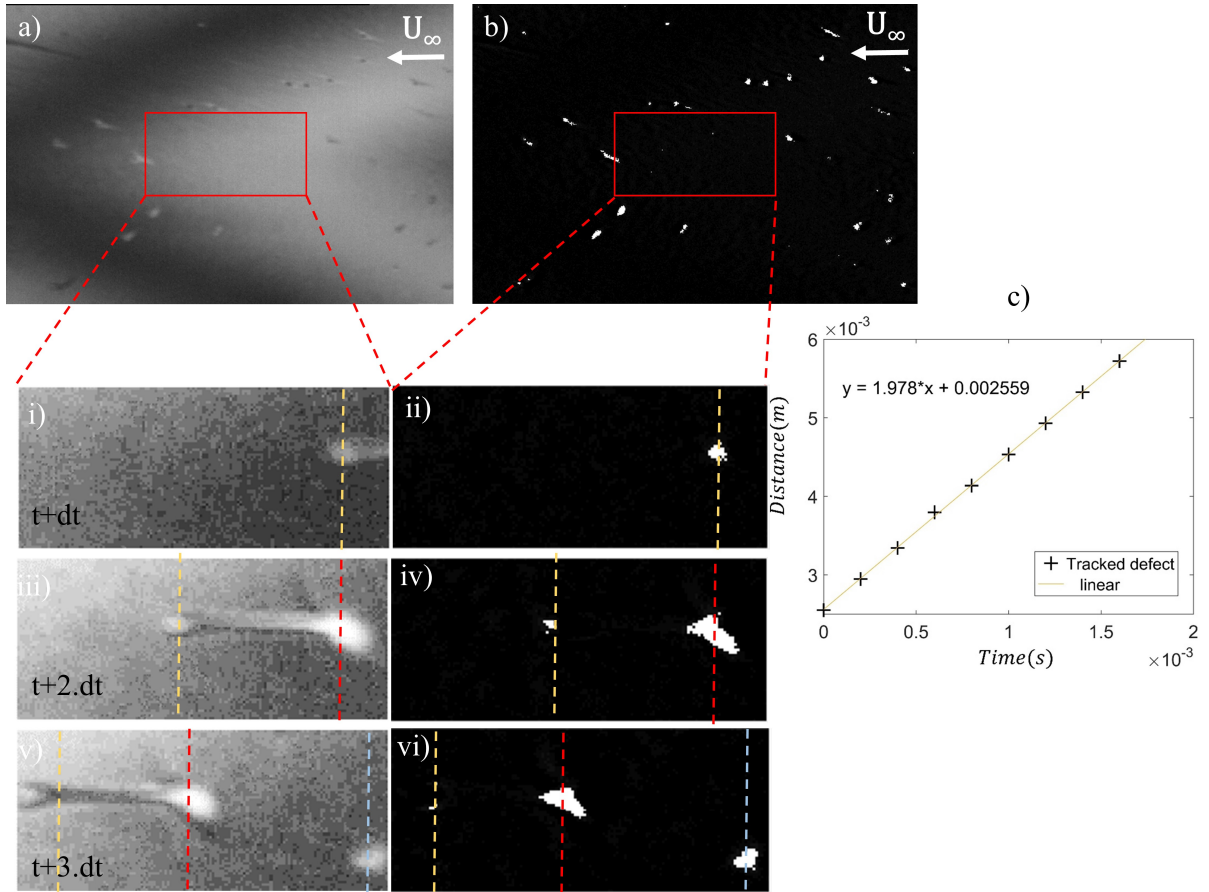


Figure 4.2: Tracking the defects in the soap film. The algorithm automatically tracks all the defects or pollutants in the soap film and the average flow-rate of the freestream is estimated. b) is the filtered and processed image of a). Time is incrementing from top to bottom.

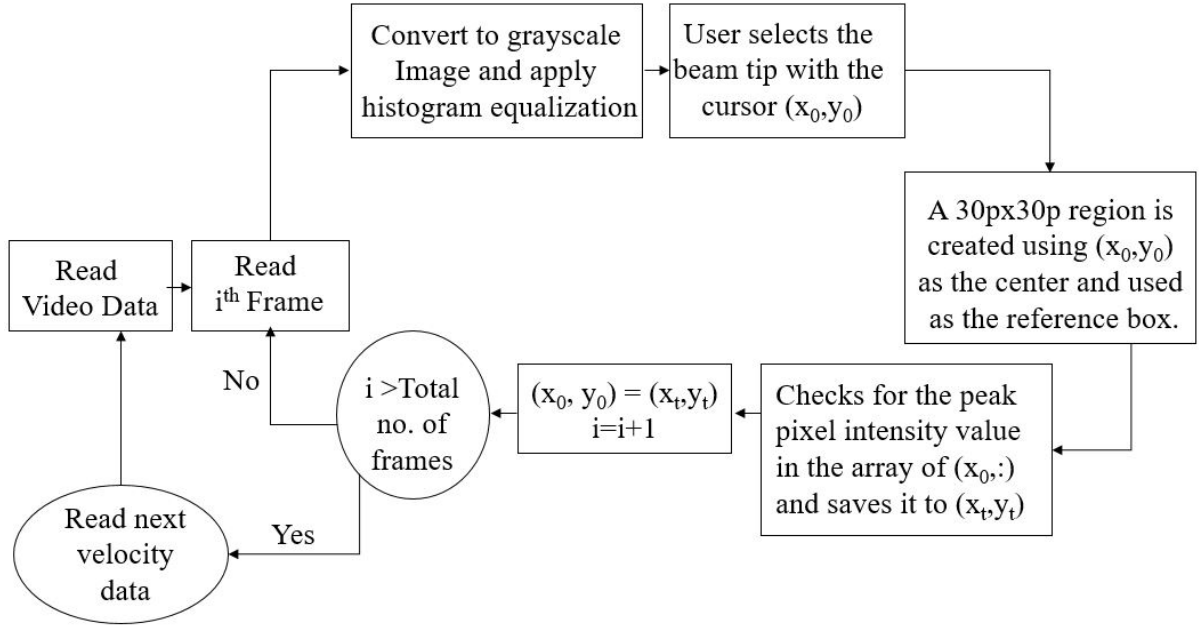


Figure 4.3: Flowchart for Image digitalization

4.2 Tracking beam vibrations

The images acquired from the high speed camera are processed through a specific set of filters and a threshold is then applied as illustrated in Fig. 4.4. The video data is read by Matlab one frame at a time. The algorithm used is shown as a flowchart in Fig. 4.3. This code converts the image into a gray-scale image and then based on the histogram plot of the image, we then calculate the average or the mean threshold value. Using this threshold value the histogram plot is normalized. This normalization is important since we observe the sodium lamp flicker at a particular frequency, which changes the intensity values of each frame and hence making the tracking an impossible task. This threshold value is then used to differentiate the interference patterns in the soap films. Later, the user will be prompted to click on the tip of the beam. The code uses this user-selected coordinate as a starting point to track the beam tip. The initial coordinate is indicated by the red blob in Fig. 4.4. A $30\text{px} \times 30\text{px}$ green dashed outline is created having this coordinate as the center. The code then checks for the peak intensity value in the array that includes all y values corresponding to the fixed x coordinate.

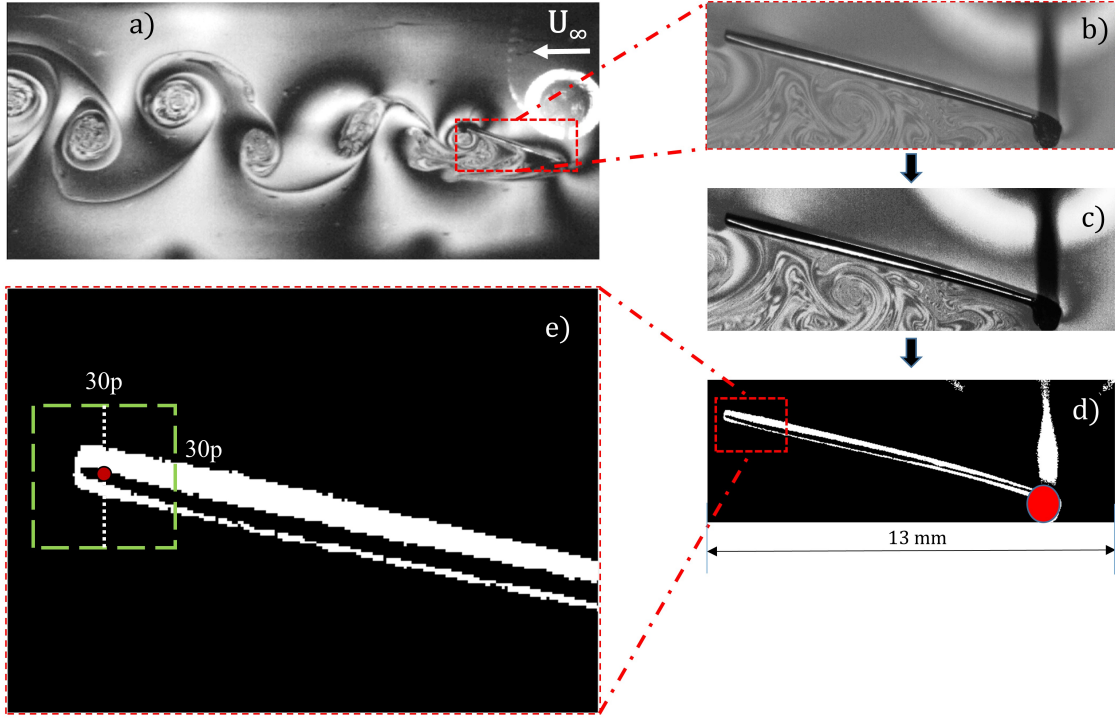


Figure 4.4: Tracking the tip of the beam. The image processing is displayed in a step-by-step manner. e) is the final processed image ready to be analyzed.

It then saves this set of coordinate in a new array. For the next frame, the previous tracked coordinate will be considered as the new center of the box region and the process continues until all the frames of the Video data are read. With the aid of threshold control we segment the beam and track its center-line to attain the vibration of the beam with time.

The coordinates of the tracked beam tip through the 5000 frames is saved as an array that would be later used to calculate the displacement, vibrational amplitude, steady loading on the beam, vibrating frequency of the beam etc. Fig. 4.5, shows the wave form of the y-coordinate of the tracked beam tip. By looking at the waveform, one could be convinced with our algorithm to track the tip. In Fig. 4.5, a) and b) are actual and processed images. c) illustrates the normalized beam tip vibration. The average of the tip displacement is what we

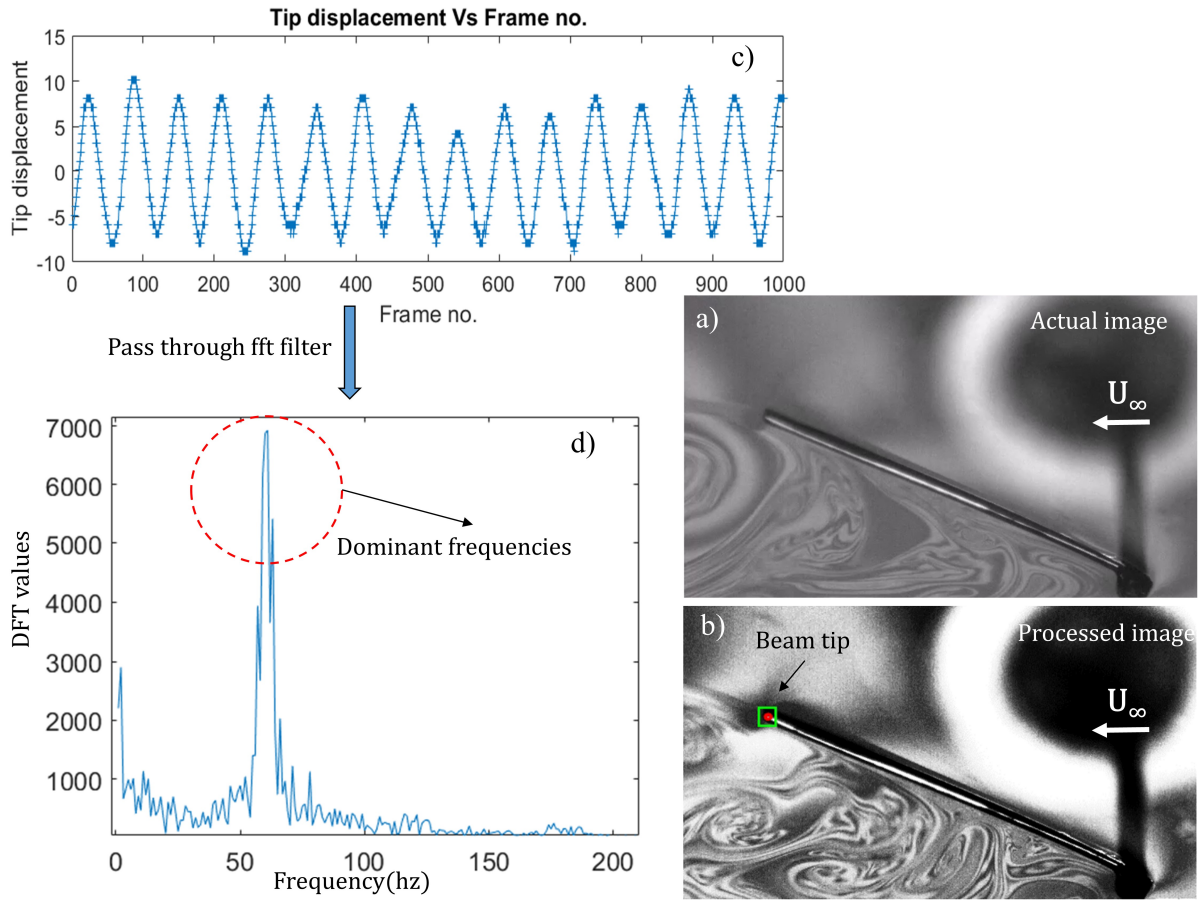


Figure 4.5: c) Waveform of the tracked tip of the beam. These waveforms are then processed through an FFT filter to extract the frequencies as shown in d)

call the steady displacement. For obtaining the frequency of vibrations we use a fast-fourier transform, that easily converts the time domain plot to a frequency domain plot as shown in d). We then sort all the dominant frequencies indicated by the circle with the aid of a cut-off frequency determined as the 60% of the maximum DFT amplitude in the frequency domain plot. One should be careful to not naively assume that these sorted frequencies are the actual beam vibration frequencies. Since there is always a possibility of high-frequency dominant noise get pass through the filters used in the image processing. By careful review of the sorted frequencies, we end up eliminating quite a few recurring frequencies for a range of Reynolds numbers. This is implemented purely based on observations. We could observe the sodium light flickering frequency and its higher harmonics appearing in the dominant frequencies. Once they are eliminated we have a filter range from $40\text{Hz} - 250\text{Hz}$ used for the remaining frequency set. The frequencies in these range are then averaged for each velocity data. These frequencies are the ones we will discuss in the results section.

4.3 Tracking vortices in the wake

Based on observations and the nature of the vortices generated in our soap film visuals, we utilize the geometry of these structures to track them. We treat the vortices as an oval/circular shaped geometry and utilize a similar algorithm, used for tracking the tip of the beam, for tracking these geometries. The geometry of these vortices can be illustrated as oval structures of varying radii as seen in the Fig. 4.6. We utilize this fact and track the curvatures in the image in order to locate the position of the vortex.

Hidema et al. (2010) proposed an interference image analysis as a new method for the study of turbulence in 2D flowing soap films with polymer additives. They propose a similar curvature analysis method that locates the curvatures of the interference pattern of turbulent soap films and later use it to predict the thickness of the film. The algorithm utilized is nearly similar to the once explained in Fig. 4.3. In Fig. 4.6, d) is the actual image we obtain from the soap film experiments. We can clearly see the von-karman vortex street downstream of cantilever beam. The user selects the core of a vortex to be tracked. This coordinate is used as the center of a 30px30p region shown in a red box. The size of the box is again an input by the user, so

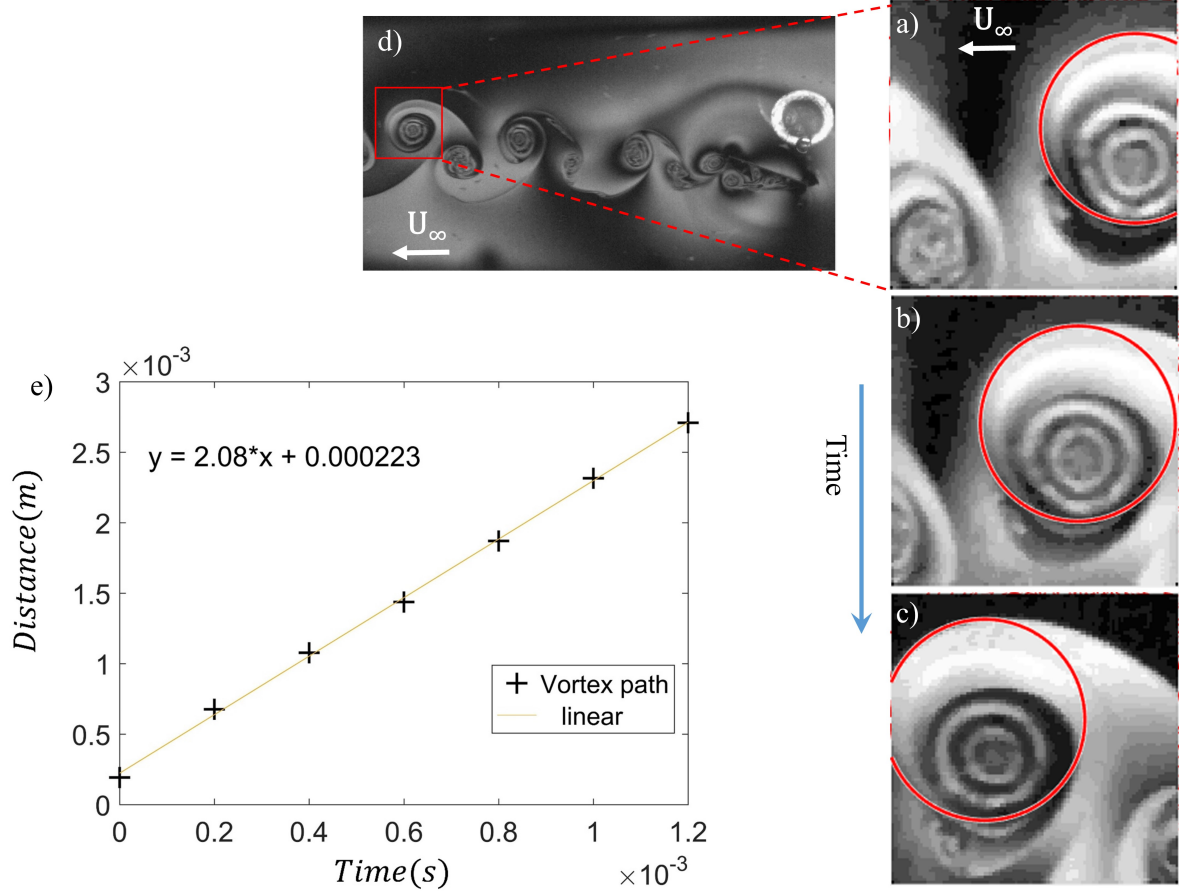


Figure 4.6: Tracking the vortices shed behind a rigid beam having an angle of attack $\alpha = 27^\circ$.

there should be a pre-assessment necessary for these values. Once the region is created, it is then segmented out in another window. As the time advances, the vortices shed as seen in the series of images a), b), c). The code now just looks for a curvature of pre-determined radii. This curvature or circle, in our case, follows the path of advected vortex downstream. This is continued until the code runs out of available frames. e) is a plot showing the rate at which a single vortex has been convected. This allows us to have an idea of the rate at which the vortices are being shed, the frequency of vortices being shed, the rate of growth of the vortices etc. Once these curvatures are tracked, they are used to obtain the path of the vortex and in turn we find the rate at which they are shed.

CHAPTER 5. RESULTS AND DISCUSSION

We will first study the results of the steady aerodynamic loading on the inclined beam by varying our control variables and discuss their dependency. We will also compare the soap film system results with the wind tunnel system results. Secondly, we have the vibrations of the beam plotted against the corresponding vortex shedding for different data sets aiming our control variables. Later, the Strouhal numbers and Reynolds numbers are promptly discussed. Before discussing the results, we introduce a small plotting nomenclature to clearly define each of the control variable we considered in our experiments.

5.1 Introduction

The nomenclature is as follows: Squares – lowest angle of attack, Circles – intermediate angle of attack, Triangles – Highest angle of attack and so on. The color denotes the relative rigidity type: Blue Flexible beam ($t = 0.0381 \text{ mm}$), Red Semi-Flexible beam ($t = 0.0508 \text{ mm}$), Black Rigid beam ($t = 0.0762 \text{ mm}$). Since we only analyzed the data for the two shortest beams, they are represented by Solid for $L_1 = 7.5 \text{ mm}$, Hollow for $L_2 = 10 \text{ mm}$. The plotting nomenclature is also shown in Fig. 5.1. We worked on several more experiments, the data either fails or needs improvements in resolution or were really tedious and difficult to analyze and hence are not presented in this thesis.

The aerodynamic loading on the inclined cantilevers are studied with respect to the increasing dynamic loading. We also discuss the relation between the beams vibrations and the corresponding vortex shedding for an inclined cantilever beam with various variables such as the beams flexural rigidity, length, angle of attack and look for the dependency.










Rigid	Semi-flexible	Flexible
		
$\alpha_1 < \alpha_2 < \alpha_3$	L_1	L_2
α_1		
α_2		
α_3		

Figure 5.1: Plotting nomenclature for a better understanding of the plots.

5.1.1 Steady displacement loading vs dynamic loading

In the tables below, the values of the steady aerodynamic coefficients for the three beams and for two lengths $L_1 = 7.5 \text{ mm}$, $L_2 = 10 \text{ mm}$ with an increase in angle of attack as an added variable are shown. We can observe an increase in these coefficients when we increase the angle of attack and length of the beam. α_1 being the least and α_3 as the highest angle of attack in our experiments. The error bars in the plots are the vibration amplitudes.

Table 5.1: For flexible beam: Aerodynamic coefficients with respect to increase in angle of attack

C_{SAL}	α_1	α_2	α_3
$L_1 = 7.5mm$	1.042	1.119	1.309
$L_2 = 10mm$	1.09	1.487	2.076

Table 5.2: For semi-flexible beam: Aerodynamic coefficients with respect to increase in angle of attack

C_{SAL}	α_1	α_2	α_3
$L_1 = 7.5mm$	0.248	0.352	0.416
$L_2 = 10mm$	0.66	0.945	1.123

For the rigid beam case, the amplitude of vibrations and aerodynamic loading are found to be relatively small compared to the other beams. For length $L_1 = 7.5 \text{ mm}$ there were very small (either not visible in our experiments or were not detected by the house-built programs) or negligible amplitude vibrations and aerodynamic loading observed.

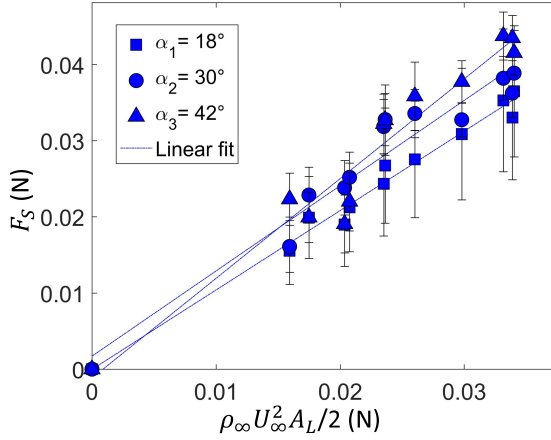


Figure 5.3 Steady tip displacement force of a flexible vibrating cantilever beam of Length ($L_1 = 7.5 \text{ mm}$) versus dynamic force with varying angle of attacks.

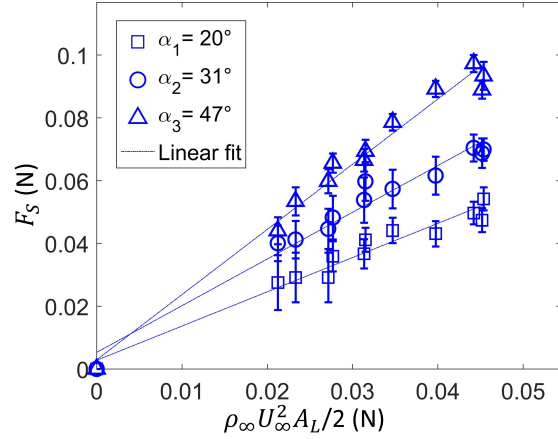


Figure 5.4 Steady tip displacement force of a flexible vibrating cantilever beam of Length ($L_2 = 10 \text{ mm}$) versus dynamic force with varying angle of attacks.

Figure 5.5: The dotted lines are linear fits having slopes dependent on the angle of attack. This slope is identified as an aerodynamic loading coefficient C_{SAL} . Note that C_{SAL} increases with the increase in angle of attack .

Table 5.3: For rigid beam: Aerodynamic coefficients with respect to increase in angle of attack

C_{SAL}	α_1	α_2	α_3
$L_1 = 7.5 \text{ mm}$	-	-	-
$L_2 = 10 \text{ mm}$	0.285	0.331	0.393

5.1.2 Strouhal number vs Reynolds number

The Strouhal number (St) is a dimensionless number that describes oscillating flow mechanisms. It is named after Vincenc Strouhal, a Czech physicist in 1878 experimented with wires experiencing vortex shedding and singing in the wind. The Strouhal number is an integral part of the fundamentals of fluid mechanics.

The Strouhal number is defined as;

$$St = fL/U \quad (5.1)$$

where f is the frequency of vortex shedding, L is the characteristic length (such as hydraulic diameter, or the airfoil thickness) and U is the freestream velocity. The characteristic length

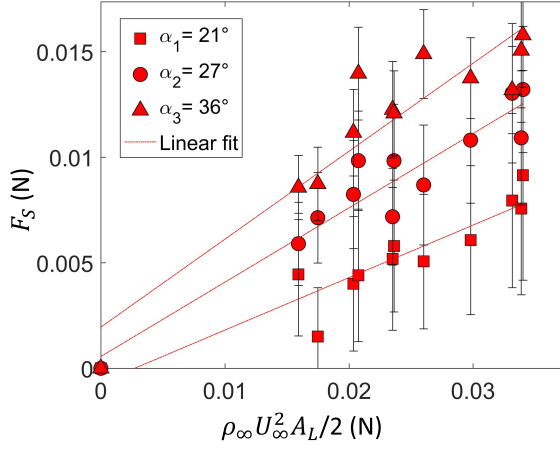


Figure 5.7 Steady tip displacement force of a semi-flexible vibrating cantilever beam of Length ($L_1 = 7.5$ mm) versus dynamic force with varying angle of attacks.

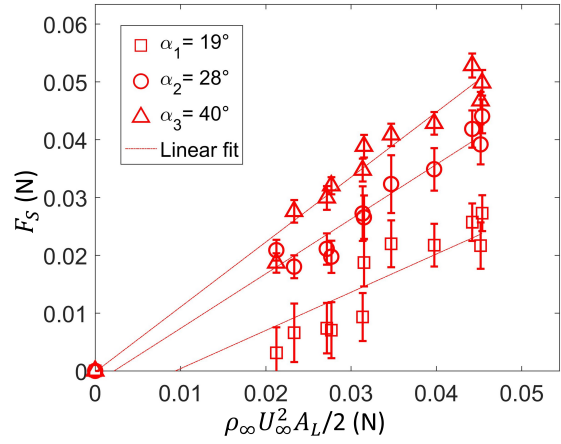


Figure 5.8 Steady tip displacement force of a semi-flexible vibrating cantilever beam of Length ($L_2 = 10$ mm) versus dynamic force with varying angle of attacks.

Figure 5.9: The dotted lines are linear fits having slopes dependent on the angle of attack. These slopes are identified as an aerodynamic loading coefficient C_{SAL} . Note that C_{SAL} increases with the increase in angle of attack .

in certain cases like heaving (plunging) flight is the amplitude of oscillation.

For large Strouhal numbers of order 1, fluid flow is dominated by viscosity, resulting in a collective oscillating movement of the fluid. For low Strouhal numbers of order 104 and below, the oscillations are dominated by the high-speed, quasi steady state portion of the movement. Oscillation at intermediate Strouhal numbers is characterized by the buildup and rapidly subsequent shedding of vortices.

The Reynolds number (Re) is another important dimensionless parameter in fluid mechanics that helps predict flow patterns in different fluid flow situations. It has wide applications, ranging from liquid flow in a pipe to the passage of air over an aircraft wing. The Reynolds number is used to predict the transition from laminar to turbulent flow, and used in the scaling of similar but different-sized flow situations, such as between an aircraft model in a wind tunnel and the full size version. The predictions of onset of turbulence and the ability to calculate scaling effects can be used to help predict fluid behaviour on a larger scale, such as in local or global air or water movement and thereby the associated meteorological and climatological

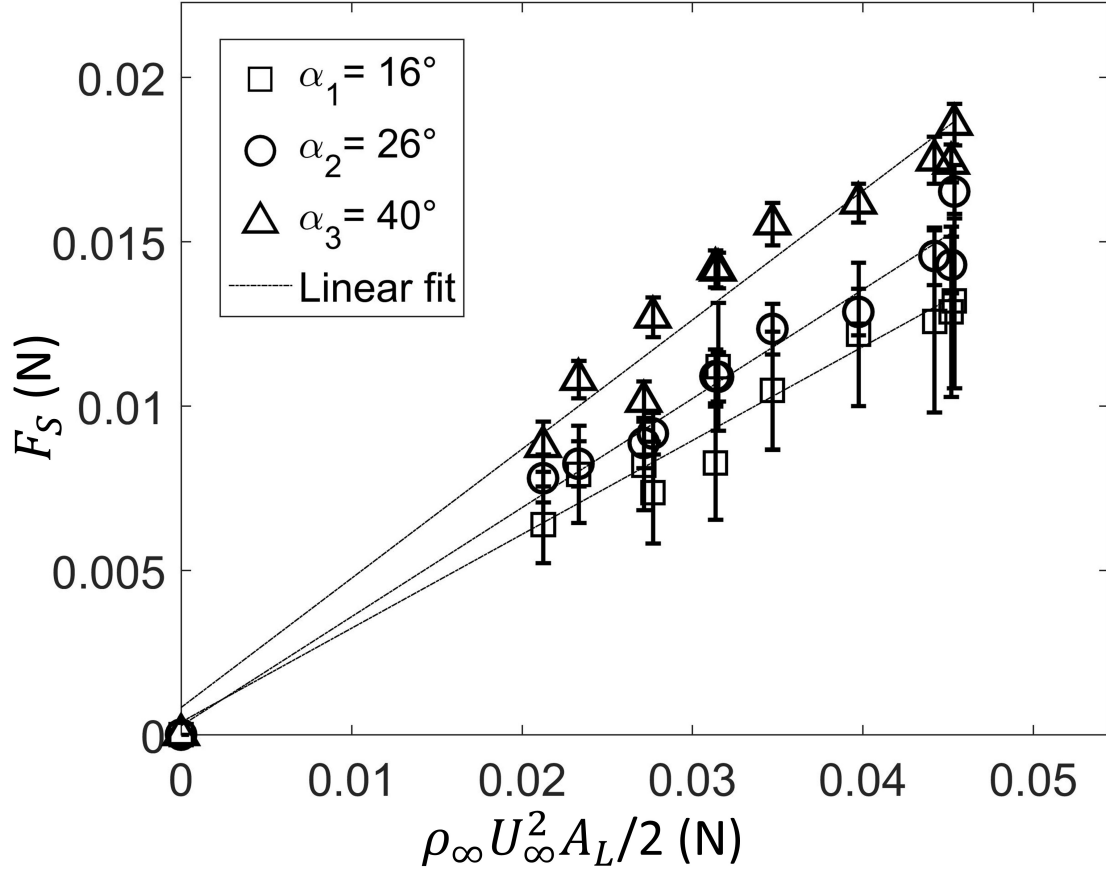


Figure 5.10: Steady tip displacement force of a relatively rigid vibrating cantilever beam of Length ($L_2 = 10 \text{ mm}$) versus dynamic force with varying angle of attacks. The dotted lines are linear fits having slopes dependent on the angle of attack. This slope is identified as an aerodynamic loading coefficient C_{SAL} . Note that C_{SAL} increases with the increase in angle of attack .

effects.

The Reynolds number is defined as

$$Re = \rho \cdot u \cdot L / \mu \quad (5.2)$$

where: ρ is the density of the fluid (SI units: kg/m^3), u is the velocity of the fluid with respect to the object (m/s), L is a characteristic linear dimension (m), μ is the dynamic viscosity of the fluid (Pas or Ns/m^2 or kg/ms).

5.1.3 Strouhal vs angle of attack

Fig. 5.20 shows the effect of angle of attack on the Strouhal numbers for the data analyzed. Similar results were found by Chen and Fang (1996), in his experimental studies of the vortex shedding over inclined flat plates. The author observed that at low angles of attack $\alpha = 0^\circ - 5^\circ$, the influence of Reynolds number become significant due to the flow reattachment. But for higher angles of attack $\alpha = 0^\circ - 5^\circ$, a fully separated flow is observed and Reynolds number does not have any effects on the relation between the Strouhal number and the angle of attack.

5.1.4 Beam vibrations vs vortex shedding

Figure. 5.21 shows a linear relationship between the beams vibrations and the corresponding vortex shedding. A line $y = x$ is plotted to show the dependency. It can be clearly seen that the cluster of experimental data fits and aligns very well on this line. The flexible beam of length $L_1 = 7.5 \text{ mm}$ at angle of attack $\alpha_1 = 18^\circ$ seems to have the highest vibrating and vortex shedding frequency. It can also be seen that with the increase in angle of attack, both the parameters decrease. Note that from the St Vs Re graph the vortex shedding is known to increase with the increase in Re .

In Fig. 5.22 we can observe that the rigid beam vibrates at a very high frequency but with a low amplitude. On the contrary the flexible beam of the same length vibrates at a lower frequency but has a high amplitude. But when the length is decreased, we could observe an increase in the frequency of vibrations but little change in amplitude for the flexible beam case. The angle of attack dependency can also be depicted. We see that with increase in angle of attack we observe a decent amount of decrease in both the frequency of vibrations as well as its amplitudes.

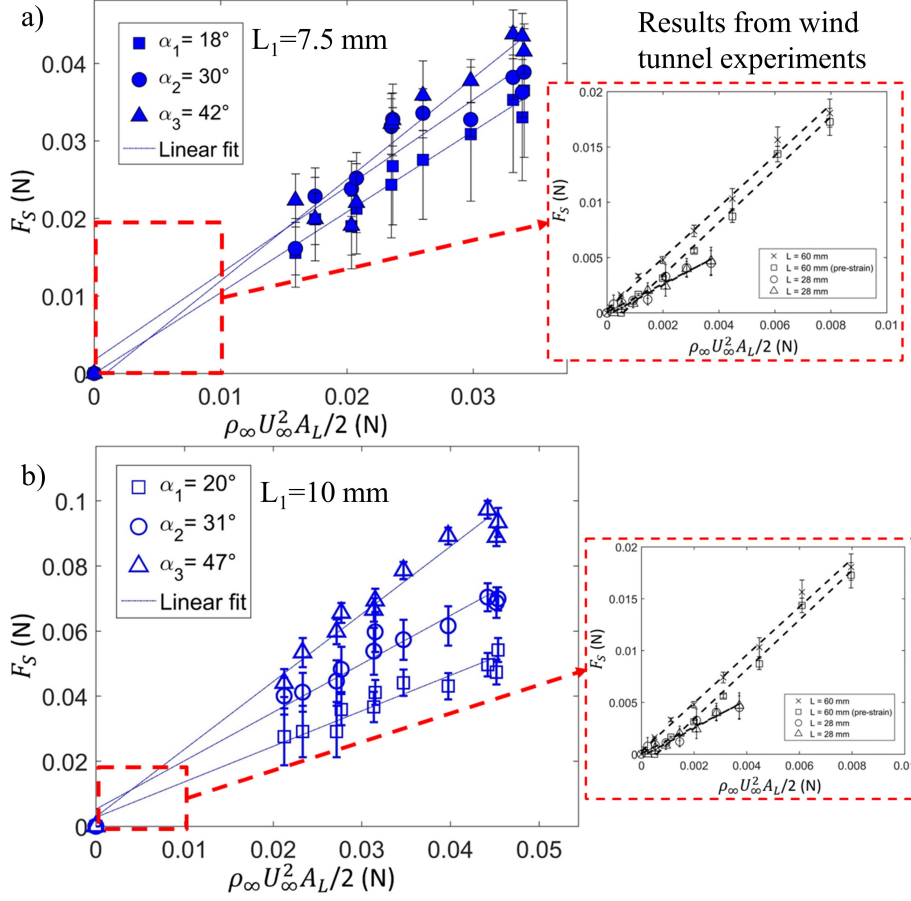


Figure 5.11: Steady tip displacement force of a flexible vibrating cantilever beam of both lengths ($L_1 = 7.5$ mm and $L_2 = 10$ mm) versus dynamic force with varying angle of attacks are compared with that of the results obtained from the wind tunnel experiments. The dotted lines are linear fits having slopes dependent on the angle of attack. This slope is identified as an aerodynamic loading coefficient C_{SAL} . Note that C_{SAL} increases with the increase in angle of attack .

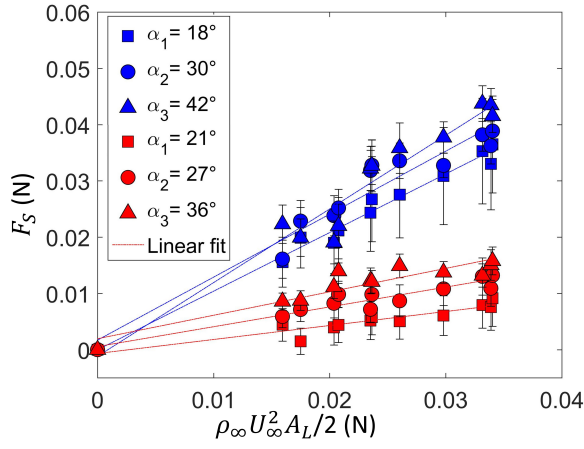


Figure 5.13 Steady tip displacement force of a relatively rigid vibrating cantilever beam of Length ($L_1 = 7.5 \text{ mm}$) versus dynamic force with varying angle of attacks.

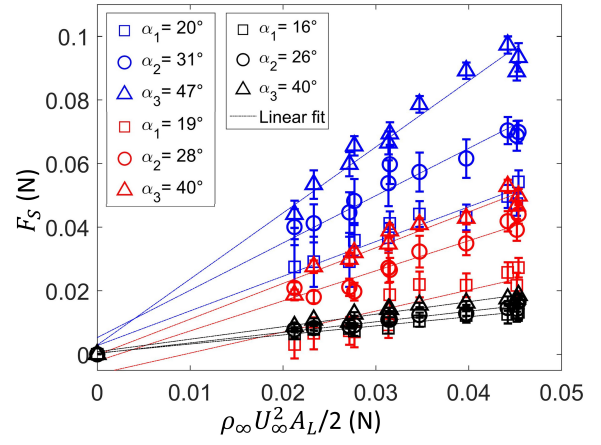


Figure 5.14 Steady tip displacement force of a relatively rigid vibrating cantilever beam of Length ($L_2 = 10 \text{ mm}$) versus dynamic force with varying angle of attacks.

Figure 5.15: The dotted lines are linear fits having slopes dependent on the angle of attack. These slopes are identified as an aerodynamic loading coefficient C_{SAL} . Note that C_{SAL} increases with the increase in angle of attack .

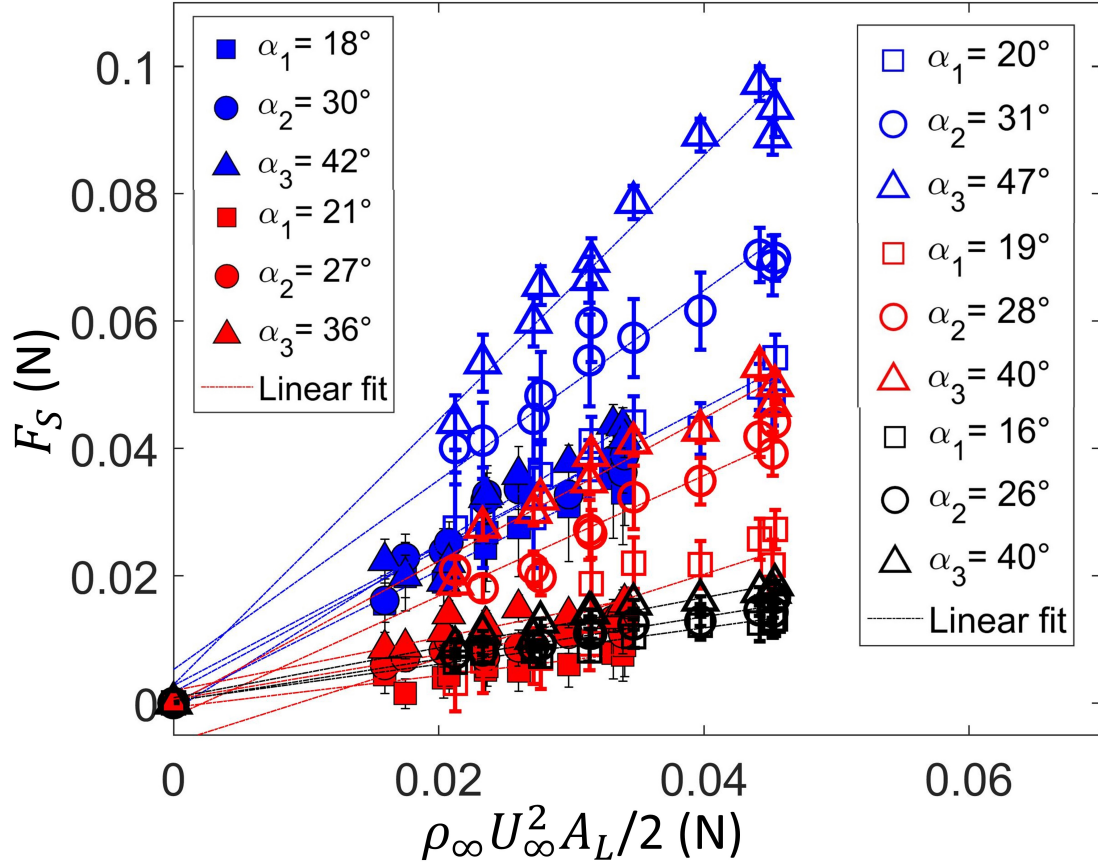


Figure 5.16: Steady tip displacement force of a relatively rigid vibrating cantilever beam of Lengths ($L_1 = 7.5 \text{ mm}$ and $L_2 = 10 \text{ mm}$) versus dynamic force with varying angle of attacks. The dotted lines are linear fits having slopes dependent on the angle of attack. This slope is identified as an aerodynamic loading coefficient C_{SAL} . Note that C_{SAL} increases with the increase in angle of attack .

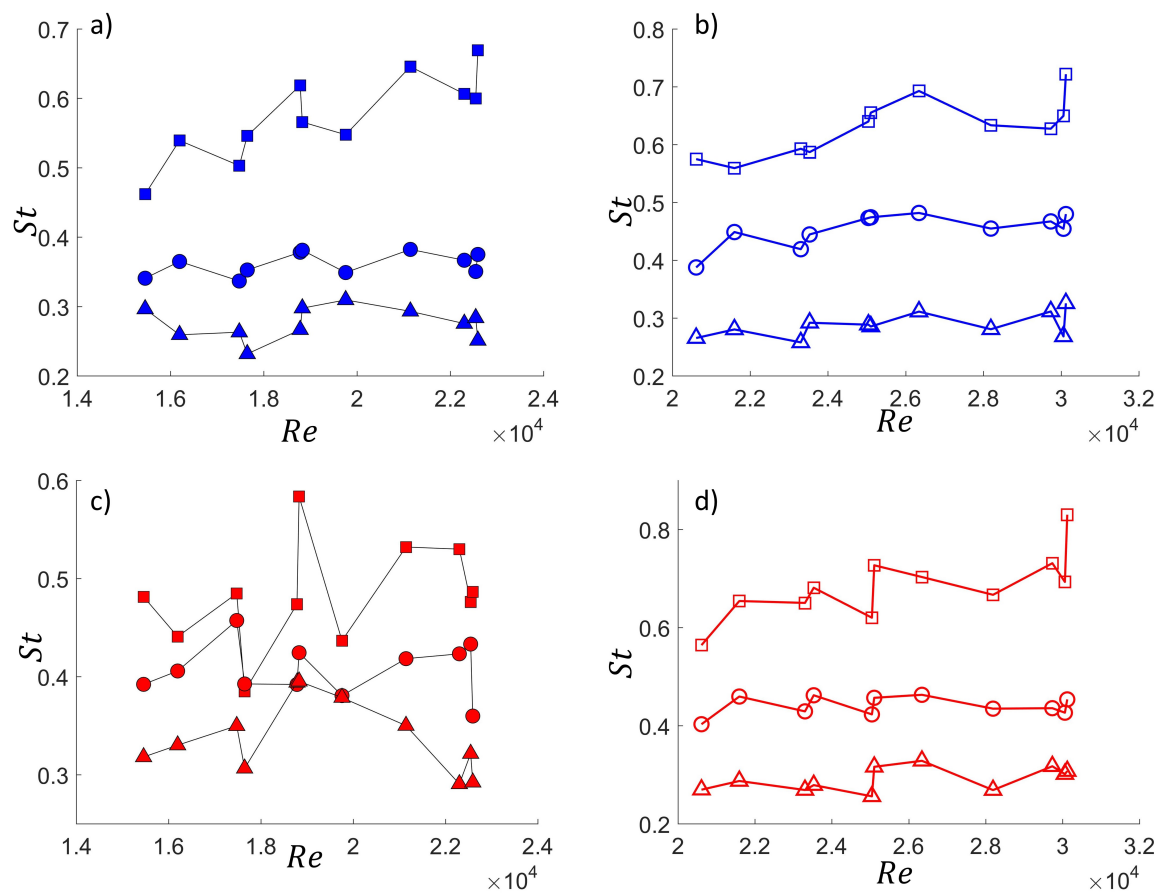


Figure 5.18 Strouhal numbers versus Reynolds numbers for Lengths ($L_1 = 7.5 \text{ mm}$) and ($L_2 = 10 \text{ mm}$)

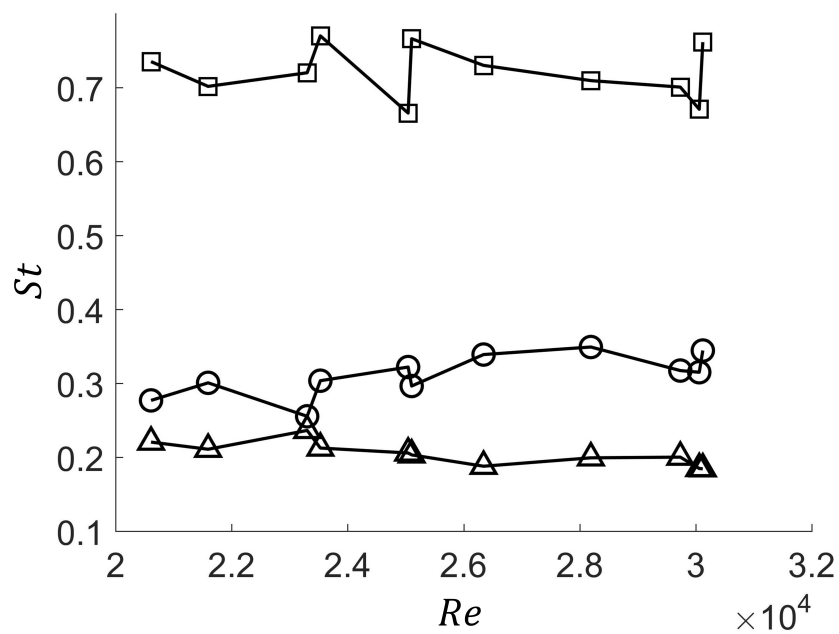


Figure 5.19 Strouhal numbers versus Reynolds numbers for rigid beam of Length ($L_2 = 10 \text{ mm}$)

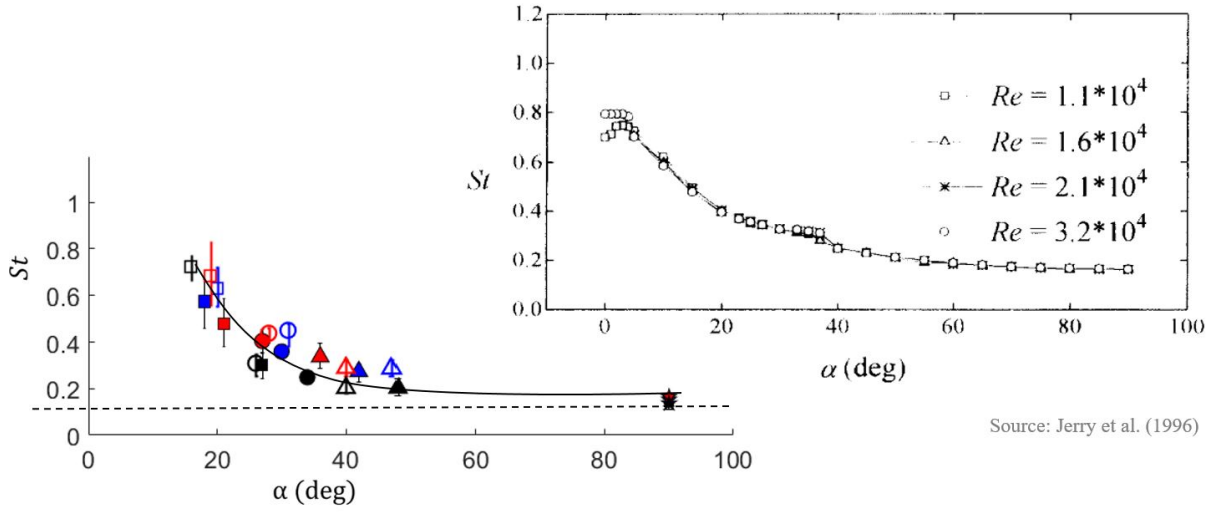


Figure 5.20: Strouhal number vs angle of attack for all data sets

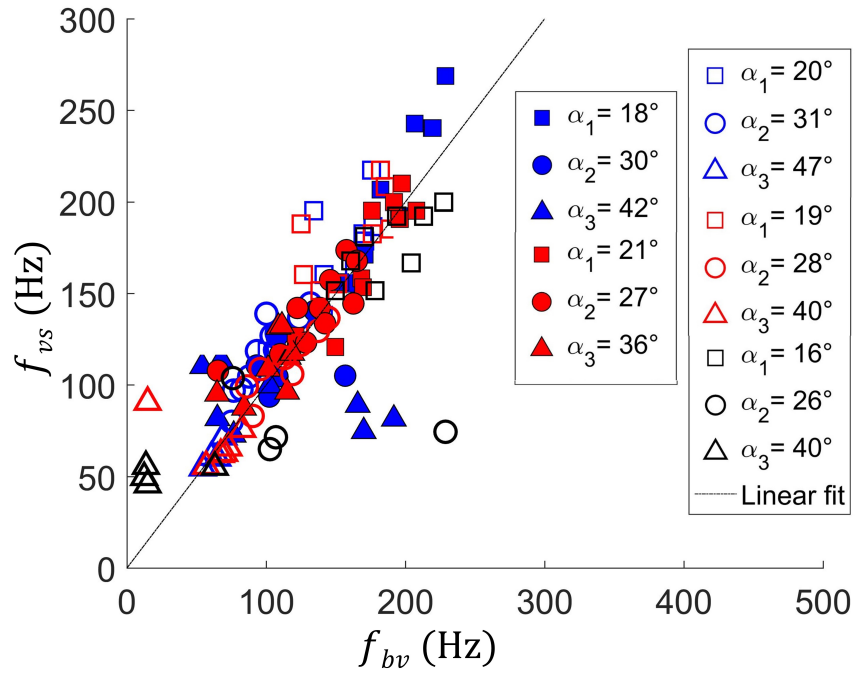


Figure 5.21: Vortex shedding frequency (f_{vs}) with corresponding beam vibrational frequencies (f_{bv}) for all data sets. Note how the data aligns with the $x=y$ line showing the dependency of f_{bv} with the corresponding f_{vs}

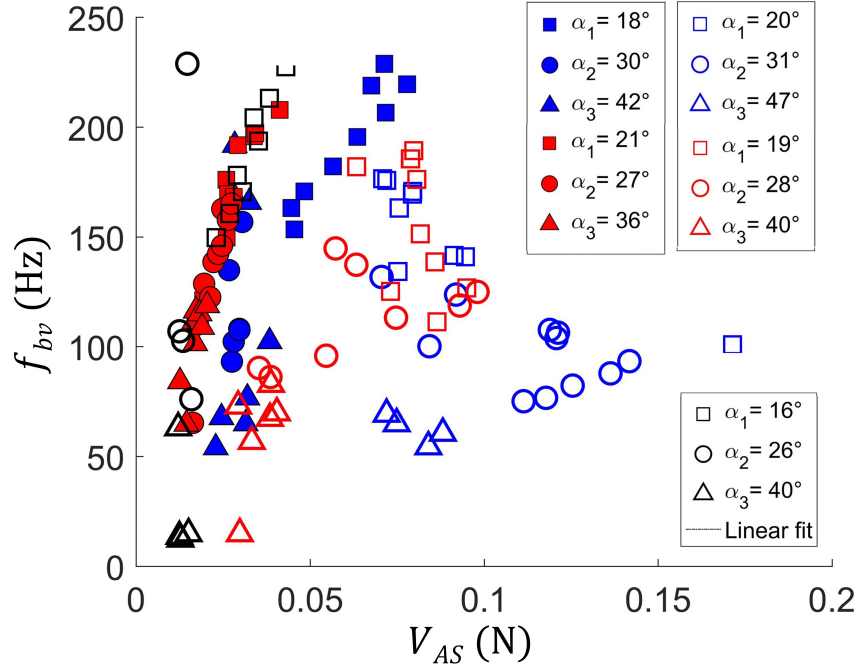


Figure 5.22: Beam vibrational frequencies (f_{bv}) with corresponding vibrational amplitude strengths (V_{as}) for all data sets. Same notation applies for the data. It can be observed that the flexible beam has a higher amplitude strengths i.e high amplitude of vibrations compared to the semi-flexible beam (red) and the rigid beam (black)

CHAPTER 6. CONCLUSIONS AND FUTURE WORK

We performed experiments for piezoelectric harvesting from flow in a low-speed wind tunnel and a dynamically similar system was utilized in a vertically falling soap film for flow visualization and data correlation. A novel soap film tunnel is introduced with a more redundant construction and reusable capability. A single cantilever beam of three rigidity modulus i.e from relatively flexible to a relatively rigid beam which are inclined with the flow direction at five increasing angle of attacks from 12° to 90° were studied in the soap film. The operating test section width of the soap film was 7.5 cm. A sophisticated set of techniques and algorithms that were written in MATLAB are presented for different sets of data. The experimental study, theoretical understanding are carried out to investigate the responses of these beams in a uniform flow. In addition, the design of vertically falling soap film tunnel, the measurements of flow field are discussed. Results of the steady aerodynamic loading vs dynamic loading suggests that at higher angles of attacks there is an increase in the coefficient of steady aerodynamic loading. When frequency of beam vibrations and the frequency of vortex shedding were plotted against each other, we find one-to-one linear relationship suggesting the beam vibrations are indeed the vortex induced vibrations. This statement is also supported by the literature and the beam exhibits lock-in behaviour with the vortex shedding in the wake.

The thesis major accomplishments,

1. We successfully built the vertical soap film tunnel in our laboratory and built a set of tools for its operation and processing. We improved the design of the experimental apparatus to work more effectively and efficiently.
2. We designed the data process schemes and developed corresponding programs. An image processing program was developed to extract beam vibrations from the high speed camera images. Considering the large amount of high speed camera images, another program was

developed to estimate the vibration frequency and amplitude as well as the vortex shedding behind the beams. These two parameters are used to establish a relation between the beams vibrations and the corresponding vortex shedding. It has been revealed that these variables are directly proportional to each other.

3. Thoroughly, studied the effects of angle of attack on the behavior of flexible beam interactions with its ambient fluid. We find the loading on the beams to increase drastically with the increase in angle of attack.

Using our soap film tunnel and processing tools, the next step would be to investigate the flow behavior in the case of multiple cantilever beams in various orientations, having an external bluff body to excite the oscillations to the flexible beam and many more as the applications can be limitless with these set of tools.

APPENDIX A. ADDITIONAL EXPERIMENTS

We have performed and analyzed some additional experiments for much higher angle of attacks in the range of $50^\circ < \alpha < 90^\circ$. The results we acquired in these experiments prove to be consistent with other experiments presented earlier in this thesis.

Higher inclination experiments

We have so far discussed about the effects of inclination on steady aerodynamic loading coefficient, flexible rigidity, lock-in phenomena of vortex shedding, Strouhal number etc for a limited set of angle of attacks. In this chapter we will be discussing a few higher angles of attack. We can now see a complete spectrum of angles that can easily be relatable to the work performed by Chen and Fang (1996). It seems like the Strouhal value converges to 0.16 as we go higher in angle of attack which is pretty comparable to the literature. More work and analysis is yet to be finished for the steady aerodynamic loading and the frequency of vibrations of these beams.

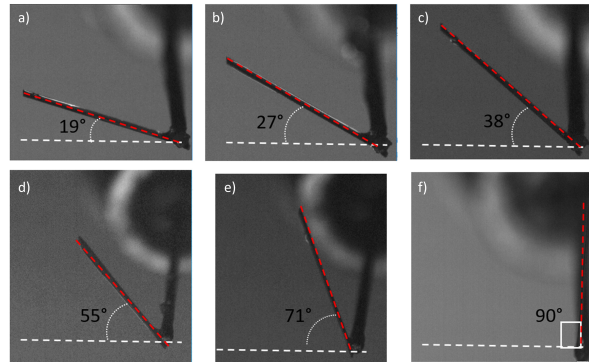


Figure A.1: Cantilever beam with the change in inclination. Analysis for St . Vs α can be found in Fig. [A.2](#)

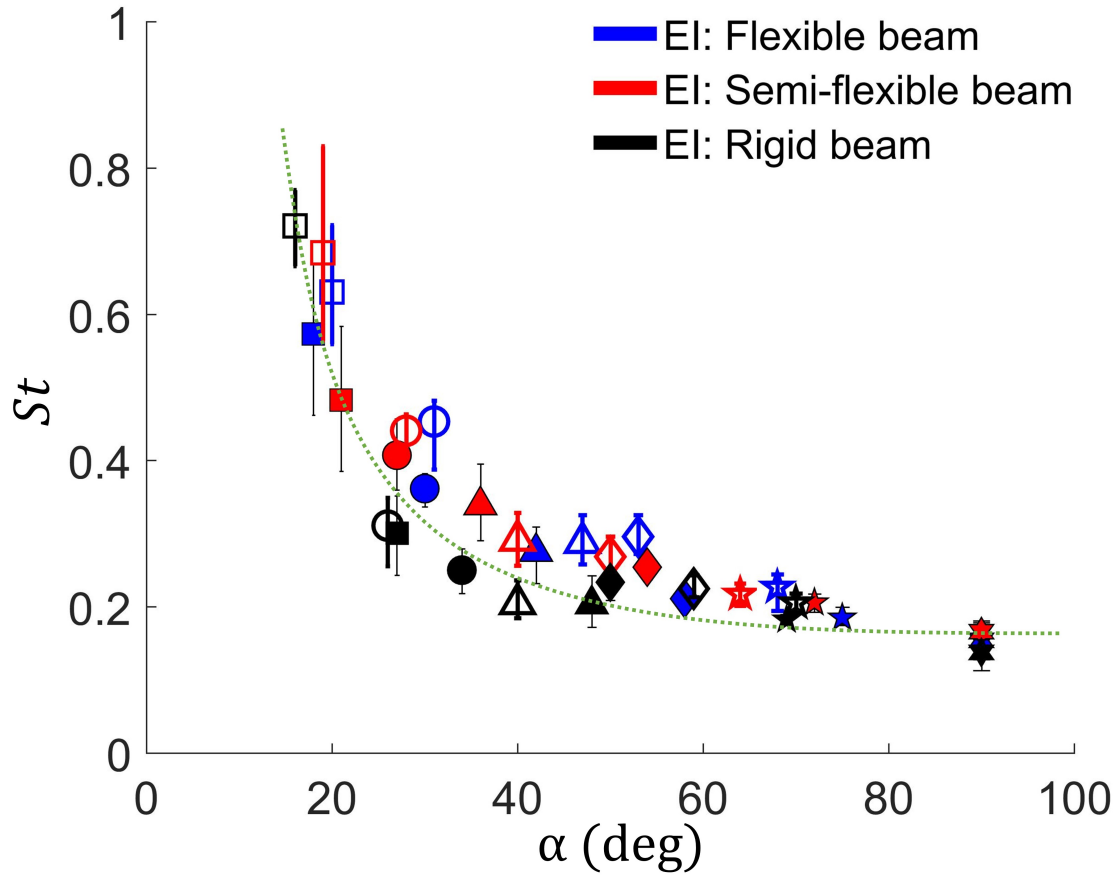


Figure A.2: Strouhal number Vs α updated with higher inclination experiments. A curve approximating the data is represented by the green dotted line.

APPENDIX B. SUPPLEMENTARY MATERIAL

Free small-amplitude vibration experiments were used to estimate the external (viscous) and internal (Kelvin-Voigt) damping coefficients. The experiments were conducted by displacing a piezoelectric cantilever (both short and long) from an equilibrium position, then releasing it while capturing the transient decay of the initial displacement using high speed video. Fig. S1 shows the resulting underdamped vibrations for the short Fig. S1(a) and long Fig. S1(b) cantilevers. Superimposed on the plot are the solutions to the Euler-Bernoulli equation assuming, internal damping only $\mu_1 = 0$, external damping only $\mu_2 = 0$, and a combination of the two $\mu_1 \neq 0$, $\mu_2 \neq 0$ according to the symbols listed in the legend.

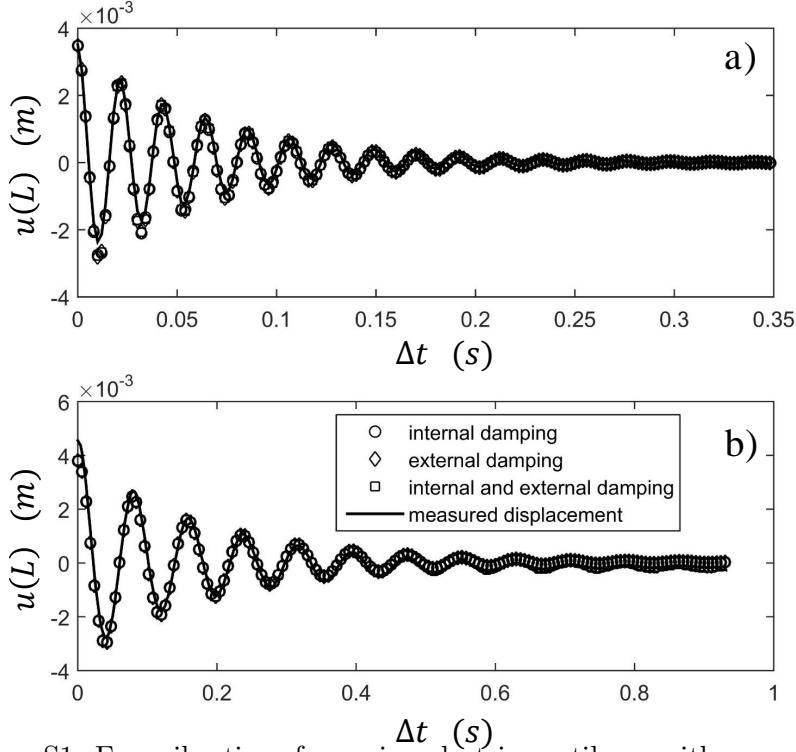


Figure S1: Free vibrations for a piezoelectric cantilever with aspect ratio a) 1.6 (short) and b) 3.6 (long).

Solutions to the Euler-Bernoulli equation were fit to the measured curve using a pattern search algorithm (details provided in Ref. White and Ward (2015)) based on a minimization of the ℓ^2 norm. We found solutions to the Euler-Bernoulli equation using numerical methods even though analytical solutions composed of a mixture of real and complex terms exist. The Euler-Bernoulli equation was advanced in time using a 4th order explicit Runge-Kutta-Merson method with adaptive time stepping. Validation of the numerical method was achieved by setting $\mu_1 = \mu_2 = F'_s = F'_\omega = 0$ and determining the natural frequency which agreed with the analytical solution.

Table B.1: Aerodynamic forcing coefficients $F_i = C_i \rho_\infty U_\infty^2 A_L / 2$ where $i = s$ or ω corresponding to steady and unsteady forcing, respectively.

Aspect Ratio	μ_1 (Pa s)	μ_2 (Pa s)
1.6	0.203	0
1.6	0	1.12×10^6
1.6	0.175	1.44×10^5
3.6	0.065	0
3.6	0	4.92×10^6
3.6	0.062	1.41×10^5

A summary of the estimates for μ_1 and μ_2 appears in Table. ???. The internal damping coefficients are nearly equivalent for $\mu_1 \neq 0$ and $\mu_2 \neq 0$. The external damping for the higher aspect ratio cantilever is about one-third of the lower one for the same condition.

In Fig. S2 we plot the resulting waveform solutions for the same free stream velocities shown in Fig. 1.8 from the main text. We used only the natural frequency to produce these plots. Adding additional frequencies, such as the ones appearing in the vicinity of the natural frequency in Fig. 1.9 of the main text, for example, would produce plots that are closer in appearance to those in Fig. 1.8 (Madanu et al., 2016).

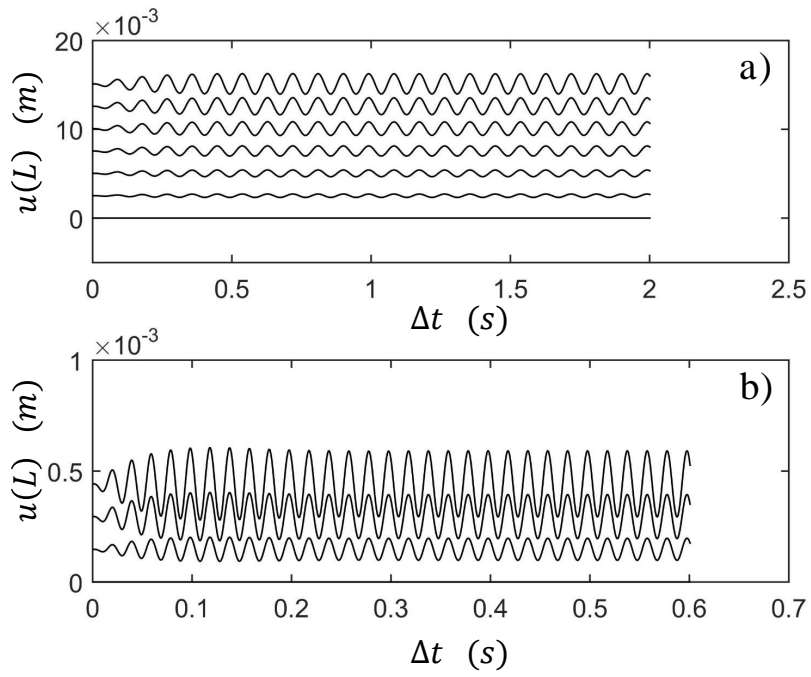


Figure S2: Displacement versus elapsed time waveforms for a) 3.6 and b) 1.6 aspect ratio piezoelectric cantilever beams found by solving the Euler-Bernoulli beam equation.

BIBLIOGRAPHY

- Adendorff, K., Naidoo, R., Jimoh, A., Okojie, D., et al. (2015). A hybrid piezoelectric micro-power generator for use in low power applications. *Renewable and Sustainable Energy Reviews*, 49:1136–1144.
- Akaydin, H., Elvin, N., and Andreopoulos, Y. (2012). The performance of a self-excited fluidic energy harvester. *Smart materials and Structures*, 21(2):025007.
- Allen, J. and Smits, A. (2001). Energy harvesting eel. *Journal of fluids and structures*, 15(3-4):629–640.
- Argentina, M. and Mahadevan, L. (2005). Fluid-flow-induced flutter of a flag. *Proceedings of the National academy of Sciences of the United States of America*, 102(6):1829–1834.
- Banks, H. T. and Inman, D. (1989). On damping mechanisms in beams.
- Chen, J. M. and Fang, Y.-C. (1996). Strouhal numbers of inclined flat plates. *Journal of wind engineering and industrial aerodynamics*, 61(2-3):99–112.
- Chomaz, J.-M. (2001). The dynamics of a viscous soap film with soluble surfactant. *Journal of Fluid Mechanics*, 442:387–409.
- Chomaz, J.-M. (2002). 2d or not 2d, the soap film dilemma. *Journal of Fluid Mechanics*.
- Cook-Chennault, K., Thambi, N., and Sastry, A. (2008). Powering mems portable devicesa review of non-regenerative and regenerative power supply systems with special emphasis on piezoelectric energy harvesting systems. *Smart Materials and Structures*, 17(4):043001.
- Couder, Y., Chomaz, J., and Rabaud, M. (1989). On the hydrodynamics of soap films. *Physica D: Nonlinear Phenomena*, 37(1-3):384–405.

- Dayou, J., Kim, J., Im, J., Zhai, L., How, A. T. C., and Liew, W. Y. (2015). The effects of width reduction on the damping of a cantilever beam and its application in increasing the harvesting power of piezoelectric energy harvester. *Smart Materials and Structures*, 24(4):045006.
- Erturk, A., Vieira, W., De Marqui Jr, C., and Inman, D. (2010). On the energy harvesting potential of piezoaeroelastic systems. *Applied Physics Letters*, 96(18):184103.
- Gharib, M. and Derango, P. (1989). A liquid film (soap film) tunnel to study two-dimensional laminar and turbulent shear flows. *Physica D: Nonlinear Phenomena*, 37(1-3):406–416.
- Greco, V. and Molesini, G. (1996). Monitoring the thickness of soap films by polarization homodyne interferometry. *Measurement Science and Technology*, 7(1):96.
- Han, S. M., Benaroya, H., and Wei, T. (1999). Dynamics of transversely vibrating beams using four engineering theories. *Journal of Sound and vibration*, 225(5):935–988.
- Hidema, R., Yatabe, Z., Shoji, M., Hashimoto, C., Pansu, R., Sagarzazu, G., and Ushiki, H. (2010). Image analysis of thickness in flowing soap films. i: effects of polymer. *Experiments in fluids*, 49(3):725–732.
- Hirata, M. H., Pereira, L. A. A., Recicar, J. N., and Moura, W. H. d. (2008). High reynolds number oscillations of a circular cylinder. *Journal of the Brazilian Society of Mechanical Sciences and Engineering*, 30(4):304–312.
- Hobeck, J. and Inman, D. (2012). Artificial piezoelectric grass for energy harvesting from turbulence-induced vibration. *Smart Materials and Structures*, 21(10):105024.
- Jia, L. (2014). *The Interaction Between Flexible Plates and Fluid in Two-dimensional Flow*. Springer.
- Jia, L., Xiao, Q., Wu, H., Wu, Y., and Yin, X. (2015). Response of a flexible filament in a flowing soap film subject to a forced vibration. *Physics of Fluids*, 27(1):017101.
- Jia, L.-B. and Yin, X.-Z. (2009). Response modes of a flexible filament in the wake of a cylinder in a flowing soap film. *Physics of Fluids*, 21(10):101704.

- Kellay, H., Wu, X., and Goldburg, W. (1995). Experiments with turbulent soap films. *Physical review letters*, 74(20):3975.
- Kim, M., Dugundji, J., and Wardle, B. L. (2015). Efficiency of piezoelectric mechanical vibration energy harvesting. *Smart Materials and Structures*, 24(5):055006.
- Koyama, D. and Nakamura, K. (2010). Electric power generation using vibration of a polyurea piezoelectric thin film. *Applied Acoustics*, 71(5):439–445.
- Lam, K. and Leung, M. (2005). Asymmetric vortex shedding flow past an inclined flat plate at high incidence. *European Journal of Mechanics-B/Fluids*, 24(1):33–48.
- Madanu, S. B., Barbel, S. I., and Ward, T. (2016). Electrostatic and aerodynamic forced vibrations of a thin flexible electrode: Quasi-periodic vs. chaotic oscillations. *Chaos: An Interdisciplinary Journal of Nonlinear Science*, 26(6):063113.
- Mateu, L. and Moll, F. (2005). Optimum piezoelectric bending beam structures for energy harvesting using shoe inserts. *Journal of Intelligent Material Systems and Structures*, 16(10):835–845.
- Pobering, S., Menacher, M., Ebermaier, S., and Schwesinger, N. (2009). Piezoelectric power conversion with self-induced oscillation. *PowerMEMS*, 2009:384–387.
- Priya, S., Chen, C.-T., Fye, D., and Zahnd, J. (2004). Piezoelectric windmill: a novel solution to remote sensing. *Japanese journal of applied physics*, 44(1L):L104.
- Rutgers, M., Wu, X., and Daniel, W. (2001). Conducting fluid dynamics experiments with vertically falling soap films. *Review of Scientific Instruments*, 72(7):3025–3037.
- Schmidt, V. H. (1992). Piezoelectric energy conversion in windmills. In *Ultrasonics Symposium, 1992. Proceedings., IEEE 1992*, pages 897–904. IEEE.
- Song, R., Shan, X., Lv, F., and Xie, T. (2015). A study of vortex-induced energy harvesting from water using pzt piezoelectric cantilever with cylindrical extension. *Ceramics International*, 41:S768–S773.

- Vorobieff, P., Rivera, M., and Ecke, R. (1999). Soap film flows: Statistics of two-dimensional turbulence. *Physics of Fluids*, 11(8):2167–2177.
- White, A. R. and Ward, T. (2015). Pattern search methods for pendant drops: Algorithms for rapid determination of surface tension and surfactant transport parameters. *Colloids and Surfaces A: Physicochemical and Engineering Aspects*, 485:1–10.
- Zakaria, M. Y., Al-Haik, M. Y., and Hajj, M. R. (2015). Experimental analysis of energy harvesting from self-induced flutter of a composite beam. *Applied Physics Letters*, 107(2):023901.
- Zhang, J., Childress, S., Libchaber, A., and Shelley, M. (2000). Flexible filaments in a flowing soap film as a model for one-dimensional flags in a two-dimensional wind. *Nature*, 408(6814):835–839.
- Zhao, L. and Yang, Y. (2015). Enhanced aeroelastic energy harvesting with a beam stiffener. *Smart Materials and Structures*, 24(3):032001.